UNIVERSITY OF CALIFORNIA
SANTA CRUZ

SYNTHESIS, CHARACTERIZATION, AND PHOTOPHYSICAL PROPERTIES OF PFNGX CHEMICAL SERIES IN CONJUGATED POLYELECTROLYTE COMPLEXES

A dissertation submitted in partial satisfaction
of the requirement for the degree of

DOCTOR OF PHILOSOPHY

in

CHEMISTRY

By

Gregory M. Pitch

December 2021

The Dissertation of Gregory M. Pitch
is approved:

Professor Alexander Ayzner, Chair

Professor Rebecca Braslau

Professor Jin Zhang

Peter Biehl
Vice Provost and Dean of Graduate Studies

Contents

Figures

Abstract

SYNTHESIS, CHARACTERIZATION, AND PHOTOPHYSICAL PROPERTIES OF PFNGX CHEMICAL SERIES IN CONJUGATED POLYELECTROLYTE COMPLEXES

Gregory M. Pitch

Conjugated polyelectrolytes (*CPEs*) absorb light, are soluble in aqueous media, and are amenable to forming higher-order architectures via non-covalent interactions. CPEs provide rapid coherent intra-chain exciton transfer due to delocalization of excited states and have pendant ionic sidechains that make them soluble in aqueous media and enable complexation with oppositely charged CPEs to form conjugated polyelectrolyte complexes (*CPECs*). CPECs as building blocks for multi-component light-harvesting systems approach panchromaticity and participate in rapid intra-chain and inter-chain electronic energy transfer (*EET*) for directionally guiding excited states towards a reaction center.

To increase the density of and proximity between CPE chains in solution, high ionic strength conditions induce liquid-liquid phase separation, which form CPE rich and CPE poor phases. The CPE rich phase containing exciton donor-acceptor pairs will form the basis of a multicomponent light-harvesting fluid, which offers the ability to host components that would perform specific tasks such as chemical reactions or charge separation. Fluidity is necessary for diffusion of reactants in and out of the light-

harvesting scaffold. To this end, progress has been made forming complex light-harvesting fluids with fully conjugated CPECs, albeit the phase of the system tends toward being more rigid than fluid.

To combat the rigidity of the desired complex light-harvesting fluid, a brush-like polyfluorene-based exciton-donor CPE series was designed and synthesized to increase the polar-character of the CPEC. This copolymeric series has one monomer that contains pendant ionic sidechains and another monomer that is functionalized with oligoethylene glycol (*oEG*) sidechains with 3, 6, 9 , or 12 ethylene glycol (*EG*) units. The brush-like PFNGX series is highly water-soluble and remarkably stable at high ionic strength. To answer whether beyond a certain length of oEG sidechain, complexation and EET will be hindered, CPECs were formed using the synthesized exciton-donor PFNGX (3, 6, 9) series and a polythiophene-based exciton acceptor, and then interrogated with a combination of photoluminescence (*PL*) quenching experiments and photoluminescence excitation experiments. Complexation and EET between exciton donor-acceptor CPE pairs was found to be independent of oEG chain length, and led to a postulated CPEC structure which rationalize these findings.

Acknowledgments

There have been many groups of people who deserve a special thank you for helping with the completion of my dissertation, such as beamline scientists, collaborators, members of the UC Santa Cruz community, and my family.

The beamline scientists and collaborators include: Tim J. Dunn, Cheng Wang, Prof. Jianguo Mei, Prof. Darren Lipomi, Dr. Aristide Gumyusenge, and Kartik Choudhary.

I'd like to thank members of the UC Santa Cruz community such as: Prof. Alex Ayzner, Prof. John Macmillan, Prof. Jin Zhang, Prof. Rebecca Braslau, Dr. Hsiau-Wei Lee, Dr. Bakthan Singaram, Dr. Shaun McKinnie, Dr. Rahul Shingare, Victor Aniebok, Duy Vo, David Delgadillo, Daniel Droege, Patrick Skelly, Wiley Schultz-Simonton, Dr. Longbo Li, Avery Baerlin, Chayo Fuentes, Kevin Schilling, Francesca Pavlovici, Dr. William Right Hollingsworth IV, Dr. Michael Roders, Dr. Carmen Segura, Pamela Schleissner, Ariel Kuhn, Anna Johnston, Levi Matsushima, Yannick Kraemer, Jack Palmer, Reilly Seban, Brett Crockett, Rachael Richards, and Ivette Mora.

I want to thank members of my family for their support, specifically Donna and Lou, Vanessa, Sean, Seanie, Cameron, Reilly, Nick, Sabrina, Mason, Irene, Casey, Mike and Mere.

To the love of my life, Stephanie, you are the reason I keep pushing on, I dream because of you. Thank you for everything, I am forever grateful.

To my beautiful best friends, Mocha and Earl, you bring me so much joy.

For

Stephanie Grace

Chapter 1

INTRODUCTION

1.1 Introduction

1.1.1 Overview

The current state of environmental affairs, which involves burning fossil fuels to facilitate day to day societal activities, places future generations in an existential crisis. Gaseous carbon dioxide (CO_2) is the product of fossil fuel combustion and the increase in the concentration of CO_2 in the atmosphere has caused the temperature of the earth to rise.[1] The increase in Earth's average temperature has indirect effects such as sea-level rise, increased drought, and stronger storm systems, all of which ultimately affect society's well-being. Production of energy through alternative methods such as via geothermal, wind, and solar technologies all aim to reduce humanities dependency on the combustion of fossil fuels.[1]

Out of all of the alternative energy technologies, solar has the advantage of not only being renewable but also abundant and predictable.[2] Solar technologies have traditionally been constructed with inorganic materials such as silicon due to its cost and efficiency.[3,4] However, the most abundant solar to energy conversion in nature occurs consistently via photosynthesis in plants.[5,6] Many years of evolution have developed light harvesting systems that are robust and highly efficient due to an intricate arrangement and proximity of organic components. Photosynthetic light-harvesting antennae scavenge incoming light by absorbing photons of various wavelengths and generate excited states that are funneled to reaction centers.[5,6] Here,

the electronic excited states are converted into separated charges, participate in sequential electron transfers, and eventually becomes stored as electro-chemical potential. Therefore, it would be less than ideal to overlook photosynthetic organisms as inspiration for synthetic light harvesting applications. It is to this end that the concept of utilizing light harvesting antennae arranged into higher order architectures via non-covalent interactions is exploited.

For this purpose, a promising class of semiconducting polymers are conjugated polyelectrolytes (*CPEs*) since they absorb light, are soluble in aqueous media, and are amenable to forming higher-order architectures via non-covalent interactions. CPEs have conjugated backbones that provide rapid coherent intra-chain exciton transfer due to delocalization of excited states.[7–13] Additionally, CPEs have pendant ionic side chains that make them aqueous soluble and able to complex with oppositely charged CPEs. A cationic poly(fluorene-alt- phenylene) CPE is shown in **Figure 1.1**.

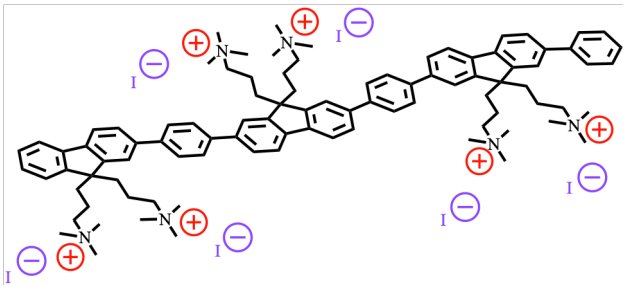

Figure 1.1 Chemical structure of cationic poly(fluorene-alt-phenylene) CPE with coulombically bound iodide anions.

Oppositely charged CPE complexes (*CPECs*) have additional properties that are important for use in a multi-component light-harvesting system, such as the possibility for the light-harvesting system to be panchromatic and the ability to perform rapid inter-chain electronic energy transfer (*EET*).[7–12] The desire to create a panchromatic light-harvesting system arises from needing to harvest incident light at all visible wavelengths in order to maximize the system's light-harvesting efficiency. Intra-chain and inter-chain EET provide methods for directionally guiding excited states towards a reaction center.[8,9] A CPEC formed from a cationic poly(fluorene-alt- phenylene) CPE coulombically bound to an anionic poly(thiophene) CPE is shown in **Figure 1.2**.

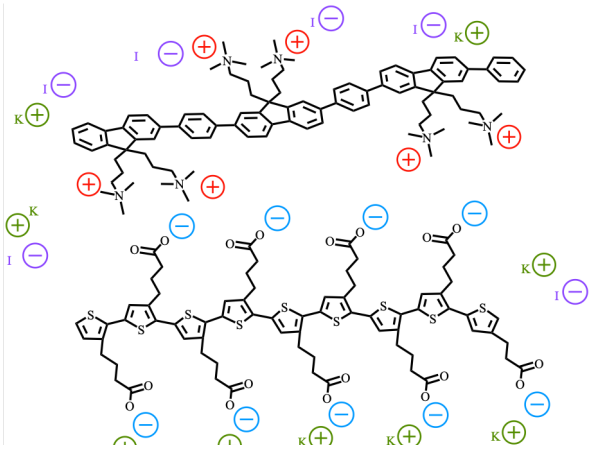

Figure 1.2 CPEC formed from a cationic poly(fluorene-alt- phenylene) CPE coulombically bound to an anionic poly(thiophene) CPE. Cartoon is shown with respective counterions.

The Ayzner lab aims to create a complex light-harvesting fluid from exciton donor-acceptor CPECs in the limit of high ionic strength. The goal is to create a light-harvesting fluid via associative phase separation that will form the foundation of a light-

harvesting scaffold. This desired fluid phase would be concentrated in CPE and would offer the ability to host components that would perform specific tasks, such as chemical reactions or charge separation. Along with retaining its modular capabilities, fluidity is necessary for diffusion of reactants in and out of the light-harvesting scaffold. Progress has been made in forming complex light-harvesting fluids with fully conjugated CPECs, however the phase of the system tends towards being more rigid than fluid. Along with the CPE having limited solubility due to electrostatic screening of its pendant ionic side chains when complexed with oppositely charged CPECs at ionic stoichiometry, the state of the phase has been attributed to the CPE partaking in many hydrophobic and π-stacking interactions. Our central hypothesis is that fluidity and stability must come from polar-but-nonionic side chains that do not participate in ionic inter-CPE complexation.

To combat the rigidity of the desired complex light-harvesting fluid, a new series of exciton-donor CPEs was designed and synthesized to increase the polar character of the CPEC. This series is a polyfluorene-based alternating copolymer where one monomer contains pendant ionic side chains and the other monomer is functionalized with oligoethylene glycol (*oEG*) side chains with 3, 6, 9, or 12 ethylene glycol (*EG*) units. The brush-like PFNGX series, where X is the number of EG units in the oEG chain appended to the polymer backbone, is highly water-soluble and remarkably stable at high ionic strength. Polymer repeat units for the PFNGX (3, 6, 9, 12) series are shown in **Figure 1.3**.

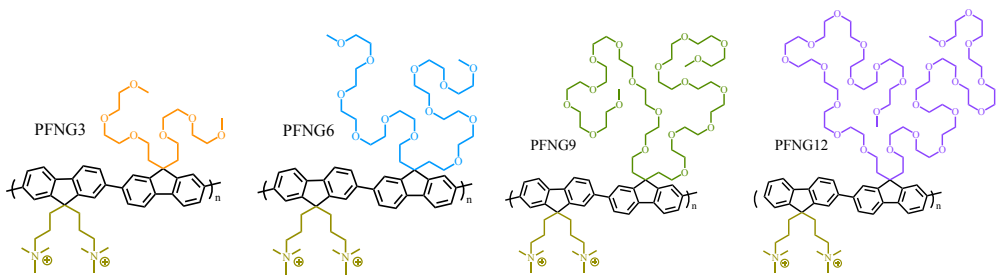

Figure 1.3 Polymer repeat units for PFNGX series (X = 3, 6, 9, 12).

Photophysical and structural characterization of isolated chains of PFNGX (3, 6, 9) series in aqueous solution were carried out to interrogate the optical properties and chain microstructures of each of the polymers. This was followed up with formation of oppositely charged artificial light-harvesting antennae, using the synthesized exciton-donor PFNGX (3, 6, 9) series and a polythiophene-based exciton acceptor that is common to all exciton donors. This was done to answer a secondary and more readily attainable hypothesis: beyond what length of oEG side chains will complexation and EET will be hindered? The next sections will help elucidate the important properties of CPEs and their role as important building blocks in modular light-harvesting systems.

1.1.2 Conjugated Polyelectrolytes as Light-harvesting Antennae

Along with being classified as semi-conducting, organic materials are inexpensive and non-crystalline, which make them widely applicable for large-scale synthesis, solution processability, and deposition onto flexible substrates.[14] CPEs are commonly

used as materials for light-harvesting applications due to their processability and charge transfer properties.[15] Due to being polymeric and having a conjugated backbone via alternating double bonds, their electronic states are delocalized. Conjugation essentially arises from constructive overlap of p orbitals on adjacent monomers.

When atomic orbitals constructively and destructively interact to form molecular orbitals, the valence electrons from each contributing atomic orbital populate the molecular orbitals up until the number of electrons are exhausted. This leads to an orbital becoming the highest occupied molecular orbital (*HOMO*). The next highest energy level which is unoccupied is referred to as the lowest unoccupied molecular orbital (*LUMO*).[16] This has huge implications for the electronic properties of organic molecules which effectively deems them as semi-conductive materials since an input of energy is needed to induce electronic transitions from the HOMO to the LUMO and higher-lying unoccupied energy levels. The probability of a photoexcitation to occur between and initial and final state λ_{if} is to a good approximation described by Fermi's Golden Rule, shown with Equation 1.1,[17]

$$\lambda_{if} = \left(2\pi/\hbar\right)|M_{if}|^2\rho_f \tag{1.1}$$

where ρ_f represents the density of final states and $\hbar$ represents the reduced Planck's constant. M_{if} is the transition dipole moment which describes the interaction of the dipole moment operator with the initial and final wavefunctions in the presence of a constant electric field.[17]

Another notable property of organic materials is that the binding energy of a photoexcited electron to its hole in the HOMO band is quite large, meaning that the dissociation of the electron from the bound hole is not a spontaneous process. For polyfluorene with alkyl side chains, the exciton binding energy has been reported as 0.2-0.3 eV.[18–20] This prevents thermal energy from dissociating the excited electron from the formed hole.[17] This net-neutral coulombically bound electron-hole pair is referred to as an exciton.[17] Two types of excitons exist: a Frenkel exciton and a Wannier-Mott exciton. The Frenkel exciton is localized to a few monomers, has a binding energy between 0.1- 1.0 eV, and is the common type of coulombically bound net-neutral excited state found in organic semiconductors. The Wannier-Mott exciton, characterized by having a smaller binding energy of ~ 0.01 eV, is a consequence of electrostatic screening of the bound charges from existing in a high dielectric material. This results in the Wannier-Mott exciton spanning multiple unit cells.[17]

Excitons generated on a polymer may undergo intra-chain EET if the nearby chromophores (intra-chain) are lower in energy than the segment of polymer chain from which the Frenkel exciton was originally generated.[11] A principal aspect of creating a light-harvesting system is for photogenerated excitons to quickly migrate to lower energy segments of polymer chain, so that energy can be focused at a reaction center.[6] Migration has to occur quickly as to increase the probability that excitons reach a reaction center before geminate recombination occurs. The microstructure of the polymer chain influences the energetic landscape of the chromophores that surround a photogenerated exciton and ultimately dictates the migration pathways available.[11]

Since the side chains are not conjugated to the aromatic backbone of the polymer, aliphatic side chains do not electronically couple to the CPE. However, depending on the identity of the side-

chain and the specific conjugated backbone, a CPE will adopt a certain solution state microstructure. This is very important because the overall microstructure of the polymer chain has direct implications for the electronic properties of the polymer, which ultimately affects the light-harvesting efficiency when incorporated into a device.[9,21] Various CPEs can have chain microstructures that vary widely because of their inherent persistence lengths: quantities that describe the flexibility of a polymer. Polymer chains that are shorter than the persistence length can effectively be characterized as a rigid rod.[22] Polymer chains that are longer than the CPEs persistence length can adopt various conformations, such as a randomly coiled microstructure.[9]

Organic materials interact with surrounding matter via non-covalent van der Waals interactions. To understand the origin of their microstructure and in turn their electronic properties, it is therefore important to think about the types of interactions in which chemical moieties participate. Polymer backbones that are comprised of fused aromatic ring systems have very long persistence lengths which not only impact the chain microstructure but also affect the propensity of polymer chains to participate in solution state aggregation.[7,21] Aggregation occurs as a result of π- π interactions between aromatic moieties. In contrast, other CPEs have conjugated backbones that allow for high degrees of rotation, which limit aggregation.[9,10]

Besides π - π interactions, other notable non-covalent interactions that affect the microstructure of a polymer chain are hydrophobic, dipole-dipole, dipole induced-dipole, London-dispersion, and cation- π.[23] Each of these arises from interactions between specific chemical moieties or chemical species. Aliphatic side chains interact in a plethora of ways depending on their chemical environment. Specifically, non-polar moieties interact with other non-polar groups in a repulsive manner at close distances via a nucleus- nucleus coulombic repulsion, and attractively at distances commensurate with the sum of the van der Waals radii.[23] Side chains with pendant ionic groups interact with partially or fully charged moieties such as conjugated systems or other pendant ionic side chains. These interactions are attractive or repulsive depending on the sign and magnitude of the charge, as well as the distance between charges.[23]

1.1.3 Conjugated Polyelectrolyte Complexes

Oppositely charged CPEs interact attractively to form CPECs largely via electrostatic interactions between ionic side chains. These complexes, consisting of exciton-donor and exciton-acceptor CPEs, are the building blocks utilized in our artificial light-harvesting systems because they form polymeric assemblies that can directionally guide excited state energy via intra and inter-chain EET. Light-harvesting systems with CPECs have a high percentage of photo-active components, due to light absorption properties of each CPE. Additionally, light-harvesting becomes more efficient when each CPE absorbs visible light at complementary energies. Panchromaticity of light-active components in a CPEC may also lead to an overlap of

the fluorescence spectrum of the exciton-donor and the absorption profile of the exciton-acceptor, which is one of the driving factors of EET.

The critical mechanism for inter-chain EET in CPECs is via Förster Resonant Energy Transfer (*FRET*), which is a non-radiative energy transfer process that can occur if the fluorescence spectrum of the exciton-donor and the absorption spectrum of the exciton-acceptor have significant overlap.[8] However, the distance between a chromophore's wavefunctions and the spatial orientation between transition dipole moments also dictates if and with what quantum efficiency the exciton donor transfers electronic energy to the exciton-acceptor.[24] Efficient FRET requires that the exciton donor and the exciton acceptor are separated by distances on the order of 10 nm. The FRET rate constant is given as Equation 1.2,

$$k_{ET} = k_D \left[\frac{R_0}{R}\right]^6 = \frac{1}{\tau_D^0}\left[\frac{R_0}{R}\right]^6 \quad (1.2)$$

where τ_D^0 is the fluorescence excited state lifetime of the donor in the absence of the acceptor. The exciton donor's decay rate in the absence of energy transfer is equal to $k_D = \frac{1}{\tau_D^0}$, R represents the distance between donor and acceptor, and R_0 is the Förster radius. The Förster radius is the distance from the exciton donor at which the spontaneous decay from the donor excited state and energy transfer to the exciton acceptor have equal probability.[24] The transfer efficiency Φ_{ET} is mathematically defined in equation 1.3.[24]

$$\Phi_{ET} = \frac{k_{ET}}{(k_D + k_{ET})} = \frac{1}{1+(R/R_0)^6} \quad (1.3)$$

The Förster radius, also known as the critical transfer distance, is given by Equation 1.4.[24]

$$R_0^6 = \left(\frac{9(\ln 10)}{128\pi^5 N_A}\right)\left(\frac{\kappa^2 \Phi_D}{n^4}\right) J \quad (1.4)$$

N_A is Avogadro's number, and n is the average refractive index of the medium. The orientation factor, κ, physically represents the orientation of transition dipole moments of the exciton donor and exciton accepting chromophores. Equation 1.5 mathematically defines the orientation factor. In this equation $\vec{\mu}_D$ and $\vec{\mu}_A$ are the magnitudes of the transition dipole moment vectors of the donor and the acceptor respectively.[24] Moreover, $\vec{r}$ is the mutual displacement vector pointing from donor to acceptor.[24]

$$\kappa = \frac{\vec{\mu}_D \cdot \vec{\mu}_A - 3(\vec{\mu}_D \cdot \vec{r})(\vec{\mu}_A \cdot \vec{r})}{\mu_D \mu_A} \quad (1.5)$$

J is the spectral overlap integral which is represented in terms of wavelength, and is determined with Equation 1.6,[24]

$$J^\lambda = \int \bar{I}_\lambda^{D^*} \varepsilon_A(\lambda) \lambda^4 d\lambda \quad (1.6)$$

where $\bar{I}_\lambda^{D^*}$ is the fluorescence intensity of the excited donor normalized to unit spectral area and $\varepsilon_A(\lambda)$ is the molar absorption coefficient in terms of wavelength.[24]

FRET has been mathematically defined for donor-acceptor molecules that are small in comparison to the large distance that separates them. However, CPECs are formed from polymer chains that are separated by distances that are commensurate with or smaller than the size of each chromophore. Therefore, inter-chain EET in CPECs is not perfectly described by Förster's equations.[24]

Creating multi-component light-harvesting fluids in the limit of high ionic-strength via associative phase separation concentrates CPE chains into a CPE-rich phase. This brings CPE chains close in proximity to each other exacerbates the difficulties in describing inter-chain EET with FRET. Nevertheless, associative phase separation of CPECs is desirable to form multi-component light harvesting fluids that could function as photophysically active compartments in a larger overarching system or as fluid exciton guiding scaffolds for artificial electron transport chains and molecular catalysis.

Associative phase separation of exciton donor-acceptor CPEs to form a fluid light-harvesting system has yet to be realized. We hypothesize that this is because associative phase separation is most often formed between CPEs at ionic stoichiometric equivalence. Complexation between oppositely charged CPEs yields a CPEC with an overall net-charge. This occurs until a molar ratio between CPEs that correspond to equivalent amount of positive and negative charges. Below ionic equivalency, interactions between a CPE's pendant ionic side chains and nearby polar solvent molecules help solubilize the mostly non-polar conjugated polymer.[25] However, upon

electrostatically induced complexation between components at ionic stoichiometry, the absence of an overall net charge of the CPEC reduces its solubility in polar solvents.[8] Reduced solubility of CPECs is exacerbated at high ionic strengths due to electrostatic screening of charges on the pendant ionic side chains, which ultimately makes CPEs behave more like their neutral derivatives. Associative phase separation of a CPEC has led to rigid phases that lack the necessary fluidity to be used as exciton guiding scaffolds for artificial electron transport chains and molecular catalysis.

To increase the aqueous solubility of the net-neutral CPECs and fluidity of a multi-component light harvesting system, a series of exciton-donor CPEs was designed and synthesized. This series is a polyfluorene-based alternating copolymer where one monomer contains pendant ionic side chains and the other monomer is functionalized with oEG side chains with 3, 6, 9 , or 12 EG units. oEG side chains offer additional hydrogen-bonding interactions with water molecules that stabilize the overall net-neutral CPEC in high ionic strength media. Photophysical and structural characterization of isolated chains of PFNGX (3, 6, 9) series in aqueous solution were carried out to interrogate the optical properties and chain microstructures of each polymer. Then an artificial light-harvesting system was formed with oppositely charged CPEs, using the synthesized exciton-donor PFNGX (3, 6, 9) series and a polythiophene-based exciton acceptor that was common to all exciton donors. This was done to interrogate whether beyond a certain length of oEG sidechain, complexation and EET would be hindered. The next section will detail how the PFNGX (3, 6, 9, 12) series of exciton-donor CPEs were synthesized.

1.2 Synthesis

1.2.1 Synthetic Overview

Suzuki coupling was used to synthesize a series of exciton-donor polyfluorene-based alternating copolymers. Suzuki coupling forms a new carbon-carbon bond between the aryl groups of aryl halides and aryl boronic acids in the presence of a palladium catalyst.[26] The general reaction scheme for a Suzuki coupling reaction is shown in **Figure 1.4**.

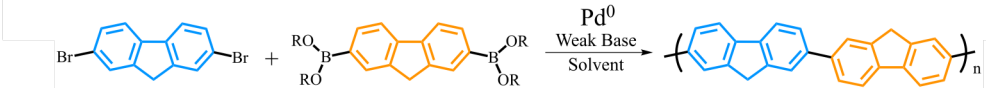

Figure 1.4 General Suzuki coupling reaction between 2,7-dibromo-fluorene and bis-(2,7-boronic-ester)-fluorene.

The polyfluorene-based alternating copolymer was formed between a diborylated fluorene monomer with bis-(trimethyl propyl ammonium) pendant side chains and a dibrominated fluorene monomer with bis- (oEG) side chains with 3, 6, 9, or 12 EG units. After functionalization of each dibrominated fluorene monomer, one of the monomers needed to be borylated. Dibrominated (3,3'-dimethylamino-1-propyl) fluorene (*FN*) was borylated due to being common amongst all PFNGX polymers. Along with the practicality of borylating the common monomer, the dibrominated fluorene monomer functionalized with oEG side chains with 6 EG units (*FG6*) created a mixture of borylated products that was not separable. The following sections describe

the mechanism of tosylation, the catalytic cycle of Miyaura borylation, and the catalytic cycle of Suzuki coupling reactions.[26,27]

1.2.2 Functional Group Conversion

The preparation of reagents to enhance reactivity and obtain higher yields through increased reaction efficiency is very important. Alcohols are common functional groups that need to be converted to better leaving groups.[28] Functional group conversion of primary and secondary alcohols with *p*-toluenesulfonyl chloride (*TsCl*) forms a tosylate, an excellent leaving group.

Specifically, tosylation of oEG monomethyl ether was carried out with TsCl to form oEG monomethyl ether *p*-toluene sulfonate (*TGX*) with (X = 3, 6, 9, or 12). This functional group conversion proceeds through deprotonation of the hydroxyl group, and subsequent nucleophilic attack at the sulfur atom, with concomitant release of chloride. The mechanism for this reaction is shown in **Figure 1.5**.[28] Use of hydroxyl group conversion to the tosylate is heavily relied upon in this dissertation.

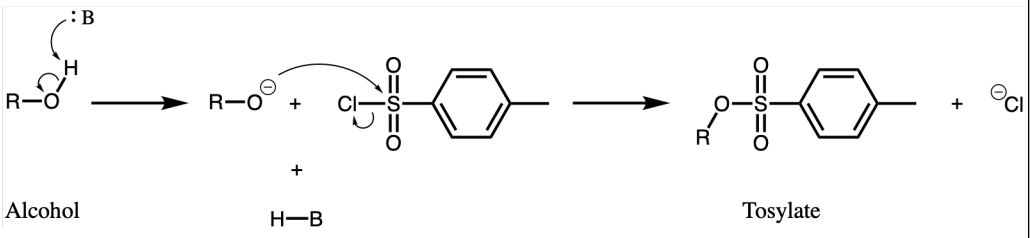

Figure 1.5 Mechanism for hydroxyl group interconversion with *p*-toluenesulfonyl chloride to form tosylate.

1.2.3 Miyaura Borylation Reactions

The Miyaura borylation converts aryl bromides into aryl boronic acids or aryl boronic esters depending on the boron reagent. This extremely important reaction is used to prepare reagents for use in Suzuki cross-couplings. The Miyaura borylation is crucial in the synthesis of the PFNGX series, herein used to convert FN, into the diborylated analog (*FNB*).[26,29,30]

Miyaura borylations are catalytic in palladium to form of the aryl boronic acids or aryl boronic esters. Reduction of a palladium(II) precatalyst is needed to form an activated palladium(0) species.[27] The activated catalyst has an unsaturated coordination sphere which is able to host other species.[27] In this dissertation [1,1'-bis(diphenylphosphino)-ferrocene]dichloropalladium(II) (*Pd(dppf)Cl*$_2$) is used exclusively because of its stability in air and precedent for borylation of fluorene monomers.[25,30] A palladium precatalyst with a bidentate phosphorous-based ligand has been experimentally shown to undergo reduction of palladium with concomitant oxidation of the boron-boron bond.[27]

The general catalytic cycle for Miyaura borylation with a simplified palladium(0) catalyst, aryl halide, bis(pinacolato)diboron (B_2Pin_2), and a weak base is shown in **Figure 1.6**.[26] In the first step of the catalytic reaction mechanism, known as oxidative addition, an unsaturated palladium(0) complex uses two of its electrons and oxidatively inserts itself between an sp^2 carbon-halogen bond. In this step, the palladium catalyst changes oxidation state from 0 to II, while acquiring two additional bonds, one to an

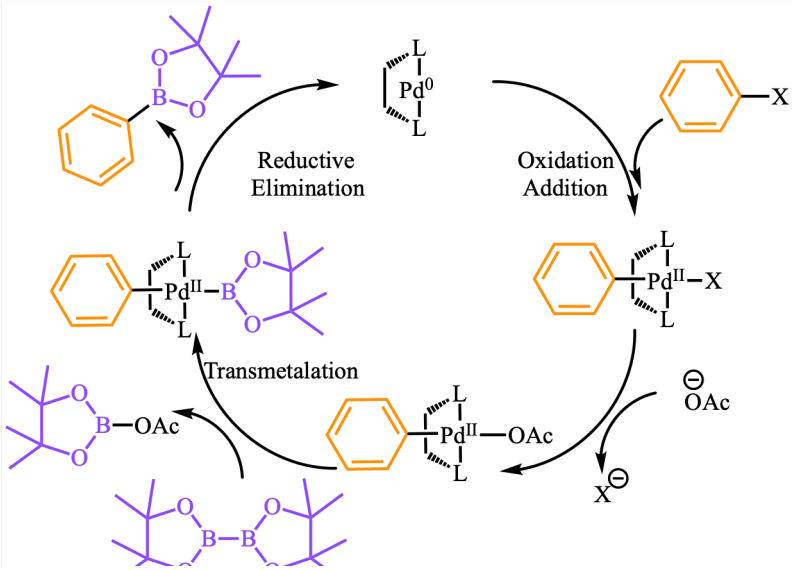

Figure 1.6 Miyaura borylation catalytic cycle with simplified activated palladium catalyst ($L_2Pd(0)$), aryl halide (Ar-X), bis(pinacolato)diboron (B_2Pin_2), and weak base (KOAc).[29]

aryl sp^2 carbon and the other to a halogen atom.[26] The second step in the catalytic cycle is that an acetate moiety replaces the halogen bound to the palladium catalyst.[26]

Transmetalation is the next step in the catalytic cycle and is the process by which the acetate on the palladium catalyst is swapped for a boron-containing compound. A purposed transmetalation transition state between palladium catalyst with acetate and B_2Pin_2 is shown in **Figure 1.7**. The carbonyl of the acetate moiety associates with the open p-orbital of boron. The electrons that form the boron-boron bond in diboronic ester are used to bond pinacol boronic ester with palladium. The bond between the oxygen of acetate and palladium breaks and forms a new carbon-oxygen double bond.

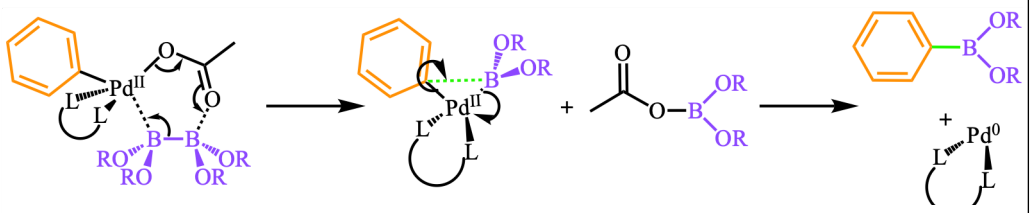

Figure 1.7 Transmetalation and reductive elimination for Miyaura borylation catalytic cycle between generic aryl palladium(II) acetate adduct and generic diboronic ester. The green solid line indicating the newly formed carbon- boron bond.[26,27]

Simultaneously, the double bond of the original carbonyl of acetate breaks and is used to bond with boron.

In the fourth step of the catalytic cycle, the boron-containing compound forms a bond to the aryl group. This occurs through what is known as reductive elimination, in which the palladium atom's oxidation state changes from II back to 0.[26,27,29] This occurs concomitantly with dissociation from the boron atom and the sp^2 carbon atom, to form a bond between the sp^2 carbon and the boron atom of the pinacol boronic ester.[29]

In this dissertation, borylation occurred through the use B_2Pin_2. When B_2Pin_2 is used alongside a base and a bisphosphine Pd(II) species such as $Pd(dppf)Cl_2$, rapid reduction of ligated Pd(II) to ligated Pd(0) occurs. Additionally, pinacol boronic ester is beneficially used as a masking group to stabilize the boryl group and increase the shelf life of the Miyaura borylation product. Moreover, the methyl protons on the pinacol ester show a distinct signal in nuclear magnetic resonance (*NMR*) spectroscopy and are very useful in verifying that the substrate was borylated. However, this reagent

suffers due to low atom economy. Specifically, the pinacol does not end up in the cross-coupled product and is not even utilized in the cross-coupling. More about this last point will be discussed in the dedicated section on Suzuki coupling.[26,27,29]

1.2.4 Suzuki Coupling Reactions

Suzuki coupling is an important reaction pathway used to form sp^2 carbon-carbon bonds. It is utilized in the synthesis of PFNGX CPE series via coupling FNB with FGX (X = 3, 6, 9, 12) in the presence of a palladium catalyst and a carbonate base. The catalytic cycle for Suzuki- Miyaura coupling is very similar to Miyaura borylation and is shown in **Figure 1.8**.

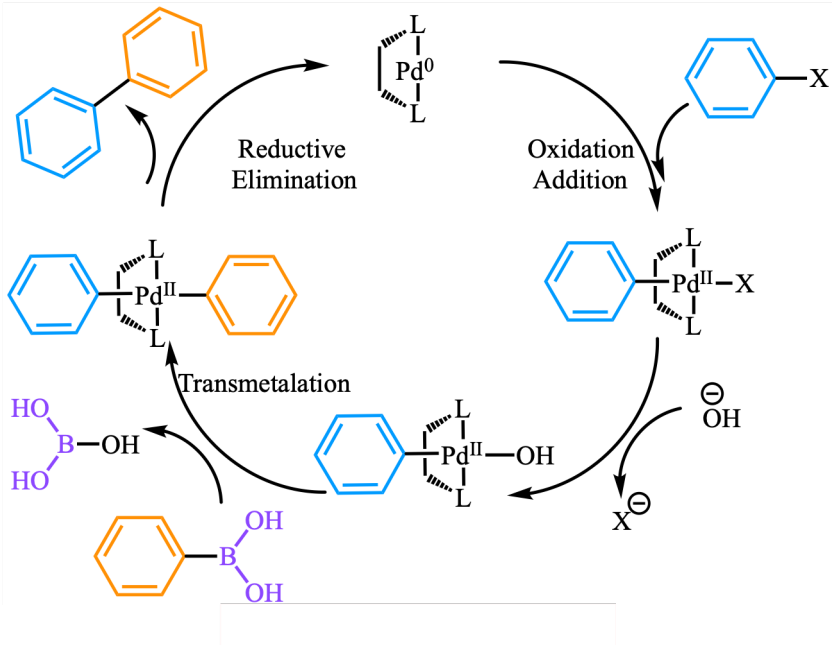

Figure 1.8 Suzuki catalytic cycle with simplified activated palladium catalyst ($L_2Pd(0)$), aryl halide (Ar-X), and aryl boronic ester (Ar-$B(OH)_2$).[29]

Some aryl boronic esters do not facilitate Suzuki transmetalation and must be converted into the analogous boronic acids for coupling to occur. This is true for the aryl pinacol boronic ester used in this dissertation.[31] Specifically, the methyl groups on the pinacol boronic ester are too sterically demanding for efficient bonding between the oxygen atom of the pinacol and the ligated palladium(II) catalyst. For Suzuki coupling to occur, the pinacol ester must be removed and converted into a boronic acid species under basic aqueous conditions.[31] Shown in **Figure 1.9** is a schematic for cross-coupling between a generic aryl palladium(II) adduct and a generic aryl boronic acid species capable of transmetalation.

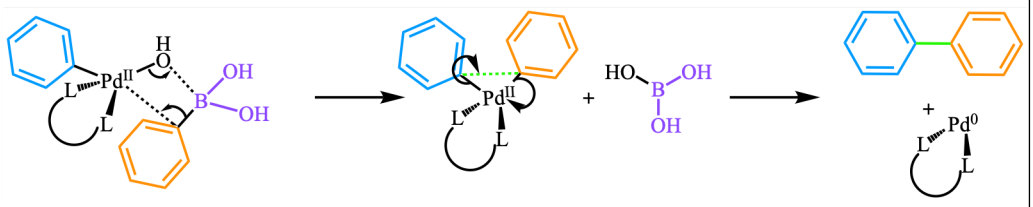

Figure 1.9 Suzuki coupling between generic aryl palladium(II) hydroxide adduct and generic aryl boronic acid. The green dashed lines represent bonds that are in the process of forming, with the green solid line indicating the newly formed sp^2 carbon- carbon bond.[31]

The mechanistic details regarding the role of the base in the transmetalation step of Suzuki coupling has been debated for many years. However, the oxo-palladium pathway, which is shown in **Figure 1.9**, has been experimentally determined as kinetically favored in comparison to the boronate and the oxo-palladium boronate pathways. Each of these aforementioned pathways have a trihydroxyboronate species

that has been regarded as detrimental to the coupling process by not allowing transmetalation to occur through the 4-membered transition state.[26]

1.3 Characterization Techniques

1.3.1 Overview

Photophysical characterization of isolated chains of PFNGX (3, 6, 9) in aqueous solution was carried out to determine the influence of the EG chain length on the optical properties and chain microstructure. Absorption spectroscopy was used to investigate the spectral shift between the fluorene monomers and their polymeric form, as well as verify that the optical density (*OD*) was below 0.1 to insure the validity of the photoluminescence (*PL*) measurements. Steady-state PL measurements were used to gain insight into the fundamental optical properties, and was used to estimate the relative microstructure of isolated PFNGX chains in aqueous solution.

Oppositely charged artificial light-harvesting CPECs were formed between PFNGX and poly(butyl-carboxylate)-thiophene (*PTAK*) at three molar charge ratios to interrogate the effect of EG chain length of PFNGX (3, 6, 9) series on the evolution of complexation and EET. More specifically, the aforementioned complexation was done to interrogate whether beyond a certain length of oEG sidechain, complexation and EET will be hindered. Absorption spectroscopy was also carried out on dilute solutions of CPEC to determine the optical absorption profiles for each component in solution. Just as was done for the isolated chains of PFNGX, absorption measurements were

carried out to verify whether the concentration of each component was dilute enough to provide trustworthy PL data. Exciton-donor PL quenching experiments were also carried out for the CPECs formed between PFNGX (3, 6, 9) and PTAK at three molar charge ratios to measure the evolution of exciton-donor PL quenching. Photoluminescence excitation (*PLE*) measurements were carried out on dilute solutions of CPEC to interrogate if EET occurred; radiative emission was enhanced when PFNGX was excited directly. The next sections will detail the important concepts of the aforementioned techniques used to characterize the photophysical properties and microstructure of isolate chains of PFNGX (3, 6, 9) and respective CPECs.

1.3.2 Absorption Spectroscopy

The interaction between electromagnetic radiation and matter is interrogated with spectroscopic techniques. Organic molecules have a subset of molecular orbitals that are filled with electrons which may become promoted to higher-lying unoccupied molecular orbitals upon the interaction with electromagnetic radiation.[17] This interaction is an absorption process when a subset of wavelengths is absorbed by the molecule and promotes ground state electrons to energetically higher unoccupied molecular orbitals. The absorption cross-section σ and molar extinction coefficient ε_A are experimental parameters that describe the strength of a molecules absorption process and are shown in Equation 1.7 and Equation 1.8,[17]

$$I(\omega, \ell) = I(\omega, 0)e^{-\sigma(\omega)\ell N} \tag{1.7}$$

$$I(\omega, \ell) = I(\omega, 0)10^{-\varepsilon_A(\omega)\ell C_M} \quad (1.8)$$

where, $I(\omega, 0)$ is the frequency-dependent incident light intensity before interacting with the sample, $I(\omega, \ell)$ is the frequency-dependent incident light after interacting with the sample a distance ℓ into the sample in cm, and ω is the frequency of the incoming radiation. In Equation 1.7, N is the concentration of the solute and has units of molecules per cubic centimeter, whereas σ is the absorption cross-section, which has units of square centimeters per molecule. While Equation 1.8, is written in terms of molar extinction coefficient ε_A and has units of $L \cdot mol^{-1} \cdot cm^{-1}$. Additionally, the concentration of absorbers C_M has units of moles per liter.

Rearrangement of Equation 1.8, leads to the formation of Equation 1.9,[17]

$$\log\left[\frac{I(\omega,0)}{I(\omega,\ell)}\right] = \varepsilon_A(\omega)\ell C_M \quad (1.9)$$

and allowing $\log\left[\frac{I(\omega,0)}{I(\omega,\ell)}\right]$ to equal the absorbance A, one obtains a familiar equation: the Beer-Lambert law represented by Equation 1.10.[17]

$$A = \varepsilon_A(\omega)\ell C_M \quad (1.10)$$

1.3.3 Photoluminescence Spectroscopy

Absorption of a photon by a molecule leads to promotion of an electron to a higher-lying state. The excited electron will eventually relax back to the ground state via non-radiative and radiative emission. E_1 represents the ground electronic state and E_2

represents the first electronic excited state; each with respective number densities N_1 and N_2: R_{12} and R_{21} are per-unit-volume rates for upward and downward transitions respectively.[17] Upward transitions can occur via absorption of electromagnetic radiation, whereas downward transitions occur via both stimulated and spontaneous emission. The rate of upward transition R_{12} is shown in Equation 1.11, where B_{12} is the rate constant for absorption and $\rho_{rad}(\omega)$ represents the energy density of the incident electromagnetic field.[17]

$$R_{12} = N_1 B_{12} \rho_{rad}(\omega) \tag{1.11}$$

The rate of downward transition, R_{21} is shown with Equation 1.12, where B_{21} is the rate constant for stimulated emission and A_{21} is the rate constant for spontaneous emission. The total downward transition rate is the sum of stimulated and spontaneous emission rates.[17]

$$R_{21} = N_2 B_{21} \rho_{rad}(\omega) + N_2 A_{21} \tag{1.12}$$

Rate constants B_{12}, B_{21}, and A_{21} are known as the Einstein coefficients. Both B_{12} and B_{21} depend on the energy density at the transition frequency (ω) and where A_{21} is independent of the electromagnetic radiation.[17]

The ratio of the populations of the two states obeys the Boltzmann distribution when observed at thermal equilibrium as per Equation 1.13,[17]

$$\frac{N_2}{N_1} = \exp\left[\frac{-(E_2 - E_1)}{k_B T}\right] = \exp\left[\frac{-\hbar\omega}{k_B T}\right] \tag{1.13}$$

where, $\hbar$ is the reduced Plank's constant, T is temperature in units of Kelvin, and k_B is the Boltzmann constant. At equilibrium the total upward transition rate from some energy level is equal to the total downward transition to that level. This condition yields Equation 1.14.[17]

$$\rho_{rad}(\omega) = \left[\frac{A_{21}}{B_{12}\exp(\hbar\omega/k_BT) - B_{21}}\right] \tag{1.14}$$

Next, an expression for the Einstein coefficients can be related to molecular properties and observables, and therefore a frequency-dependent upward transition rate per molecule for randomly oriented absorbers can be shown as Equation 1.15,[17]

$$R_{12}^{(1)} = \frac{\pi|\mu_{21}|^2}{3n^2\varepsilon_0\hbar^2}\,\rho_{rad}(\omega) \tag{1.15}$$

If Equation 1.15 is multiplied by the number density of molecules in state E_1 and is set equal to Equation 1.11, the following relation is acquired and is shown via Equation 1.16.[17]

$$B_{21} = \frac{\pi|\mu_{21}|^2}{3n^2\varepsilon_0\hbar^2} \tag{1.16}$$

Equation 1.17 shows a relation between B_{21} and A_{21}.

$$\frac{A_{21}}{B_{21}} = \frac{\hbar n^3\omega^3}{\pi^2c^2} \tag{1.17}$$

Therefore, Equation 1.16 rewritten in terms of A_{21} and the transition dipole moment is shown with Equation 1.18.[17]

$$A_{21} = \frac{n\omega^3|\mu_{21}|^2}{3\pi\varepsilon_0\hbar c^3} \quad (1.18)$$

In this equation, the units for A are inverse seconds, n is the frequency dependent refractive index of the medium, ε_0 is the permittivity of free space, and c is the speed of light.[17]

The energy of a photon in the wavelengths of the visible spectrum is about 100 times greater than k_BT, and therefore when a photon with this magnitude of energy is absorbed, the excited molecule will need to redistribute its energy to return to thermal equilibrium. When the amount of energy absorbed promotes an electron from the ground state into a higher-lying electronic and vibrational state, multiple processes can dissipate the absorbed energy.[17] There are five processes that a molecule in the excited state can utilize to dissipate energy; three non-radiative and two radiative. The three non-radiative processes are intramolecular vibrational relaxation (*IVR*), internal conversion (*IC*), and intersystem crossing (*ISC*). The two radiative processes include fluorescence (photoluminescence) and phosphorescence. A useful way to visualize these processes is through a Jablonski diagram, which is shown in **Figure 1.10**.[17]

The diagram is read from the bottom left starting with an organic molecule that exists in the ground electronic and vibrational states at room temperature. This molecule is shown to be in a ground-state closed-shell singlet, S_0. Upon photon absorption, an electron from S_0 will be promoted into an excited vibrational level of an excited singlet excited state S_n. For the purpose of exploring each of the possible

relaxation processes, the excited state was chosen to be the second excited singlet state, S_2.

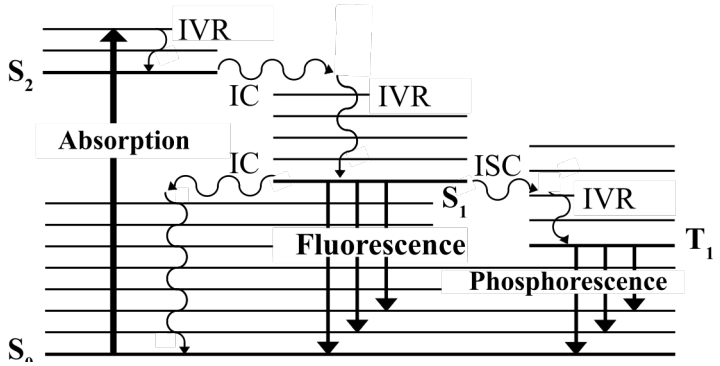

Figure 1.10 Jablonski diagram showing absorption processes, intramolecular vibrational relaxation (*IVR*), internal conversion (*IC*), intersystem crossing (*ISC*), fluorescence, and phosphorescence.

This diagram will be used to illustrate the different transitions among ground and excited states.[17] A highly probable outcome of this excitation is to stay in the S_2, undergo IVR by redistribution of vibrational energy from an excited vibrational level to a lower vibrational level, and subsequently give up that amount of energy to its surroundings. For larger organic molecules, the time scale of this process is on the order of a few picoseconds (ps). This is compared to light emission, which occurs on hundreds of ps to 1 ns timescales.

A transition between two electronic states with the same spin multiplicity is known as internal conversion. It competes with or immediately follows IVR. Figure 1.10 shows that once the excited state becomes vibrationally relaxed to the ground

vibrational level of S_2, IC may occur between S_2 and a vibrationally excited state of the next lower electronic excited state, S_1. This transition is a competitive process to that of IVR because it often occurs on a picosecond timescale.[17]

Once relaxed to the lowest vibrational state of S_1, three processes can occur, IC to a very highly excited vibrational level of S_0, ISC to a high lying vibrational state of an electronic state with different spin multiplicity T_1, or direct fluorescence to the lowest electronic state S_0. All three of these processes compete, but usually the dominant process for redistribution of energy is fluorescence from S_1 to S_0. Fluorescence can occur between the lowest vibrational state of S_1 to the ground vibrational level, first excited vibrational level, or second excited vibrational level of the electronic ground state S_0. Internal conversion from the ground vibrational state of S_1 to a very highly excited vibrational level of S_0 is unlikely because the transition is slow due to being a transition between widely different vibrational quantum numbers.[17]

Intersystem crossing is not competitive because of slow timescales varying from picoseconds to microseconds. Optical transitions between singlet and triplet states are also weak due to spin selection rules. However, if ISC does occur from the ground vibrational level of S_1 to a higher-lying vibrational level of T_1, then just like with IC from S_2 to a higher-lying vibrational level of S_1, the process is followed by IVR to the lowest vibrational level of that electronic excited state. Lastly, once in T_1, phosphorescence can occur, albeit very slowly, which takes the excited triplet back down to the ground electronic state.[17]

Michael Kasha and co-workers detailed spectroscopic observables for aggregated dye molecules; this model has been expanded upon to yield a diagnostic tool to infer the average microstructure of a polymer.[15,32,33] The main premise is that a monomer's transition dipole moment can couple constructively or destructively with nearby transition dipole moments. Kasha and co-workers argue that coulombic coupling between transition dipole moments can be treated as a vector sum.[32] Coupling leads to a splitting of the first excited state, and is shown in **Figure 1.11**.[32]

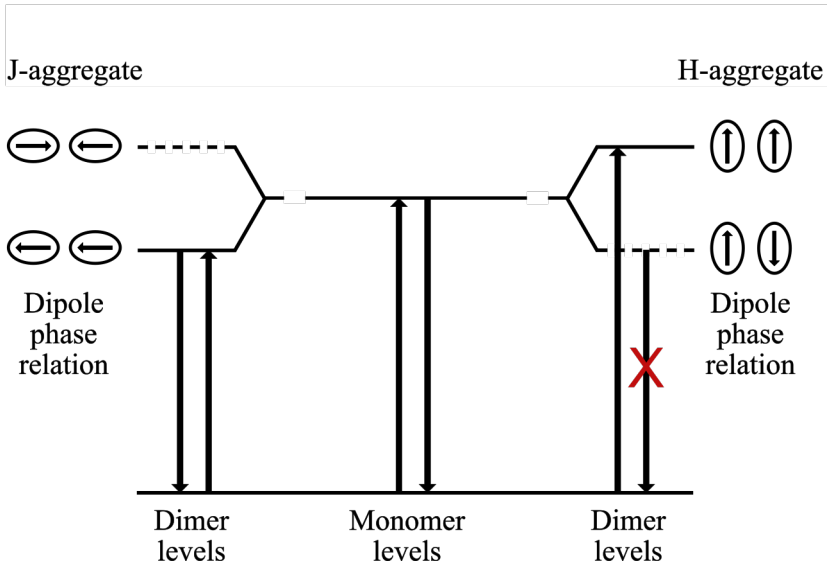

Figure 1.11 Energy level diagram for Kasha's J- and H- aggregate (dimer) model. Solid lines represent energy levels with allowed transitions that couple to the ground state. Dashed black lines represent energy levels with disallowed transitions that do not couple with the ground state.

Either the head-to-tail or head-to-head combination of transition dipole moments occupy the upper state, and depends on the sign of the coulombic coupling term J_{Coul}. A mathematical approximation of J_{Coul} is given by Equation 1.19,[33]

$$J_{Coul} \approx \frac{\mu^2(1-3\cos^2\theta)}{4\pi\varepsilon R^3} \qquad \text{Equation 1.19}$$

where, μ is the transition dipole moment of identical chromophores, R is the intermolecular distance between mass centers, and θ is the angle between μ and R.[33] Depending on the orientation of and the angle between each transition dipole moment, the coulombic coupling term J_{Coul} changes sign, which in turn dictates whether the non-zero (symmetric) combination of transition dipole moments occupies the upper or lower state. These two scenarios arise from differences in θ.[15]

The excited state associated with the anti-symmetric combination of transition dipole moments does not couple to the ground state because the total transition dipole moment for that excited state is zero.[15,32,33] If the anti-symmetric state occupies the lower of the two excited states, radiative emission from the lowest vibrational level of the anti-symmetric excited state to the lowest vibrational level of the ground state is restricted. If the lowest excited state corresponds to the symmetric combination of transition dipole moments, then radiative emission is not restricted.[15,32,33] The spectroscopic observable to determine the angle between nearby transition dipole moments is the relative oscillator strength of the 0-0 transition compared with the oscillator strength of the 0-1 transition. Applied to polymeric systems, if the ratio of oscillator strengths between the 0-0 transition and the 0-1 transition is greater than 1; the backbone of the polymer is more extended and is described as a J-aggregating polymer chain. If the ratio of oscillator strengths between the 0-0 transition and the 0-

1 transition is less than 1, the polymer has a coiled microstructure and is described as an H-aggregating polymer chain.[15,32,33]

1.3.4 Photoluminescence Excitation Spectroscopy

PLE measurements were used to detect EET between PFNGX (donor) and PTAK (acceptor); the observable for this was whether radiative emission from PTAK in a CPEC was enhanced when PFNGX was directly excited. This measurement involves excitation in a range of wavelengths and detects emission at a single wavelength. Therefore, by exciting wavelengths that are primarily ascribed to PFNGX only, and detecting radiative emission at a wavelength associated with radiative emission from PTAK only, unambiguous evidence of EET can be observed. Each exciton-donor polymer was complexed with PTAK at 3 molar charge ratios to observe the evolution of EET. The chosen ratios, spanned a range from low molar charge ratio of acceptor, to molar charge ratios of acceptor that approached ionic stoichiometry.

The overall functional form of the excitation intensities in a PLE measurement often takes a similar functional form as the absorption profile obtained with absorption spectroscopy.[34] This is because the intensity of radiative emission at an excitation wavelength correlates well with the excited state population at that excitation wavelength.

1.3.5 Time-Resolved Photoluminescence Spectroscopy

Time-resolved photoluminescence (*TRPL*) spectroscopy is a technique used to help elucidate the photoluminescence (fluorescence) lifetimes of an emitter. TRPL measurements were carried out on isolated polymer chains of PFNGX (3, 6, 9) in aqueous media to elucidate the fluorescence lifetimes. The emission rate will depend on the rate of depopulation from the excited state to the ground state with a rate constant of A_{21}. This relationship is shown in Equation 1.20.[17]

$$N_2(t) = N_2(0)\exp(-A_{21}t) \tag{1.20}$$

Taking the inverse of the rate constant for spontaneous emission yields τ_{rad}, which is the natural radiative lifetime. When the excited state undergoes spontaneous emission, the radiative lifetime can be written in terms of the transition dipole moment using Equation 1.21.[17]

$$\tau_{rad} = \frac{1}{A_{21}} = \frac{3\pi\varepsilon_0\hbar c^3}{n\omega^3|\mu_{21}|^2} \tag{1.21}$$

For the condition of spontaneous emission from an excited state to more than one lower energy state j; depopulation of state 2 with respect to time is equal to the rate constant for spontaneous emission to each state j, multiplied by the number density of the emitting excited state summed over each state j.[17] This relation is shown in Equation 1.22.

$$\frac{-dN_2}{dt} = \sum_j A_{2j}N_2 \tag{1.22}$$

Similarly, Equation 1.23 has a functional form of a decreasing exponential.

$$N_2(t) = N_2(0)\exp\left(^{-t}/_{\tau_{rad}}\right) \quad (1.23)$$

The natural radiative lifetime can be expressed with Equation 1.24 as the inverse of the spontaneous emission rate constants summed over j final states.[17]

$$\tau_{rad} = 1/\sum_j A_{2j} \quad (1.24)$$

1.4 Conclusion

The introductory chapter in this dissertation has served to bring the audience up to speed with the concepts, techniques, and methodologies needed to complete the experimental work in the following three chapters. Section 1.1 discussed the overarching reasons why CPEs were utilized as the primary material to carry out light-harvesting investigations. Some points that were touched upon are the electronic structure and structure-property relationships of CPEs, electronic transitions, solubilization of CPEs, CPE complexation, and FRET.

In section 1.2, the background synthetic information and concepts that were utilized in this dissertation were explored. The section began with discussion of the functional group conversion of hydroxy group tosylation. The next two sections covered Miyaura borylation reactions and Suzuki coupling reactions. The purpose of this section was to prime the audience with relevant synthetic knowledge to enable reasoning as to why the following reactions were carried out to synthesize the PFNGX chemical series

utilized in this dissertation. Chapter 2 describes the procedures and results of PFNGX (3, 6, 9, 12) synthesis.

Many different characterization techniques used to study CPEs and CPECs were discussed in section 1.3. Photophysical characterization techniques were discussed such as absorption, photoluminescence, photoluminescence excitation, and time-resolved photoluminescence spectroscopies. These characterization techniques were at the crux of the experiments carried out to determine the optical properties and polymer chain microstructure of the synthesized CPEs. Characterization of CPECs was carried out to ultimately determine whether beyond a certain length of oEG sidechain, complexation and EET would be hindered. This aspect will be covered in more detail in chapter 3.

In chapter 4, synchrotron-based small angle X-ray scattering measurements to elucidate the morphology of polymer thin films are discussed. The two main characterization techniques utilized in this chapter are grazing incidence X-ray diffraction (*GIXD*) and resonant elastic X-ray scattering (*REXS*). GIXD measurements were carried out to interrogate the π-stacking and lamellar distances between polymer chains, as well as the distribution of orientations of polymer crystallites in thin films. REXS measurements were carried out to determine nanometer length-scales of donor-acceptor polymer/small-molecule acceptor thin films. Each of these techniques along with detailed analysis will be covered in chapter 4.

1.5 References

(1) O'Neill, B. C.; Oppenheimer, M.; Warren, R.; Hallegatte, S.; Kopp, R. E.; Pörtner, H. O.; Scholes, R.; Birkmann, J.; Foden, W.; Licker, R.; Mach, K. J.; Marbaix, P.; Mastrandrea, M. D.; Price, J.; Takahashi, K.; Ypersele, J.-P. van; Yohe, G. IPCC Reasons for Concern Regarding Climate Change Risks. *Nat Clim Change* 2017, *7* (1), 28–37. https://doi.org/10.1038/nclimate3179.

(2) Devabhaktuni, V.; Alam, M.; Depuru, S. S. S. R.; Green, R. C.; Nims, D.; Near, C. Solar Energy: Trends and Enabling Technologies. *Renew Sustain Energy Rev* 2013, *19*, 555–564. https://doi.org/10.1016/j.rser.2012.11.024.

(3) McCann, M. J.; Catchpole, K. R.; Weber, K. J.; Blakers, A. W. A Review of Thin-Film Crystalline Silicon for Solar Cell Applications. Part 1: Native Substrates. *Sol Energ Mat Sol C* 2001, *68* (2), 135–171. https://doi.org/10.1016/s0927-0248(00)00242-7.

(4) Zhang, B.; Jie, J.; Zhang, X.; Ou, X.; Zhang, X. Large-Scale Fabrication of Silicon Nanowires for Solar Energy Applications. *Acs Appl Mater Inter* 2017, *9* (40), 34527–34543. https://doi.org/10.1021/acsami.7b06620.

(5) Mirkovic, T.; Ostroumov, E. E.; Anna, J. M.; Grondelle, R. van; Govindjee; Scholes, G. D. Light Absorption and Energy Transfer in the Antenna Complexes of Photosynthetic Organisms. *Chem Rev* 2017, *117* (2), 249–293. https://doi.org/10.1021/acs.chemrev.6b00002.

(6) Scholes, G. D.; Fleming, G. R.; Olaya-Castro, A.; Grondelle, R. van. Lessons from Nature about Solar Light Harvesting. *Nat Chem* 2011, *3* (10), 763–774. https://doi.org/10.1038/nchem.1145.

(7) Hollingsworth, W. R.; Lee, J.; Fang, L.; Ayzner, A. L. Exciton Relaxation in Highly Rigid Conjugated Polymers: Correlating Radiative Dynamics with Structural Heterogeneity and Wavefunction Delocalization. *Acs Energy Lett* 2017, *2* (9), 2096–2102. https://doi.org/10.1021/acsenergylett.7b00535.

(8) Hollingsworth, W. R.; Segura, C.; Balderrama, J.; Lopez, N.; Schleissner, P.; Ayzner, A. L. Exciton Transfer and Emergent Excitonic States in Oppositely-Charged Conjugated Polyelectrolyte Complexes. *J Phys Chem B* 2016, *120* (31), 7767–7774. https://doi.org/10.1021/acs.jpcb.6b06533.

(9) Hollingsworth, W. R.; Magnanelli, T. J.; Segura, C.; Young, J. D.; Bragg, A. E.; Ayzner, A. L. Polyion Charge Ratio Determines Transition between Bright and Dark

Excitons in Donor/Acceptor-Conjugated Polyelectrolyte Complexes. *J Phys Chem C* 2018, *122* (39), 22280–22293. https://doi.org/10.1021/acs.jpcc.8b06195.

(10) Hollingsworth, W. R.; Williams, V.; Ayzner, A. L. Semiconducting Eggs and Ladders: Understanding Exciton Landscape Formation in Aqueous Π-Conjugated Inter-Polyelectrolyte Complexes. *Macromolecules* 2020, *53* (7), 2724–2734. https://doi.org/10.1021/acs.macromol.0c00029.

(11) Clark-Winters, T. L.; Bragg, A. E. Control of Photoinduced Charge Separation in Conjugated Polyelectrolyte Complexes through Microstructure-Dependent Exciton Delocalization. *J Phys Chem C* 2021, *125* (42), 22982–22997. https://doi.org/10.1021/acs.jpcc.1c06276.

(12) Johnston, A. R.; Perry, S. L.; Ayzner, A. L. Associative Phase Separation of Aqueous Π-Conjugated Polyelectrolytes Couples Photophysical and Mechanical Properties. *Chem Mater* 2021, *33* (4), 1116–1129. https://doi.org/10.1021/acs.chemmater.0c02424.

(13) Wang, H.; Lu, P.; Wang, B.; Qiu, S.; Liu, M.; Hanif, M.; Cheng, G.; Liu, S.; Ma, Y. A Water-Soluble Π-Conjugated Polymer with up to 100 Mg · ML−1 Solubility. *Macromol Rapid Comm* 2007, *28* (16), 1645–1650. https://doi.org/10.1002/marc.200700221.

(14) Hedley, G. J.; Ruseckas, A.; Samuel, I. D. W. Light Harvesting for Organic Photovoltaics. *Chem Rev* 2017, *117* (2), 796–837. https://doi.org/10.1021/acs.chemrev.6b00215.

(15) Spano, F. C.; Silva, C. H- and J-Aggregate Behavior in Polymeric Semiconductors. *Annual Reviews Physical Chemistry* 2014.

(16) Hoffmann, R. How Chemistry and Physics Meet in the Solid State. *Angewandte Chemie Int Ed Engl* 1987, *26* (9), 846–878. https://doi.org/10.1002/anie.198708461.

(17) Kelley, A. M. *Condensed-Phase Molecular Spectroscopy and Photophysics*; John Wiley & Sons, Inc.: Hoboken, New Jersey, 2013.

(18) Alvarado, S. F.; Seidler, P. F.; Lidzey, D. G.; Bradley, D. D. C. Direct Determination of the Exciton Binding Energy of Conjugated Polymers Using a Scanning Tunneling Microscope. *Phys Rev Lett* 1998, *81* (5), 1082–1085. https://doi.org/10.1103/physrevlett.81.1082.

(19) Knupfer, M. Exciton Binding Energies in Organic Semiconductors. *Appl Phys* 2003, *77* (5), 623–626. https://doi.org/10.1007/s00339-003-2182-9.

(20) Takeda, N.; Asaoka, S.; Miller, J. R. Nature and Energies of Electrons and Holes in a Conjugated Polymer, Polyfluorene. *J Am Chem Soc* 2006, *128* (50), 16073–16082. https://doi.org/10.1021/ja062596h.

(21) Chabinyc, M. L. X-ray Scattering from Films of Semiconducting Polymers. *Polym Rev* 2008, *48* (3), 463–492. https://doi.org/10.1080/15583720802231734.

(22) Patel, S. N.; Chabinyc, M. L. Anisotropies and the Thermoelectric Properties of Semiconducting Polymers. *J Appl Polym Sci* 2016, *134* (3). https://doi.org/10.1002/app.44403.

(23) Sundararajan, P. R. *Polymer Self-Assembly*; John Wiley & Sons Inc., 2017; Vol. 1., pp 17-35.

(24) Braslavsky, S. E.; Fron, E.; Rodríguez, H. B.; Román, E. S.; Scholes, G. D.; Schweitzer, G.; Valeur, B.; Wirz, J. Pitfalls and Limitations in the Practical Use of Förster's Theory of Resonance Energy Transfer. *Photochem Photobio S* 2008, *7* (12), 1444–1448. https://doi.org/10.1039/b810620g.

(25) Meng, B.; Song, H.; Chen, X.; Xie, Z.; Liu, J.; Wang, L. Replacing Alkyl with Oligo(Ethylene Glycol) as Side Chains of Conjugated Polymers for Close π–π Stacking. *Macromolecules* 2015, *48* (13), 4357–4363. https://doi.org/10.1021/acs.macromol.5b00702.

(26) Lennox, A. J. J.; Lloyd-Jones, G. C. Selection of Boron Reagents for Suzuki–Miyaura Coupling. *Chem Soc Rev* 2013, *43* (1), 412–443. https://doi.org/10.1039/c3cs60197h.

(27) Wei, C. S.; Davies, G. H. M.; Soltani, O.; Albrecht, J.; Gao, Q.; Pathirana, C.; Hsiao, Y.; Tummala, S.; Eastgate, M. D. The Impact of Palladium(II) Reduction Pathways on the Structure and Activity of Palladium(0) Catalysts. *Angewandte Chemie Int Ed* 2013, *52* (22), 5822–5826. https://doi.org/10.1002/anie.201210252.

(28) Carey, F. A.; Giuliano, R. M. *Organic Chemistry*; McGraw-Hill: New York, NY, 2011; Vol. 8th., pp 347.

(29) Molander, G. A.; Trice, S. L. J.; Kennedy, S. M.; Dreher, S. D.; Tudge, M. T. Scope of the Palladium-Catalyzed Aryl Borylation Utilizing Bis-Boronic Acid. *J Am Chem Soc* 2012, *134* (28), 11667–11673. https://doi.org/10.1021/ja303181m.

(30) Pu, K.-Y.; Wang, G.; Liu, B. *Design and Synthesis of Conjugated Polyelectrolytes*; John Wiley & Sons Inc., 2013., pp 16-17.

(31) Thomas, A. A.; Zahrt, A. F.; Delaney, C. P.; Denmark, S. E. Elucidating the Role of the Boronic Esters in the Suzuki–Miyaura Reaction: Structural, Kinetic, and Computational Investigations. *J Am Chem Soc* 2018, *140* (12), 4401–4416. https://doi.org/10.1021/jacs.8b00400.

(32) Kasha, M.; Rawls, H. R.; El-Bayoumi, M. A. The Exciton Model in Molecular Spectroscopy. *Pure Appl Chem* 1965, *11* (3–4), 371–392. https://doi.org/10.1351/pac196511030371.

(33) Hestand, N. J.; Spano, F. C. Molecular Aggregate Photophysics beyond the Kasha Model: Novel Design Principles for Organic Materials. *Accounts Chem Res* 2017, *50* (2), 341–350. https://doi.org/10.1021/acs.accounts.6b00576.

(34) Wang, X.; Zardo, I.; Spirkoska, D.; Yazji, S.; Ng, K. W.; Ko, W. S.; Chang-Hasnain, C. J.; Finley, J. J.; Abstreiter, G. Valence Band Splitting in Wurtzite InGaAs Nanoneedles Studied by Photoluminescence Excitation Spectroscopy. *Acs Nano* 2014, *8* (11), 11440–11446. https://doi.org/10.1021/nn504512u.

Chapter 2

SYNTHESIS

2.1 Synthetic Overview

2.1.1 Methodology, Materials, and Measurements

Herein is described the synthetic procedures adapted to create the PFNGX series, polyfluorene-based copolymers used in this dissertation as exciton donors in CPECs. The reaction scheme for the synthesis of this series is shown in **Figure 2.1**.[1–6]

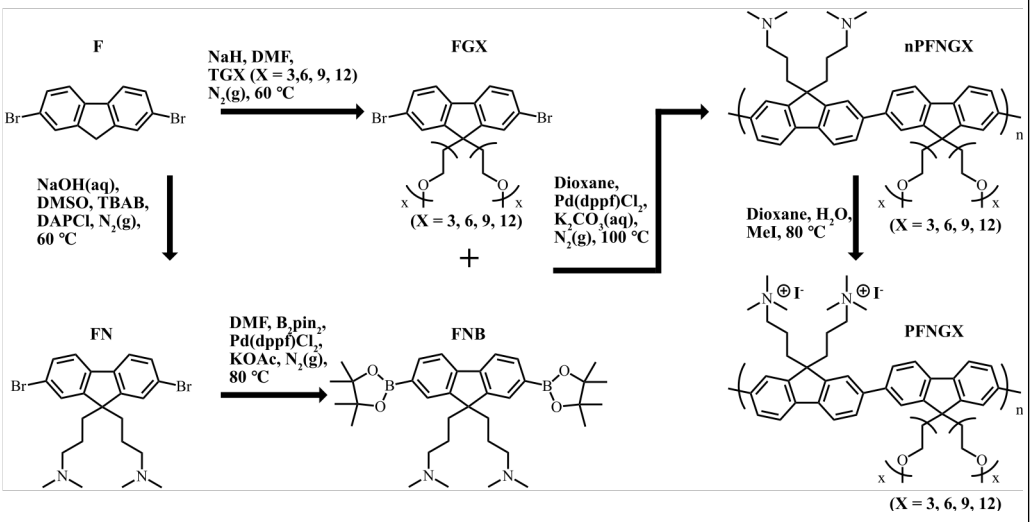

Figure 2.1 Synthetic scheme for PFNGX series.[1–6]

This series of A-B repeating polyfluorene copolymers, contain one co-monomer providing ionic functionality, and another co-monomer providing neutral side groups for enhancing the aqueous solubility of the CPE series.[1]

Before starting to actively synthesize the monomers, the first thing that was needed was to prepare the oligo ethylene glycol (*oEG*) reagents as the tosylates to create a more

reactive oEG reagent.[2] Next came attaching the oEG chains to the fluorene monomer, this was carried out by creating a nucleophilic fluorene species with a base and attacking the oEG at the carbon bearing the tosyl group.[3]

Reactions were then carried out to synthesize the amine-containing fluorene monomer. This was accomplished by turning the fluorene into a nucleophile with a base and having it attack dimethyl aminopropyl chloride hydrochloride. The fluorene nucleophile displaced the chloride on the propyl chain to append the dimethylamino propyl chain to the fluorene monomer.[4,5] Each of the two aforementioned nucleophilic reactions formed disubstituted fluorene monomers. Next, the amine-containing fluorene monomer (*FN*) was borylated via a Miyaura borylation reaction to form (*FNB*). Coupling between the fluorene with the oEG side chains (*FGX*) (X = 3, 6, 9, 12) and the borylated fluorene monomer (*FNB*) was carried out to form the neutral conjugated polyelectrolytes (*nPFNGX*) (X = 3, 6, 9, 12).[4,5] This was followed by *in situ* quaternization of the tertiary amine of nPFNGX with methyl iodide.[1,6]

Reagents and materials were used as received from the following distributors: 2,7-dibromofluorene and 4-toluenesulfonyl chloride were obtained from Oakwood Chemical. Poly[3-(potassium-4-butanoate)thiophene-2,5-diyl] regioregular was obtained from Rieke Metals. Bis(pinacolato)diboron >98% and 1,4-dioxane (anhydrous, 99.8%) were obtained from Alfa Aesar. Triethylene glycol monomethyl ether (>98.0%), hexaethylene glycol monomethyl ether (>96.0%), and nonaethylene glycol monomethyl ether (>93.0%) were obtained from TCI America Inc. Tetraethylammonium bromide 100% was obtained from Chem-Impex International

Inc. Palladium catalyst [1,1'-bis(diphenylphosphino)ferrocene] dichloropalladium (II), dimethyl aminopropyl chloride hydrochloride (96%), sodium hydride (60% dispersed in mineral oil), and dimethylformamide (anhydrous, 99.8%) were obtained from Sigma-Aldrich. Methyl iodide (99.5%), tetrahydrofuran (HPLC grade), and dichloromethane (99.5%) were obtained from Spectrum Chemical. Sodium hydroxide, sodium hydroxide solution (50% w/w), potassium carbonate (anhydrous, 99.7%), triethylamine (99%), diethyl ether (99%), methanol (99.9%), acetone (HPLC grade), chloroform (99.9%), ethyl acetate (99.5%), hexanes (98.5%), and potassium acetate (>99%) were obtained from Fisher Chemical. Dimethyl sulfoxide (99.7%) was obtained from Acros Organics. Chemglass pressure tubes were used for polymerizations (48 mL - part number CG-1880-04), and quaternization (350 mL - part number CG-1880-12). Polyvinylidene difluoride filters (450 nm) were obtained from Lab Safety Supply and polytetrafluoroethylene filters (450 nm) were obtained from Cole-Parmer. $CDCl_3$ (D 99.8%) and D_2O (D 99.9%) were both purchased from Cambridge Isotope Laboratories. Nuclear magnetic resonance (*NMR*) spectra of the monomers were collected on a Bruker Avance III HD 4 channel 500 MHz NMR, and spectra of the polymers were collected on a Bruker Avance III HD 4 channel 800 MHz NMR with a cryoprobe.

2.2 Preparation of Reagents

2.2.1 Reagent TG3

Synthesis of (1-(p-tosyl)-3,6,9- trioxodecane) To a clean and dried 25 mL round bottom flask placed in an ice bath, a Teflon coated stir bar, sodium hydroxide (*NaOH*, 683 mg, 17.1 mmol), deionized water (*DI H_2O*, 3.5 mL, 193.9 mmol), triethylene glycol monomethyl ether (*G3OH*, 1.00 g, 6.1 mmol), and tetrahydrofuran (*THF*, 7.0 mL, 86.3 mmol) were added and allowed to react for 30 minutes. Next, *p*-tolyl sulfonyl chloride (*PTSC*, 2.11 g, 11.1 mmol) was added under an atmosphere of nitrogen (N_2(g)) and reacted for 12 hours. Upon completion, the reaction contents were dumped into 8.7 mL of cold DI H_2O, followed by extraction of the product with dichloromethane (*DCM*, 2 x 4.5 mL). The organic layer was washed with DI H_2O (2 x 4.5 mL), brine (1 x 4.5 mL), and subsequently dried over sodium sulfate (Na_2SO_4). The anhydrous organic layer was decanted away from the drying agent and concentrated under reduced pressure to provide the product TG3 as a colorless oil (77 yield, 1.50 g).[2] **Figure 2.2**: TG3 ^{1}H NMR (500 MHz, $CDCl_3$): δ 7.79-7.77 (d, 2H), 7.33-7.31 (d, 2H), 4.14 (t, 2H), 3.67 (t, 2H), 3.59 (m, 2H), 3.57 (s, 4H), 3.51 (t, 2H), 3.35 (s, 3H), 2.43 (s, 3H) **Figure 2.3:** TG3 ^{13}C NMR (500 MHz, $CDCl_3$): δ 144.8, 133.1, 129.8, 128.0, 71.9, 70.7, 70.6, 69.3, 68.7, 59.0, 21.6.

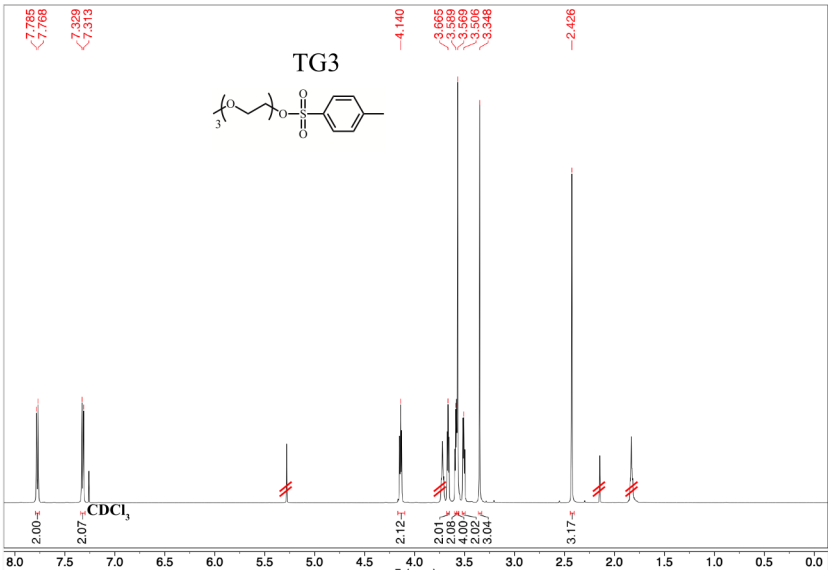

Figure 2.2 TG3 ^{1}H NMR with trace amount of *DCM, THF,* and Acetone.

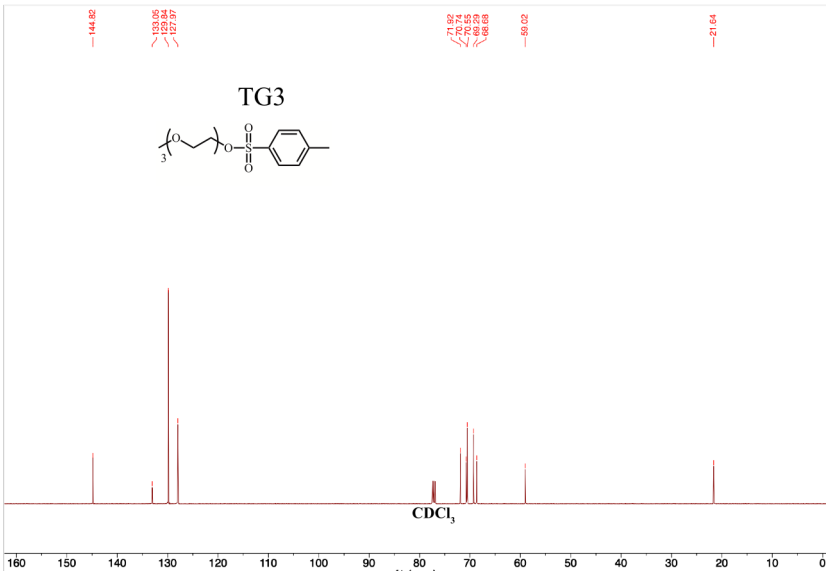

Figure 2.3 TG3 ^{13}C NMR

2.2.2 Reagent TG6

Synthesis of (1-(p-tosyl)-3,6,9,12,15,18- hexaoxononadecane) To a clean and dried 25 mL round bottom flask placed in an ice bath, a Teflon coated stir bar, NaOH (1.2 g, 30.0 mmol), DI H_2O (6.0 mL, 332.4 mmol), hexaethylene glycol monomethyl ether (*G6OH*, 3.00 g, 10.3 mmol), and THF (12.0 mL, 148.0 mmol) were added and allowed to react for 30 minutes. Next, PTSC (3.47 g, 18.2 mmol) was added under an atmosphere of N_2(g) and reacted for 12 hours. Upon completion, the reaction contents were dumped into 16 mL of cold DI H_2O, followed by extraction of the product with DCM (4 x 10 mL). The organic layer was washed with DI H_2O (2 x 10 mL), brine (1 x 10 mL), and subsequently dried over Na_2SO_4. The anhydrous organic layer was decanted away from the drying agent and concentrated under reduced pressure to provide the product TG6 as a colorless oil (99% yield, 4.56 g).[2] **Figure 2.4**: TG6 ^{1}H NMR (500 MHz, $CDCl_3$): δ 7.80-7.79 (d, 2H), 7.35-7.33 (d, 2H), 4.16 (t, 2H), 3.68 (t, 2H), 3.63 (m, 14H), 3.58 (s, 4H), 3.54 (t, 2H), 3.37 (s, 3H), 2.44 (s, 3H) **Figure 2.5**: TG6 ^{13}C NMR (500 MHz, $CDCl_3$): δ 144.9, 133.2, 130.0, 128.1, 72.1, 70.9, 70.8, 70.7, 70.7, 70.7, 70.7, 69.4, 68.8, 68.1, 59.2, 25.8, 21.8.

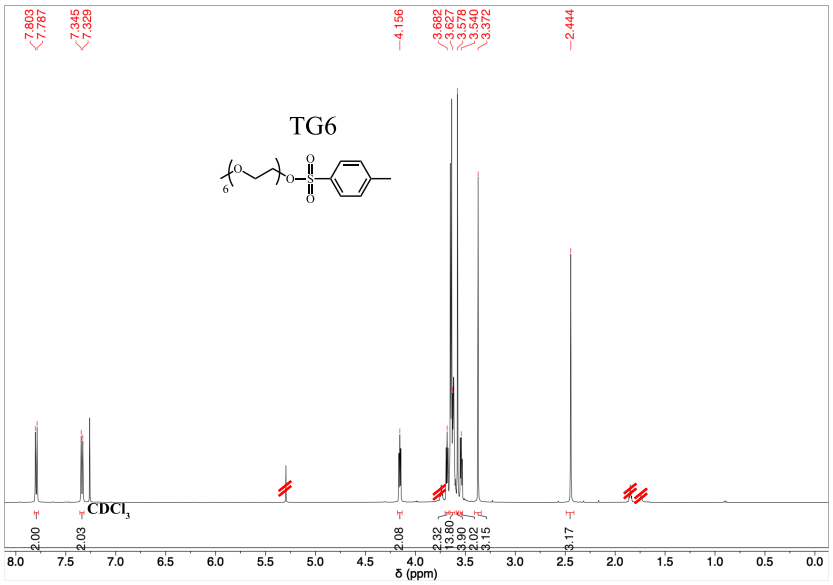

Figure 2.4 TG6 ^{1}H NMR with trace amount of *DCM, THF,* and water.

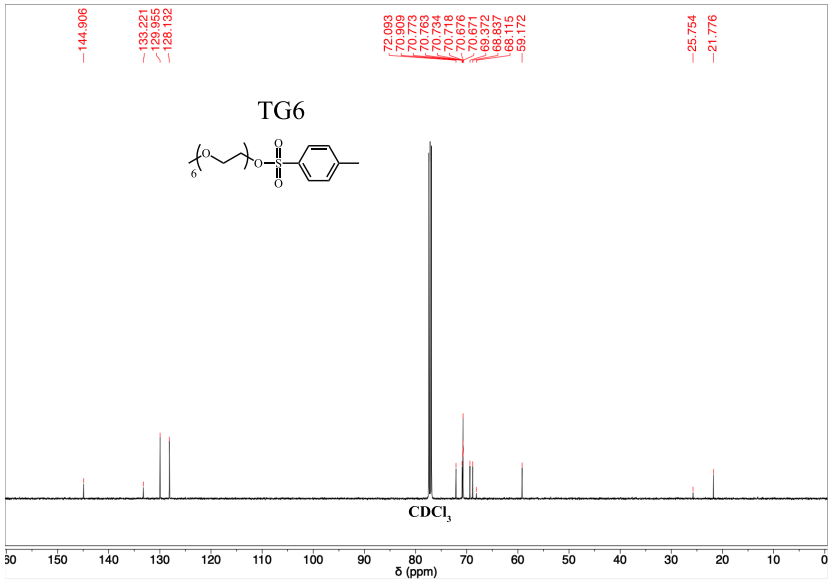

Figure 2.5 TG3 ^{13}C NMR

2.2.3 Reagent TG9

Synthesis of (1-(p-tosyl)-3,6,9,12,15,18,21,24,27- nonaoxooctacosane To a clean and dried 25 mL round bottom flask placed in an ice bath, a Teflon coated stir bar, NaOH (0.80 g, 20.0 mmol), DI H_2O (4.0 mL, 222 mmol), nonaethylene glycol monomethyl ether (*G9OH*, 3.00 g, 7.0 mmol), and THF (8.0 mL, 98.6 mmol) were added and allowed to react for 30 minutes. Next, PTSC (2.40 g, 12.6 mmol) was added under an atmosphere of N_2(g) and reacted for 12 hours. Upon completion, the reaction contents were dumped into 16 mL of cold DI H_2O, followed by extraction of the product with DCM (4 x 10 mL). The organic layer was washed with DI H_2O (2 x 10 mL), brine (1 x 10 mL), and subsequently dried over Na_2SO_4. The anhydrous organic layer was decanted away from the drying agent and concentrated under reduced pressure to provide the product TG9 as a colorless oil (99% yield, 4.06 g).[2] **Figure 2.6**: TG9 ^{1}H NMR (500 MHz, $CDCl_3$): δ 7.80-7.79 (d, 2H), 7.35-7.33 (d, 2H), 4.16 (t, 2H), 3.68 (t, 2H), 3.65- 3.64 (m, 22H), 3.61 (m, 4H), 3.58 (s, 4H), 3.54 (s, 2H), 3.37 (s, 3H), 2.44 (s, 3H) **Figure 2.7**: TG9 ^{13}C NMR (500 MHz, $CDCl_3$): δ 144.9, 133.2, 130.0, 128.1, 72.1, 70.9, 70.8, 70.7, 70.7, 69.4, 68.8, 68.1, 59.2, 25.8, 21.8.

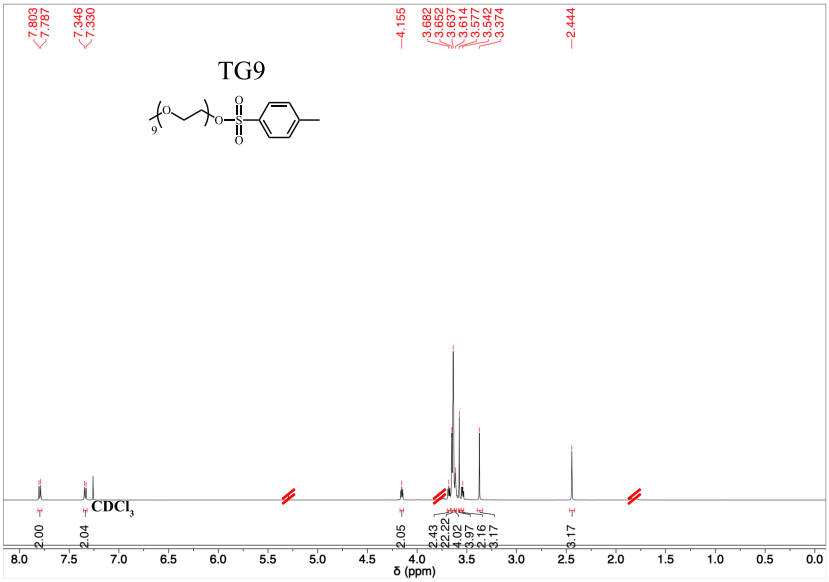

Figure 2.6 TG9 ^{1}H NMR with trace amount of *DCM, THF,* and water.

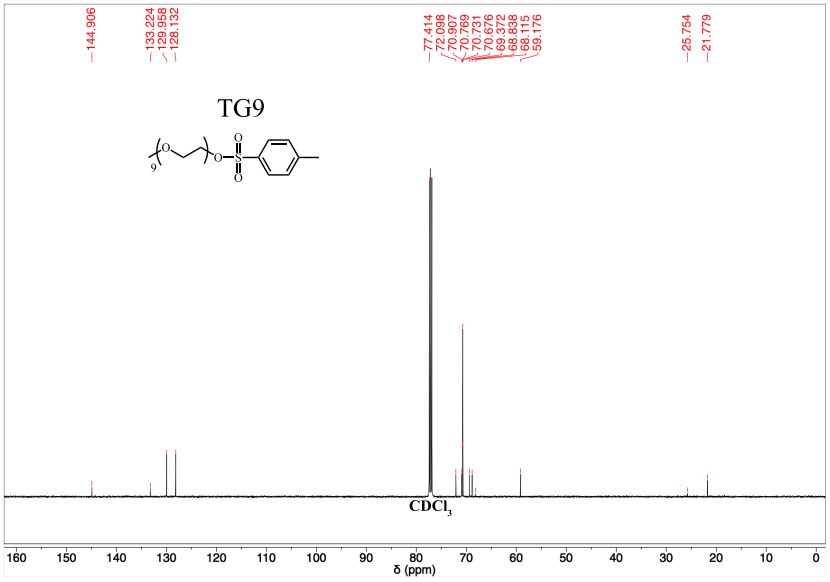

Figure 2.7 TG9 ^{13}C NMR

2.2.4 Reagent TG12

Synthesis of (1-(p-tosyl)-3,6,9,12,15,18,21,24,27,30,33,36- dodecaoxohepta-contane To a clean and dried 25 mL round bottom flask placed in an ice bath, a Teflon coated stir bar, NaOH (0.600 g, 15.0 mmol), DI H_2O (3.0 mL, 166.2 mmol), dodecaethylene glycol monomethyl ether (*G12OH*, 3.00 g, 5.35 mmol), and THF (6.0 mL, 74.0 mmol) were added and allowed to react for 30 minutes. Next, PTSC (1.84 g, 9.65 mmol) was added under an atmosphere of N_2(g) and reacted for 12 hours. Upon completion, the reaction contents were dumped into 16 mL of cold DI H_2O, followed by extraction of the product with DCM (4 x 10 mL). The organic layer was washed with DI H_2O (2 x 10 mL), brine (1 x 10 mL), and subsequently dried over Na_2SO_4. The anhydrous organic layer was decanted away from the drying agent and concentrated under reduced pressure to provide the product TG12 as a colorless oil (97% yield, 3.71 g).[2] **Figure 2.8**: TG12 ^{1}H NMR (500 MHz, $CDCl_3$): δ 7.75-7.73 (d, 2H), 7.30-7.29 (d, 2H), 4.10 (d, 2H), 3.63 (t, 2H), 3.59 (m, 34H), 3.57 (m, 4H), 3.53 (s, 4H), 3.49 (t, 2H), 3.32 (s, 3H), 2.40 (s, 3H) **Figure 2.9**: TG12 ^{13}C NMR (500 MHz, $CDCl_3$): δ 144.8, 133.1, 129.9, 128.0, 72.0, 70.8, 70.6, 70.5, 69.3, 68.7, 59.1, 21.7.

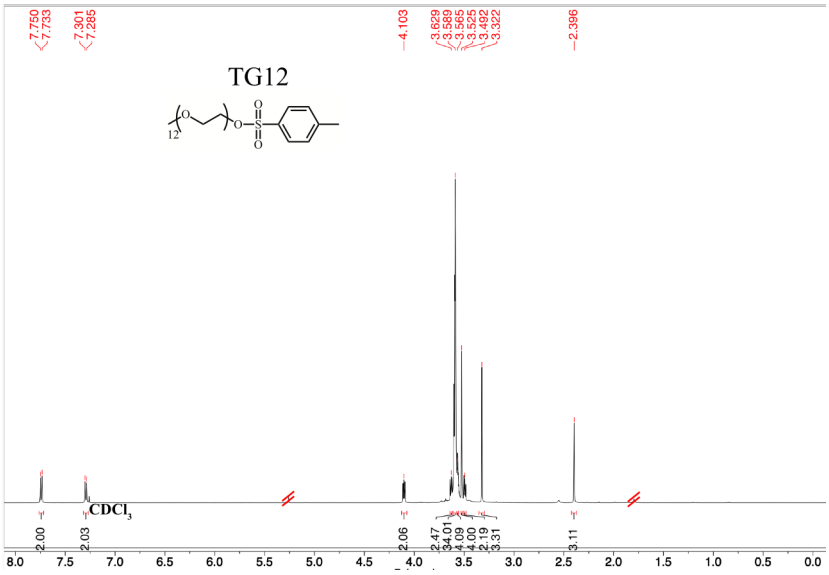

Figure 2.8 TG12 ^{1}H NMR with trace amount of *DCM, THF,* and water.

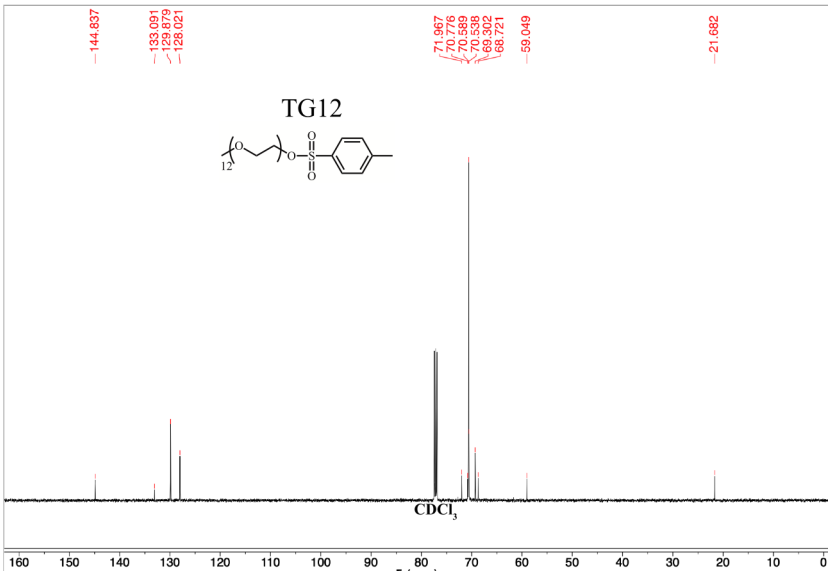

Figure 2.9 TG12 ^{13}C NMR

2.3 Synthesis of Monomers

2.3.1 Monomer FN

Synthesis of (2,7-dibromo-9,9-bis(3'-(N,N-dimethyl-amino)-propyl)-fluorene) To a clean, dried, 100 mL two neck round bottom flask, a Teflon coated stir bar, dimethyl sulfoxide (*DMSO*, 30.9 mL, 434.6 mmol), 2,7- dibromofluorene (*F*, 2 g, 6.2 mmol), tetrabutylammonium bromide (*TBAB*, 39.8 mg, 0.12 mmol), and 4 mL of a 50 wt. % aqueous sodium hydroxide solution (*50 wt. % aq. NaOH*, 4 mL, 154.3 mmol) was added under an atmosphere of N_2(g). An additional aliquot of DMSO (10.5 mL, 145.1 mmol) was added to the reaction flask, followed by dimethyl aminopropyl chloride hydrochloride salt (*DAPCl*, 2.6 g, 16.4 mmol). The reaction was stirred and heated at 60 °C for 12 hours. Reaction progress was monitored by thin-layer chromatography (*TLC*). DI H_2O (40 mL, 2.216 mmol) was added to the reaction flask to dissolve precipitated salts as well as to solvate DMSO. The product (FN) was extracted from the wet DMSO layer with diethyl ether (*Et_2O*, 8 x 25 mL), washed with a 10 wt. % aqueous NaOH (2 x 50 mL). The organic layer was washed with DI H_2O (3 x 50 mL), followed by a brine wash (1 x 50 mL), and then dried over Na_2SO4. Concentration of the anhydrous organic layer under reduced pressure lead to crude solid which was purified with a silica gel column (Hexanes: Ethyl Acetate: Triethylamine, 49:49:2) to obtain FN (59% yield, 1.81 g).[4,5] **Figure 2.10**: FN ^{1}H NMR (500 MHz, $CDCl_3$): δ 7.52-7.50 (d, 2H), 7.47 (s, 2H), 7.45-7.44 (d, 2H), 2.03 (s, 12H), 1.99 (m, 8H), 0.77 (m, 4H)

Figure 2.11: FN ^{13}C NMR (500 MHz, $CDCl_3$): δ 152.2, 139.3, 130.6, 126.3, 121.8, 121.4, 59.7, 55.5, 45.5, 37.7, 22.2.

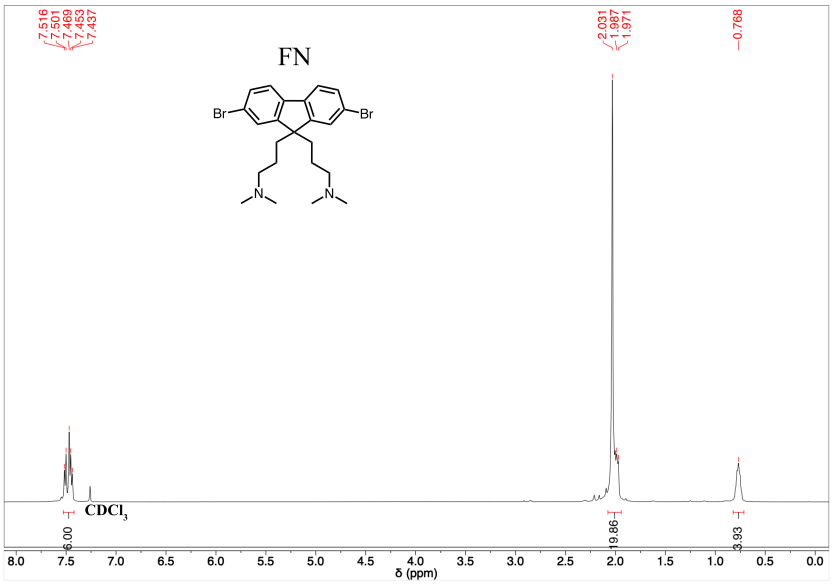

Figure 2.10 FN ^{1}H NMR

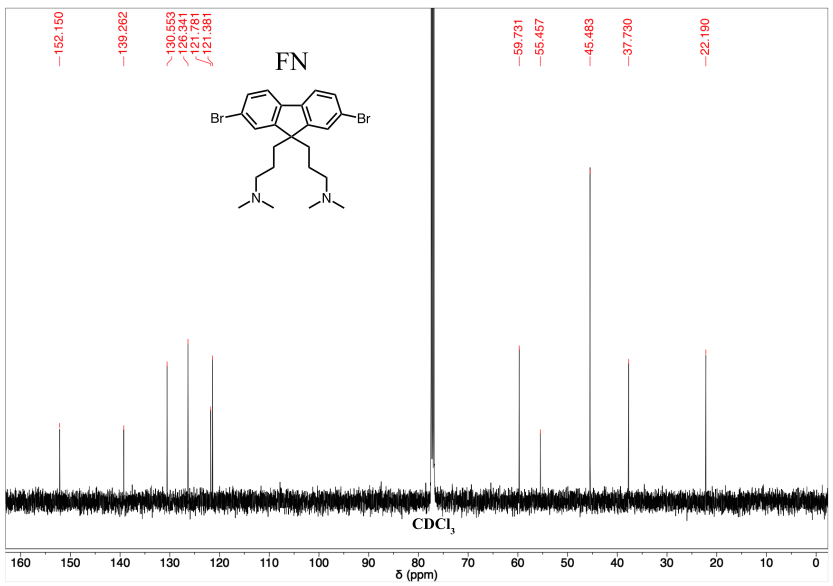

Figure 2.11 FN ^{13}C NMR

2.3.2 Monomer FNB

Synthesis of (2,7-diboryl pinacol ester-9,9-bis(3'-(N,N-dimethyl-amino)-propyl)-fluorene) To a clean, dried, 100 mL two neck round bottom flask, a Teflon coated stir bar, dimethylformamide (*DMF*, 39 mL, 505.8 mmol), FN (1 g, 2.0 mmol), bis(pinacolato)diboron (B_2Pin_2, 2.26 g, 8.9 mmol), potassium acetate (*KOAc*, 3.53 g, 17.8 mmol), [1,1'-Bis(diphenyl-phosphino)ferrocene]dichloro-palladium(II) ($Pd(dppf)Cl_2$, 0.296 g, 0.40 mmol) were added under an atmosphere of N_2(g). The contents of the reaction were stirred and heated at 80 °C for 24 hours. Reaction progress was monitored by TLC. Upon completion, the reaction was concentrated to dryness, and the crude solid was extracted with hot HPLC-grade hexanes (7 x 100 mL). The combined hexanes layer was filtered, concentrated to dryness, reextracted with hot hexanes, and re-concentrated to dryness. Acetone was used to extract the product from the re-dried hexanes layer and was allowed to crystallize out of the solution as an off-white solid. The crystals of FNB were collected via filtration and washed with a minimal amount of cold acetone to obtain FNB (55% yield, 0.6647 mg).[4,5] **Figure 2.12**: FNB ^{1}H NMR (500 MHz, $CDCl_3$): δ 7.80-7.78 (d, 2H), 7.78 (s, 2H), 7.71-7.70 (d, 2H), 2.06 (m, 4H), 1.99 (m, 4H), 1.98 (s, 12H), 1.37 (s, 24H), 0.75 (m, 4H) **Figure 2.13**: FNB ^{13}C NMR (500 MHz, $CDCl_3$): δ 149.4, 144.0, 134.3, 129.1, 119.8, 84.0, 59.2, 54.7, 44.6, 37.4, 31.1, 25.1.

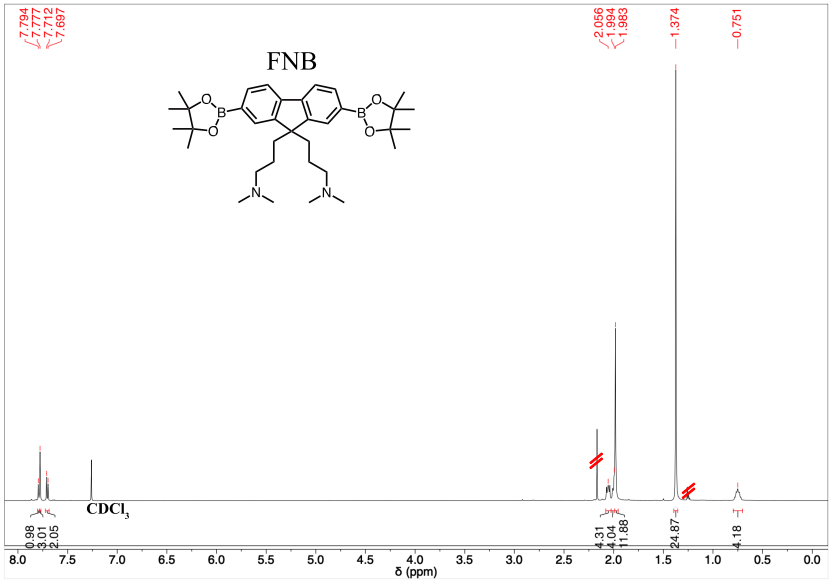

Figure 2.12 FNB ^{1}H NMR with trace amount of acetone and hexanes.

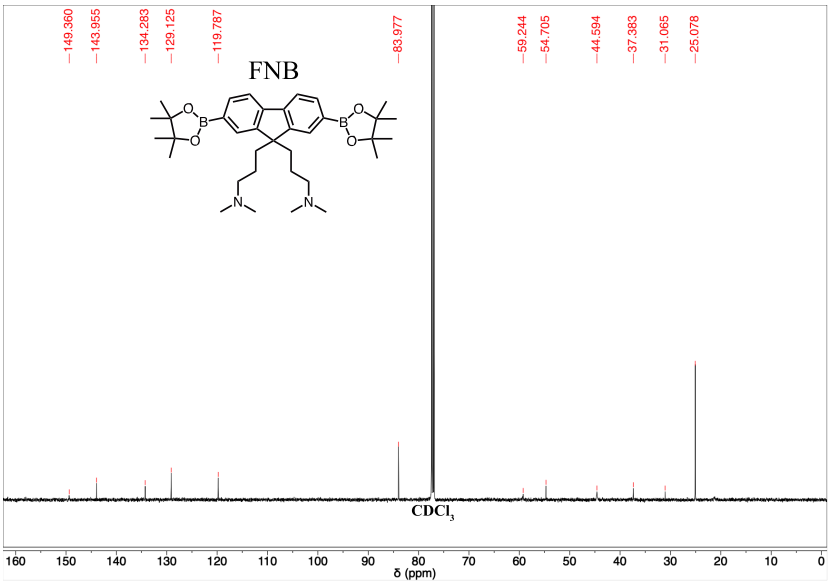

Figure 2.13 FNB ^{13}C NMR

2.3.3 Monomer FG3

Synthesis of (2,7-dibromo-9,9-bis-(2-(2-(2-methoxy-ethoxy) ethoxy) ethyl)-fluorene) To a clean and dried 25 mL round bottom flask, a Teflon coated stir bar, F (204.0 mg, 0.63 mmol), anhydrous DMF (3 mL, 38.7 mmol), and sodium hydride (*60% w/w dispersed in mineral oil NaH*, 80 mg, 2.0 mmol) were added under an inert atmosphere of N_2(g). After 30 minutes, the bright red solution was allowed to react at 60 °C for 12 hours with previously prepared TG3 (500 mg, 1.6 mmol). After quenching the remaining NaH with DI H_2O (2 mL), the reaction was extracted with DCM (4 x 20 mL). Dried the combined organic layer over Na_2SO_4. The anhydrous organic layer was decanted away from the drying agent. While stirring, a mixture consisting of 95% DCM with 5% Methanol (*MeOH*) was used to wash the product from the Na_2SO_4 slurry. The DCM: MeOH solution was decanted from the Na_2SO_4, and combined with the organic layer. The organic layer was concentrated under reduced pressure to provide a semi-crude solid which was purified further via a silica gel column (DCM: Ethyl Acetate, 80:20) to obtain FG3 (68.7% yield, 266.8 mg).[3] **Figure 2.14**: FG3 ^{1}H NMR (500 MHz, $CDCl_3$): δ 7.53 (d, 2H), 7.51-7.50 (d, 2H), 7.47-7.45 (d, 2H), 3.51 (m, 8H), 3.39 (t, 4H), 3.34 (s, 6H), 3.20 (t, 4H), 2.78 (t, 4H), 2.33 (t, 4H) **Figure 2.15**: FG3 ^{13}C NMR (500 MHz, $CDCl_3$): δ 151.1, 138.6, 130.8, 126.9, 121.8, 121.4, 72.0, 70.6, 70.6, 70.2, 66.9, 59.1, 52.1, 39.6.

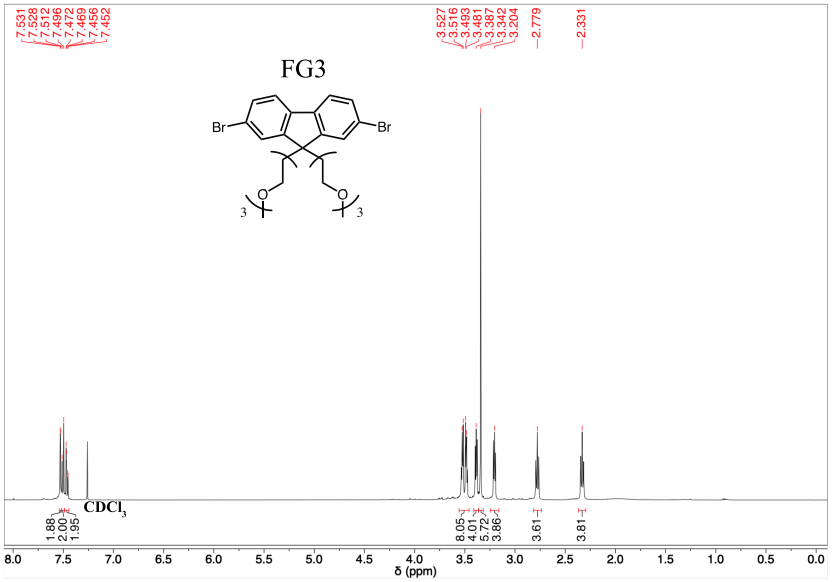

Figure 2.14 FG3 ^{1}H NMR

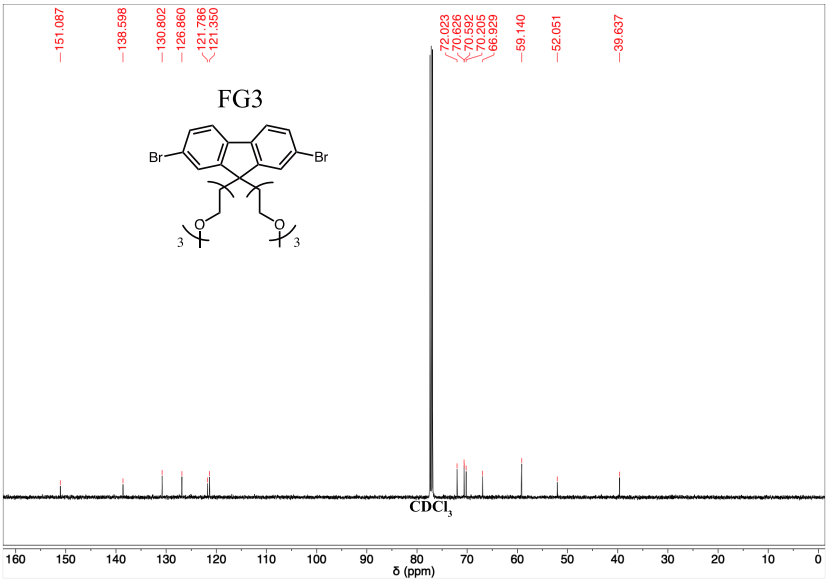

Figure 2.15 FG3 ^{13}C NMR

2.3.4 Monomer FG6

Synthesis of (2,7-dibromo-9,9-bis-(2-(2-(2-(2-(2-(2-methoxy-ethoxy) ethoxy) ethoxy) ethoxy) ethoxy) ethyl)- fluorene) To a clean and dried 50 mL round bottom flask, a Teflon coated stir bar, F (870 mg, 2.69 mmol), anhydrous DMF (15 mL, 193.7 mmol), and NaH in 60% w/w dispersed in mineral oil (400 mg, 10.0 mmol) were added under an inert atmosphere of N_2(g). After 30 minutes, the bright red solution was allowed to react at 60 °C for 12 hours with previously prepared TG6 (3.0 g, 6.7 mmol). After quenching the remaining NaH with DI H_2O (20 mL), the reaction was extracted with DCM (4 x 50 mL). Dried the combined organic layer over Na_2SO_4. The anhydrous organic layer was decanted away from the drying agent. While stirring, a mixture consisting of 95% DCM with 5% MeOH was used to wash the product from the Na_2SO_4 slurry. The DCM: MeOH solution was decanted from the Na_2SO_4, and combined with the organic layer. The organic layer was concentrated under reduced pressure to provide a semi-crude solid which was purified further via a silica gel column (Ethyl Acetate: MeOH, 99:1), followed by (Ethyl Acetate: MeOH, 90:10). Since the percentage of MeOH in the solvent used to elute the aggregated fraction of FG6 was 10%, FG6 was dissolved in chloroform (*$CHCl_3$*) to help precipitate out the once dissolved silica gel. The $CHCl_3$ solution was then filtered to remove the precipitate, and concentrated under reduced pressure to obtain FG6 (52.4% yield, 1.23 g).[3] **Figure 2.16**: FG6 ^{1}H NMR (500 MHz, $CDCl_3$): δ 7.53 (d, 2H), 7.52-7.50 (d, 2H), 7.47-7.46 (d, 2H), 3.64 (m, 12H), 3.61 (m, 8H), 3.58 (m, 4H), 3.54 (t, 8H), 3.38 (m, 4H), 3.37 (m, 6H), 3.19 (t, 4H), 2.77 (t, 4H), 2.33 (t, 4H) **Figure 2.17**: FG6 ^{13}C NMR (500 MHz,

$CDCl_3$): δ 151.0, 138.6, 130.8, 126.8, 121.7, 121.3, 72.0, 70.7, 70.6, 70.5, 70.2, 66.9, 59.1, 52.0, 39.6.

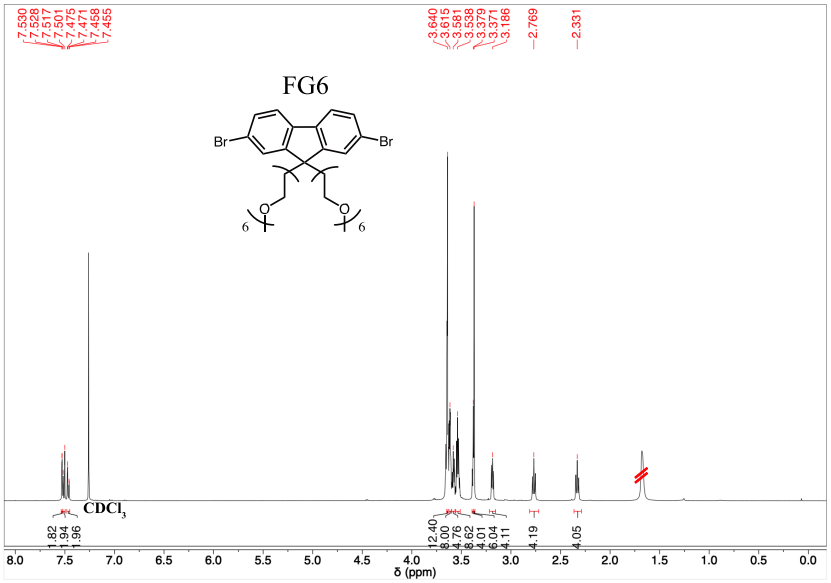

Figure 2.16 FG6 ^{1}H NMR with trace amount of water.

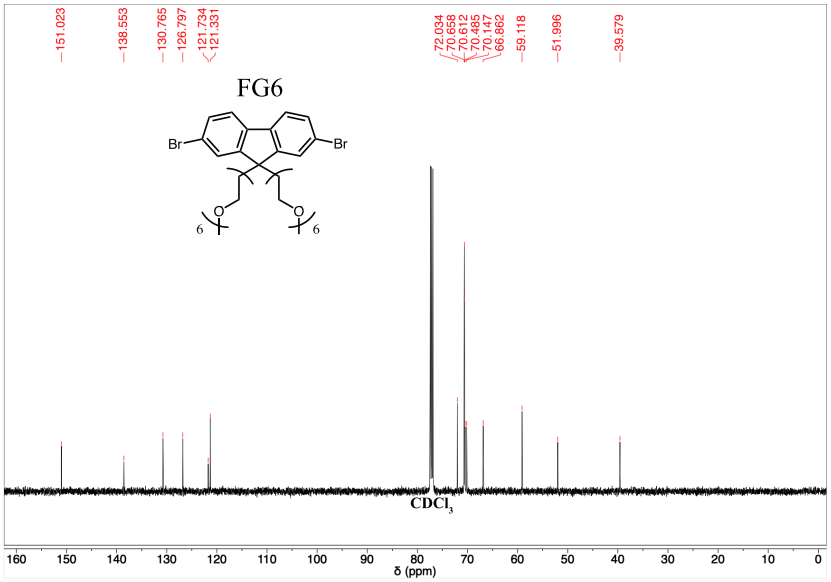

Figure 2.17 FG6 ^{13}C NMR

2.3.5 Monomer FG9

Synthesis of (2,7-dibromo-9,9-bis-(2-(2-(2-(2-(2-(2-(2-(2-methoxy-ethoxy) ethoxy) ethoxy) ethoxy) ethoxy) ethoxy) ethoxy) ethyl)- fluorene) To a clean and dried 50 mL round bottom flask, a Teflon coated stir bar, F (670 mg, 2.1 mmol), anhydrous DMF (12 mL, 155 mmol), and NaH in 60% w/w dispersed in mineral oil (210 mg, 5.3 mmol) were added under an inert atmosphere of N_2(g). After 30 minutes, the bright red solution was allowed to react at 60 °C for 12 hours with previously prepared TG9 (3.0 g, 5.2 mmol). After quenching the remaining NaH with DI H_2O (15 mL), the reaction was extracted with DCM (4 x 50 mL). Dried the combined organic layer over Na_2SO_4. The anhydrous organic layer was decanted away from the drying agent. While stirring, a mixture consisting of 95% DCM with 5% MeOH was used to wash the product from the Na_2SO_4 slurry. The DCM: MeOH solution was decanted from the Na_2SO_4, and combined with the organic layer. The organic layer was concentrated under reduced pressure to provide a semi-crude solid which was purified further via a silica gel column (Ethyl Acetate: MeOH, 90:10). Since the percentage of MeOH in the solvent used to elute the aggregated fraction of FG9 was 10%, FG9 was dissolved in $CHCl_3$ to help precipitate out the once dissolved silica gel. The $CHCl_3$ solution was then filtered to remove the precipitate, and concentrated under reduced pressure to obtain FG9 (30.0% yield, 0.710 g).[3] **Figure 2.18**: FG9 ^{1}H NMR (500 MHz, $CDCl_3$): δ 7.53 (d, 2H), 7.52-7.50 (d, 2H), 7.47-7.46 (d, 2H), 3.64 (m, 44H), 3.58 (m, 4H), 3.54 (t, 8H), 3.37 (m, 10H), 3.18 (t, 4H), 2.77 (t, 4H), 2.33 (t, 4H) **Figure 2.19**:

FG9 ^{13}C NMR (500 MHz, $CDCl_3$): δ 151.0, 138.6, 130.8, 126.8, 121.7, 121.4, 72.0, 70.7, 70.7, 70.6, 70.6, 70.5, 70.1, 66.9, 60.5, 59.1, 52.0, 39.6.

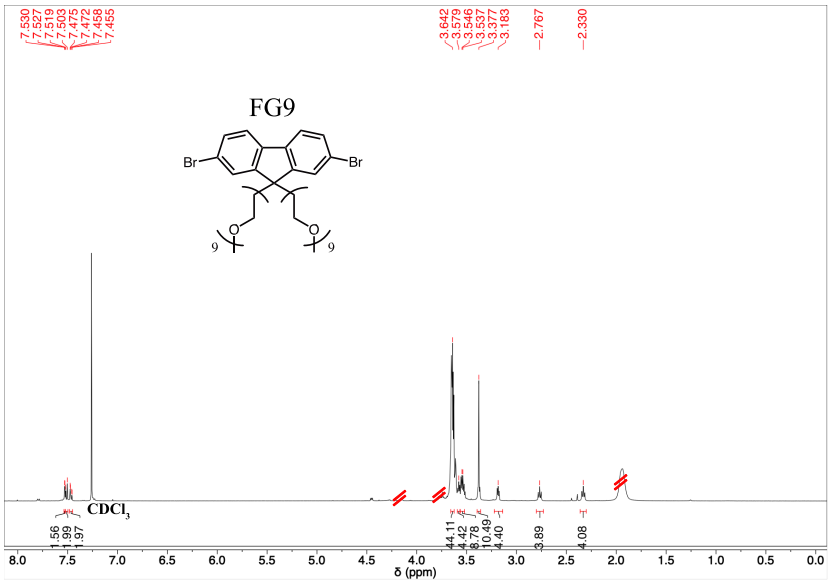

Figure 2.18 FG9 ^{1}H NMR with trace amount of THF and EtOAc.

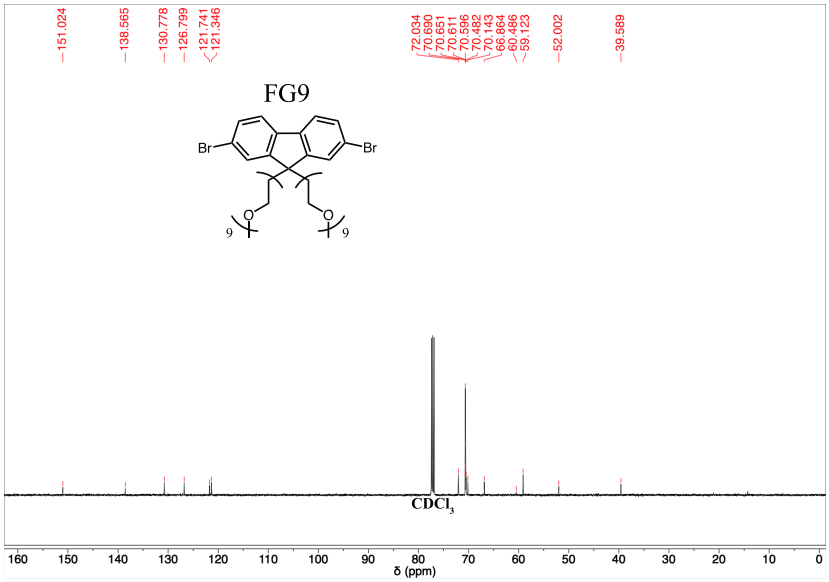

Figure 2.19 FG9 ^{13}C NMR

2.3.6 Monomer FG12

Synthesis of (2,7-dibromo-9,9-bis-(2-(2-(2-(2-(2-(2-(2-(2-(2-(2-(2-methoxy -ethoxy) ethoxy) ethoxy) ethoxy) ethoxy) ethoxy) ethoxy) ethoxy) ethoxy) ethoxy) ethyl)- fluorene) To a clean and dried 50 mL round bottom flask, a Teflon coated stir bar, F (550 mg, 1.7 mmol), anhydrous DMF (10 mL, 136 mmol), and NaH in 60% w/w dispersed in mineral oil (200 mg, 5.0 mmol) were added under an inert atmosphere of N_2(g). After 30 minutes, the bright red solution was allowed to react at 60 °C for 12 hours with previously prepared TG12 (3.0 g, 4.2 mmol). After quenching the remaining NaH with DI H_2O (15 mL), the reaction was extracted with DCM (4 x 50 mL). Dried the combined organic layer over Na_2SO_4. The anhydrous organic layer was decanted away from the drying agent. While stirring, a mixture consisting of 95% DCM with 5% MeOH was used to wash the product from the Na_2SO_4 slurry. The DCM: MeOH solution was decanted from the Na_2SO_4, and combined with the organic layer. The organic layer was concentrated under reduced pressure to provide a semi-crude solid which was purified further via a silica gel column (Ethyl Acetate: MeOH, 85:15), followed by (Ethyl Acetate: MeOH, 50:50). Since the percentage of MeOH in the solvent used to elute the aggregated fraction of FG12 was 15-50%, FG12 was dissolved in $CHCl_3$ to help precipitate out the once dissolved silica gel. The $CHCl_3$ solution was then filtered to remove the precipitate, and concentrated under reduced pressure to obtain FG12 (76.1% yield, 1.80 g).[3] **Figure 2.20**: FG12 ^{1}H NMR (500 MHz, $CDCl_3$): δ 7.53 (d, 2H), 7.52-7.50 (d, 2H), 7.47-7.46 (d, 2H), 3.64 (m, 68H), 3.58 (m, 4H), 3.55 (t, 8H), 3.38 (m, 10H), 3.18 (t, 4H), 2.77 (t, 4H), 2.33 (t, 4H) **Figure 2.21**:

FG12 ^{13}C NMR (500 MHz, $CDCl_3$): δ 150.9, 138.4, 130.7, 126.7, 121.6, 121.2, 71.9, 70.6, 70.5, 70.5, 70.4, 70.0, 66.8, 59.0, 51.9, 39.5.

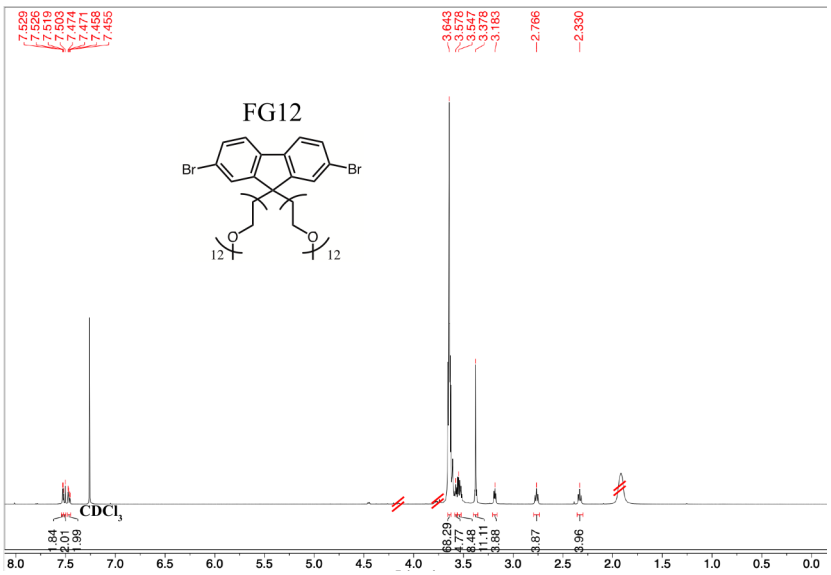

Figure 2.20 FG12 ^{1}H NMR

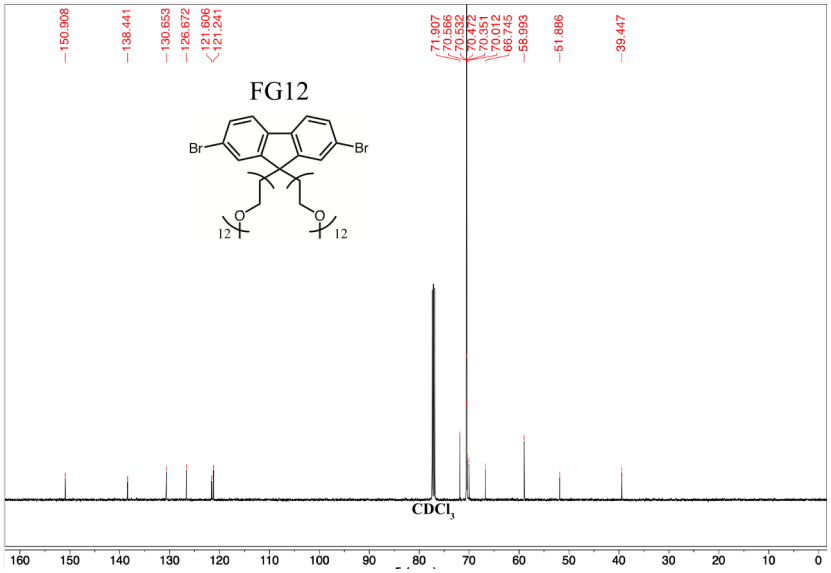

Figure 2.21 FG12 ^{13}C NMR

2.4 Synthesis of Neutral Polymers

2.4.1 Polymer nPFNG3- Batch 1

Polymerization of poly([9,9-bis(3'-(N,N-dimethyl-amino)-propyl)-fluorene]-alt-co-[9,9-bis-(2-(2-(2-methoxy-ethoxy) ethoxy) ethyl)- fluorene] To a clean and dried 15 mL pressure tube, a Teflon coated stir bar, FG3 (500 mg, 0.81 mmol), FNB (480 mg, 0.82 mmol), potassium carbonate (K_2CO_3, 1.35 g, 9.8 mmol), 1,4- dioxane (*Dioxane*, 7 mL, 90.4 mmol), DI H_2O (5.0 mL, 277.0 mmol), and Pd(dppf)Cl_2 (6 mg, 0.008 mmol) were added. The reaction solution as well as the head space was flushed with N_2(g). The pressure vial was capped quickly, placed into a silicon oil bath, stirred, and heated at 100 °C for 48 hours. To stop the reaction, the stirring function was turned off, the bottom water layer was removed, and an aliquot of nPFNG3 dispersed in dioxane was removed for further characterization. The polymer in dioxane (1 mL) was pipetted into DI H_2O (10 mL) to induce precipitation of nPFNG3. The water was decanted from the polymer and nPFNG3 was dried via vacuum filtration.[1,6] **Figure 2.22**: nPFNG3- Batch 1 ^{1}H NMR (800 MHz, $CDCl_3$): δ 7.82-7.70 (br, 1.00 H), 3.70 (br, 1.11 H), 3.64 (br, 0.12 H), 3.52 (br, 0.35 H), 3.45 (br, 0.85 H), 3.13 (br, 0.91 H), 2.93 (br, 0.26 H), 2.79 (br, 0.04 H), 2.57 (br, 0.19 H), 2.47 (br, 0.09 H), 2.42 (br, 0.14 H), 2.18 (br, 0.12 H), 2.11 (br, 0.32 H), 2.06 (br, 0.98 H), 0.97- 0.89 (br, 0.30 H) **Figure 2.23**: nPFNG3-Batch 1 ^{13}C NMR (800 MHz, $CDCl_3$): δ 151.5, 150.0, 141.0, 140.5, 139.6, 131.6,

129.1, 128.4, 126.9, 126.6, 121.7, 121.5, 120.4, 72.0, 70.7, 70.6, 69.8, 68.7, 67.2, 66.5, 66.3, 62.8, 62.4, 59.9, 59.1, 55.3, 51.6, 45.5, 40.1, 38.1, 29.8, 22.3.

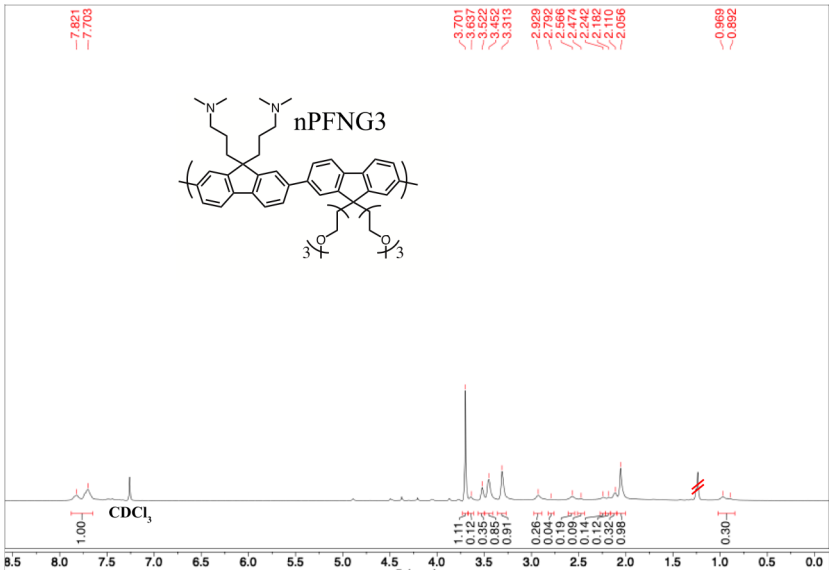

Figure 2.22 nPFNG3- Batch 1 ^{1}H NMR

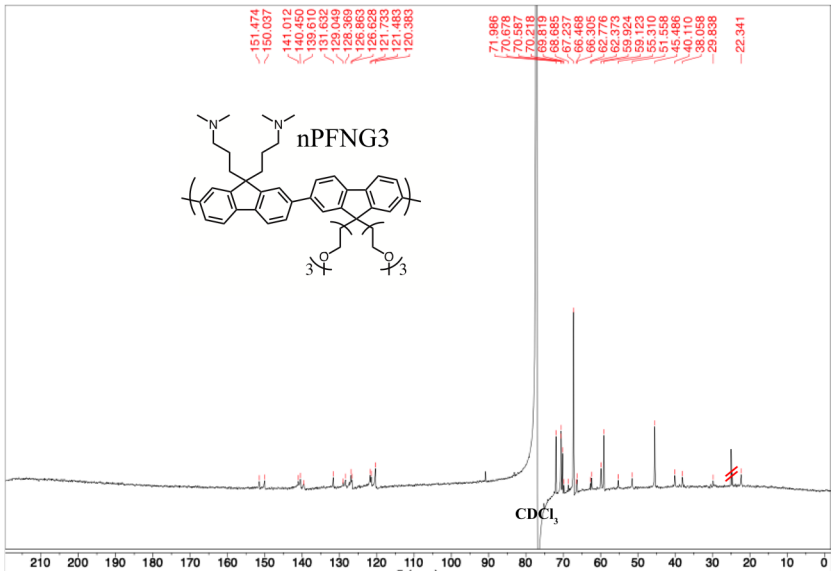

Figure 2.23 nPFNG3- Batch 1 ^{13}C NMR

2.4.2 Polymer nPFNG6- Batch 1

Polymerization of nPFNG6: poly([9,9-bis(3'-(N,N-dimethyl-amino)-propyl)-fluorene]-alt-co-[9,9-bis-(2-(2-(2-(2-(2-(2-methoxy-ethoxy) ethoxy) ethoxy) ethoxy) ethoxy) ethyl)- fluorene] nPFNG6 Batch 1: To a clean and dried 15 mL pressure tube, a Teflon coated stir bar, FG6 (500 mg, 0.57 mmol), FNB (344.08 mg, 0.58 mmol), K_2CO_3 (0.950 g, 6.9 mmol), Dioxane (5 mL, 64.6 mmol), DI H_2O (3.4 mL, 221.6 mmol), and $Pd(dppf)Cl_2$ (4 mg, 0.005 mmol) were added. The reaction solution as well as the head space was flushed with N_2(g). The pressure vial was capped quickly, placed into a silicon oil bath, stirred, and heated at 100 °C for 48 hours. To stop the reaction, the stirring function was turned off, the bottom water layer was removed, and an aliquot of nPFNG6 dispersed in Dioxane was removed for further characterization. The polymer in Dioxane (1 mL) was pipetted into DI H_2O (10 mL) to induce precipitation of nPFNG6. The water was decanted from the polymer and nPFNG6 was dried via vacuum filtration.[1,6] **Figure 2.24**: nPFNG6- Batch 1 ^{1}H NMR (800 MHz, $CDCl_3$): δ 7.83-7.71 (br, 1.00 H), 3.62 (br, 2.28 H), 3.52 (br, 1.15 H), 3.44 (br, 0.51 H), 3.35 (br, 0.65 H), 3.28 (br, 0.40 H), 2.91 (br, 0.34 H), 2.56 (br, 0.33 H), 2.18 (br, 0.82 H), 2.10 (br, 0.93 H), 1.00- 0.87 (br, 0.31 H), **Figure 2.25**: nPFNG6- Batch 1 ^{13}C NMR (800 MHz, $CDCl_3$): δ 151.2, 150.0, 140.9, 140.5, 140.3, 139.5, 126.9, 126.7, 121.78, 121.5, 120.4, 72.1, 70.6, 70.2, 67.3, 67.2, 66.3, 62.4, 59.7, 59.2, 55.2, 54.5, 51.5, 45.2, 44.5, 40.1, 37.9, 22.0, 21.1.

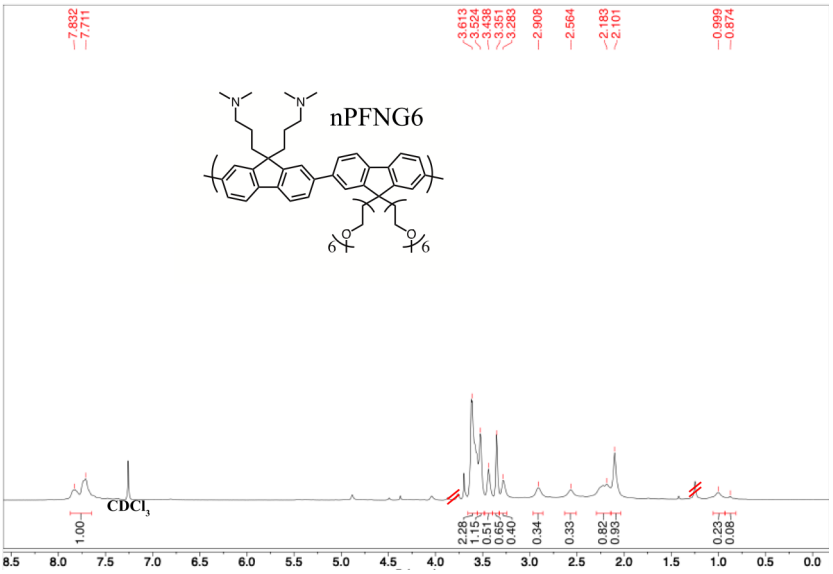

Figure 2.24 nPFNG6- Batch 1 ^{1}H NMR

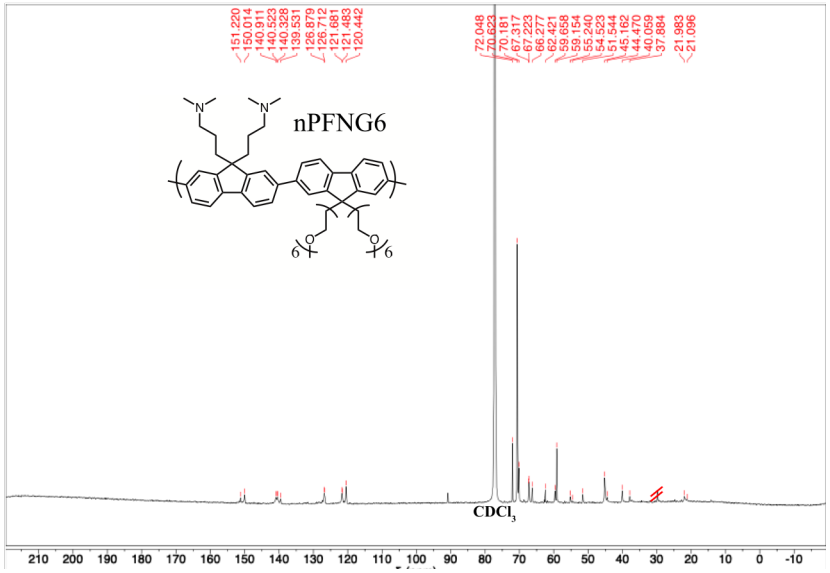

Figure 2.25 nPFNG6- Batch 1 ^{13}C NMR

2.4.3 Polymer nPFNG9- Batch 1

Polymerization of poly([9,9-bis(3'-(N,N-dimethyl-amino)-propyl)-fluorene]-alt-co-[9,9-bis-(2-(2-(2-(2-(2-(2-(2-(2-methoxy-ethoxy) ethoxy) ethoxy) ethoxy) ethoxy) ethoxy) ethoxy) ethoxy) ethyl)- fluorene] nPFNG9 Batch 1: To a clean and dried 15 mL pressure tube, a Teflon coated stir bar, FG9 (500 mg, 0.44 mmol), FNB (260 mg, 0.44 mmol), K_2CO_3 (0.780 g, 5.6 mmol), Dioxane (4 mL, 54.4 mmol), DI H_2O (3.0 mL, 166.2 mmol), and $Pd(dppf)Cl_2$ (3.0 mg, 0.004 mmol) were added. The reaction solution as well as the head space was flushed with N_2(g). The pressure vial was capped quickly, placed into a silicon oil bath, stirred, and heated at 100 °C for 48 hours. To stop the reaction, the stirring function was turned off, the bottom water layer was removed, and an aliquot of nPFNG9 dispersed in Dioxane was removed for further characterization. The polymer in Dioxane (1 mL) was pipetted into DI H_2O (10 mL) to induce precipitation of nPFNG9. The water was decanted from the polymer and nPFNG6 was dried via vacuum filtration.[1,6] **Figure 2.26**: nPFNG9- Batch 1 ^{1}H NMR (800 MHz, $CDCl_3$): δ 7.81-7.69 (br, 1.00 H), 3.68 (br, 3.27 H), 3.61 (br, 4.43 H), 3.52 (br, 1.90 H), 3.43 (br, 0.62 H), 3.35 (br, 0.83 H), 3.27 (br, 0.49 H), 2.90 (br, 0.33 H), 2.54 (br, 0.30 H), 2.09 (br, 0.47 H), 2.04 (br, 1.08 H), 0.95- 0.86 (br, 0.23 H) **Figure 2.27**: nPFNG9- Batch 1 ^{13}C NMR (800 MHz, $CDCl_3$): δ 151.4, 150.0, 140.9, 140.4, 139.4, 131.6, 128.9, 128.3, 126.8, 126.6, 121.6, 121.4, 120.3, 72.0, 70.6, 70.1, 67.2, 62.6, 59.9, 59.1, 55.2, 51.5, 45.5, 40.0, 38.0, 29.8.

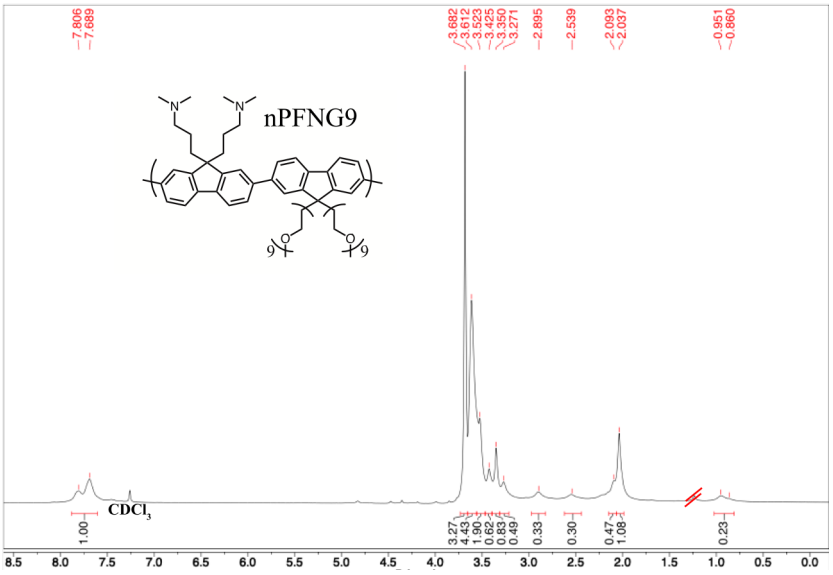

Figure 2.26 nPFNG9- Batch 1 ^{1}H NMR

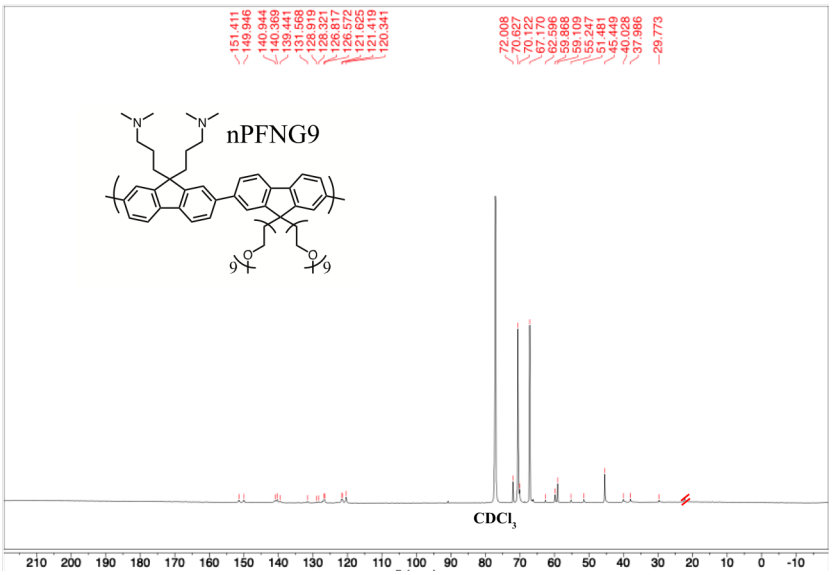

Figure 2.27 nPFNG9- Batch 1 ^{13}C NMR

2.4.4 Polymer nPFNG3- Batch 2

Polymerization poly([9,9-bis(3'-(N,N-dimethyl-amino)-propyl)-fluorene]-alt-co-[9,9-bis-(2-(2-(2-methoxy-ethoxy) ethoxy) ethyl)- fluorene] of nPFNG3 Batch 2: To a clean and dried 48 mL pressure tube, a Teflon coated stir bar, FG3 (620 mg, 1.01 mmol), FNB (580 mg, 0.99 mmol), K_2CO_3 (1.68 g, 12.2 mmol), Dioxane (10.0 mL, 136.0 mmol), DI H_2O (6.0 mL, 332.4 mmol), and $Pd(dppf)Cl_2$ (10 mg, 0.01 mmol) were added. The reaction solution as well as the head space was flushed with $N_2(g)$. The pressure vial was capped quickly, placed into a silicon oil bath, stirred, and heated at 100 °C for 24 hours. To stop the reaction, the stirring function was turned off, the bottom water layer was removed, and an aliquot of nPFNG3 dispersed in Dioxane was removed for further characterization. The polymer in Dioxane (1 mL) was pipetted into DI H_2O (10 mL) to induce precipitation of nPFNG3. The water was decanted from the polymer and nPFNG3 was dried via vacuum filtration.[1,6] **Figure 2.28**: nPFNG3- Batch 2 ^1H NMR (800 MHz, $CDCl_3$): δ 7.82-7.70 (br, 1.00 H), 3.52 (br, 0.40 H), 3.45 (br, 0.88 H), 3.31 (br, 1.09 H), 2.93 (br, 0.27 H), 2.80 (br, 0.09 H), 2.56 (br, 0.19 H), 2.48 (br, 0.12 H), 2.24 (br, 0.24 H), 2.11 (br, 0.37 H), 2.05 (br, 1.34 H), 0.96 (br, 0.29 H) **Figure 2.29**: nPFNG3- Batch 2 ^{13}C NMR (800 MHz, $CDCl_3$): δ 151.5, 150.0, 141.0, 140.5, 139.5, 126.8, 126.6, 121.7, 121.5, 72.0, 70.7, 70.6, 70.2, 67.3, 59.9, 59.1, 55.3, 51.5, 45.5, 40.1, 38.1, 22.4.

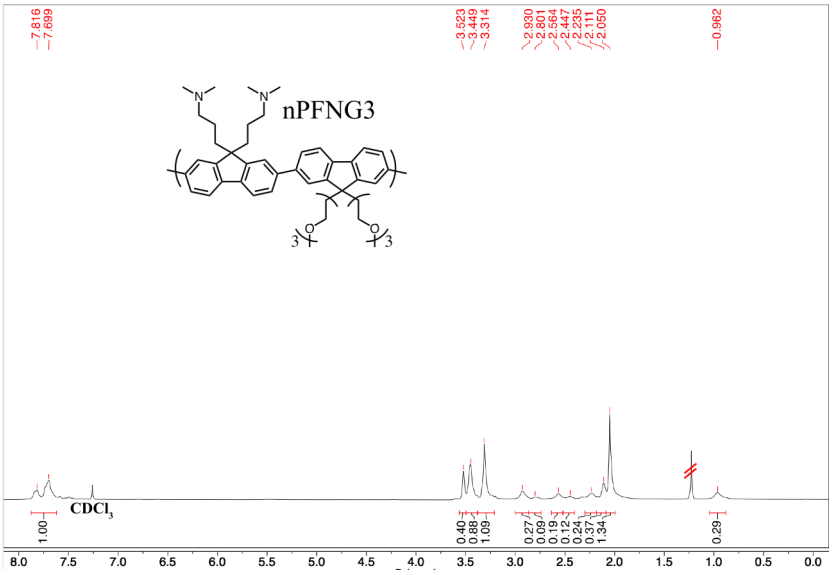

Figure 2.28 nPFNG3- Batch 2 ^{1}H NMR with trace amount of pinacol.

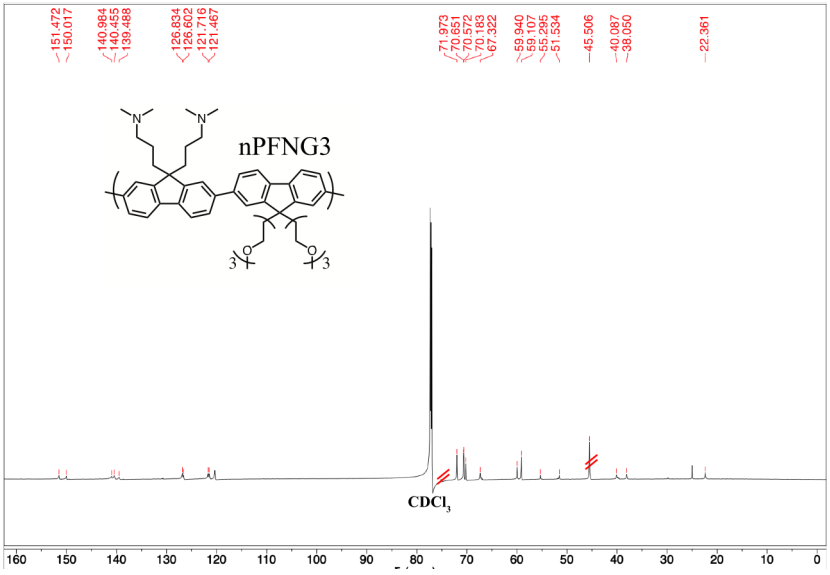

Figure 2.29 nPFNG3- Batch 2 ^{13}C NMR

2.4.5 Polymer nPFNG6- Batch 2

Polymerization of poly([9,9-bis(3'-(N,N-dimethyl-amino)-propyl)-fluorene]-alt-co-[9,9-bis-(2-(2-(2-(2-(2-(2-methoxy-ethoxy) ethoxy) ethoxy) ethoxy) ethoxy) ethyl)-fluorene] To a clean and dried 48 mL pressure tube, a Teflon coated stir bar, FG6 (880 mg, 1.00 mmol), FNB (580 mg, 0.99 mmol), K_2CO_3 (1.73 g, 12.5 mmol), Dioxane (10.0 mL, 136.0 mmol), DI H_2O (6.0 mL, 332.4 mmol), and $Pd(dppf)Cl_2$ (10 mg, 0.01 mmol) were added. The reaction solution as well as the head space was flushed with N_2(g). The pressure vial was capped quickly, placed into a silicon oil bath, stirred, and heated at 100 °C for 24 hours. To stop the reaction, the stirring function was turned off, the bottom water layer was removed, and an aliquot of nPFNG6 dispersed in Dioxane was removed for further characterization. The polymer in Dioxane (1 mL) was pipetted into DI H_2O (10 mL) to induce precipitation of nPFNG6. The water was decanted from the polymer and nPFNG6 was dried via vacuum filtration.[1,6] **Figure 2.30**: nPFNG6-Batch 2 ^{1}H NMR (800 MHz, $CDCl_3$): δ 7.80-7.70 (br, 1.00 H), 3.62 (br, 2.06 H), 3.52 (br, 1.42 H), 3.44 (br, 0.44 H), 3.35 (br, 0.66 H), 3.28 (br, 0.35 H), 2.91 (br, 0.29 H), 2.56 (br, 0.22 H), 2.23 (br, 0.34 H), 2.11 (br, 0.37 H), 2.05 (br, 1.45 H), 0.96- 0.88 (br, 0.34 H) **Figure 2.31**: nPFNG6- Batch 2 ^{13}C NMR (800 MHz, $CDCl_3$): δ 151.5, 150.0, 141.0, 140.4, 139.7, 126.9, 121.7, 121.5, 120.4, 72.1, 70.6, 70.2, 67.3, 67.2, 60.0, 51.5, 45.5, 45.4, 40.1, 38.2, 38.1, 29.8, 22.4.

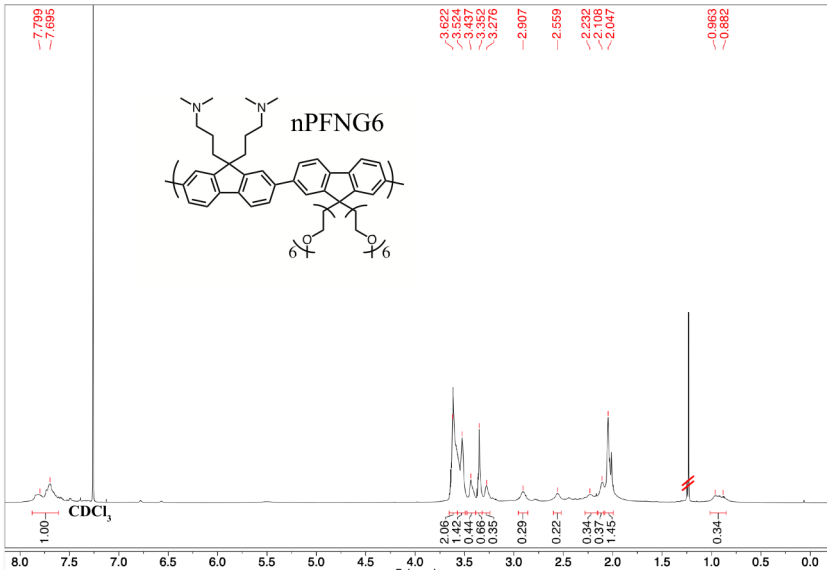

Figure 2.30 nPFNG6- Batch 2 ^{1}H NMR with trace amount of pinacol.

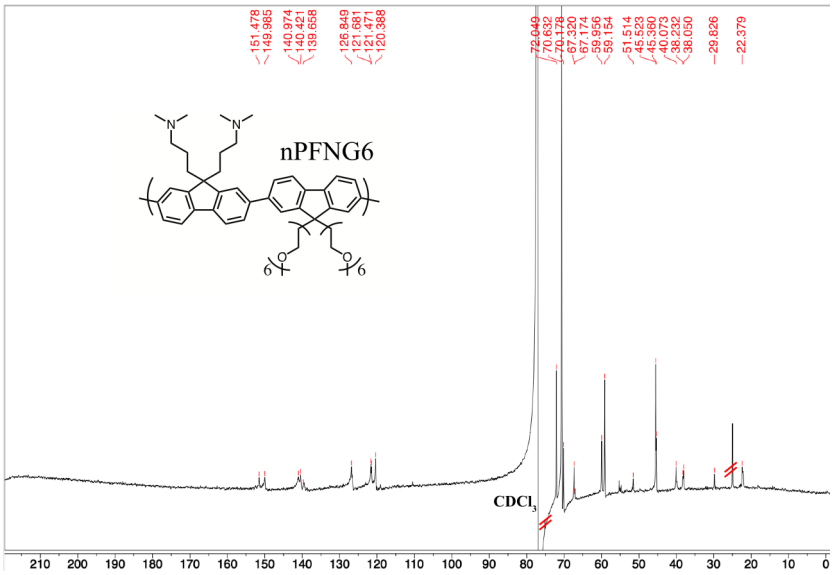

Figure 2.31 nPFNG6- Batch 2 ^{13}C NMR

2.4.6 Polymer nPFNG9- Batch 2

Polymerization of poly([9,9-bis(3'-(N,N-dimethyl-amino)-propyl)-fluorene]-alt-co-[9,9-bis-(2-(2-(2-(2-(2-(2-(2-(2-methoxy-ethoxy) ethoxy) ethoxy) ethoxy) ethoxy) ethoxy) ethoxy) ethoxy) ethyl)- fluorene] To a clean and dried 48 mL pressure tube, a Teflon coated stir bar, FG9 (1140 mg, 1.00 mmol), FNB (580 mg, 0.99 mmol), K_2CO_3 (1.73 g, 12.5 mmol), Dioxane (10.0 mL, 136.0 mmol), DI H_2O (6.0 mL, 332.4 mmol), and $Pd(dppf)Cl_2$ (10 mg, 0.01 mmol) were added. The reaction solution as well as the head space was flushed with N_2(g). The pressure vial was capped quickly, placed into a silicon oil bath, stirred, and heated at 100 °C for 24 hours. To stop the reaction, the stirring function was turned off, the bottom water layer was removed, and an aliquot of nPFNG9 dispersed in Dioxane was removed for further characterization. The polymer in Dioxane (1 mL) was pipetted into DI H_2O (10 mL) to induce precipitation of nPFNG9. The water was decanted from the polymer and nPFNG9 was dried via vacuum filtration.[1,6] **Figure 2.32**: nPFNG9- Batch 2 ^{1}H NMR (800 MHz, $CDCl_3$): δ 7.78-7.69 (br, 1.00 H), 3.62 (br, 3.72 H), 3.53 (br, 1.51 H), 3.42 (br, 0.35 H), 3.36 (br, 0.64 H), 3.26 (br, 0.43 H), 2.89 (br, 0.30 H), 2.56 (br, 0.32 H), 2.01 (br, 1.56 H), 0.96-0.88 (br, 0.36 H) **Figure 2.33**: nPFNG9- Batch 2 ^{13}C NMR (800 MHz, $CDCl_3$): δ 207.1, 140.8, 127.4, 120.5, 72.1, 70.7, 70.2, 67.2, 60.1, 59.2, 45.5, 38.0, 31.1, 29.8, 22.3.

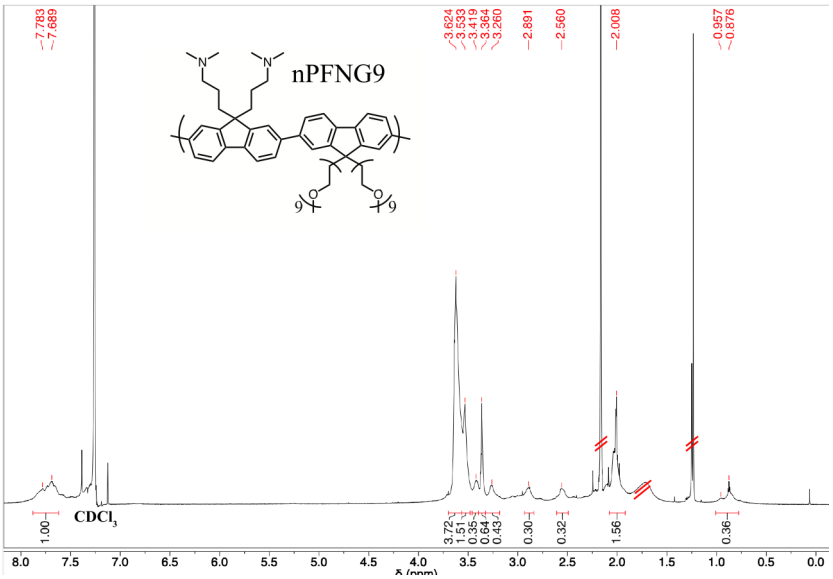

Figure 2.32 nPFNG9- Batch 2 ^{1}H NMR with trace amount of acetone, water, and pinacol.

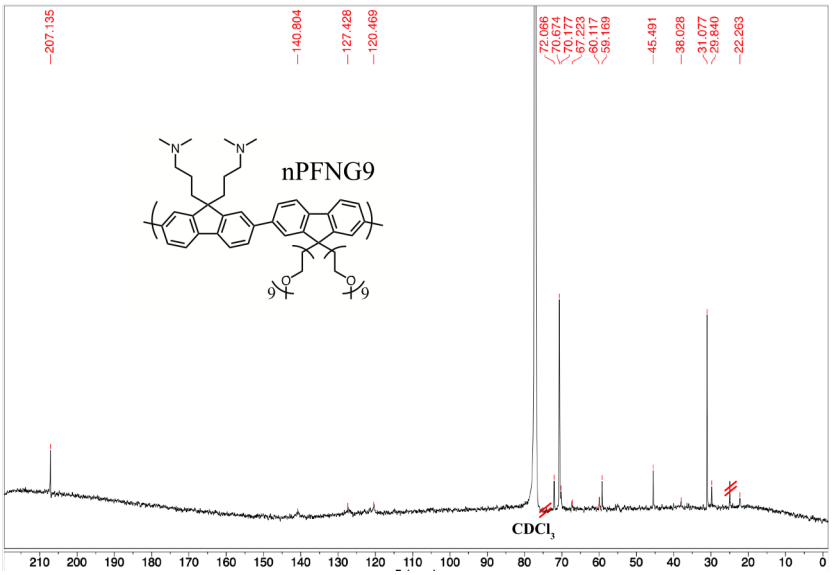

Figure 2.33 nPFNG9- Batch 2 ^{13}C NMR

2.4.7 Polymer nPFNG12- Batch 2

Polymerization of poly([9,9-bis(3'-(N,N-dimethyl-amino)-propyl)-fluorene]-alt-co-[9,9-bis-(2-(2-(2-(2-(2-(2-(2-(2-(2-(2-(2-methoxy-ethoxy) ethoxy) ethoxy) ethoxy) ethoxy) ethoxy) ethoxy) ethoxy) ethoxy) ethoxy) ethyl)- fluorene] To a clean and dried 48 mL pressure tube, a Teflon coated stir bar, FG12 (1430 mg, 1.02 mmol), FNB (580 mg, 0.99 mmol), K_2CO_3 (1.68 g, 12.2 mmol), Dioxane (10.0 mL, 136.0 mmol), DI H_2O (6.0 mL, 332.4 mmol), and $Pd(dppf)Cl_2$ (10 mg, 0.01 mmol) were added. The reaction solution as well as the head space was flushed with $N_2(g)$. The pressure vial was capped quickly, placed into a silicon oil bath, stirred, and heated at 100 °C for 24 hours. To stop the reaction, the stirring function was turned off, the bottom water layer was removed, and an aliquot of nPFNG12 dispersed in Dioxane was removed for further characterization. The polymer in Dioxane (1 mL) was pipetted into DI H_2O (10 mL) to induce precipitation of nPFNG12. The water was decanted from the polymer and nPFNG12 was dried via vacuum filtration.[1,6] **Figure 2.34**: nPFNG12- Batch 2 ^{13}C NMR (800 MHz, $CDCl_3$): δ 7.82-7.69 (br, 1.00 H), 3.63 (br, 9.36 H), 3.54 (br, 3.13 H), 3.42 (br, 0.82 H), 3.37 (br, 1.32 H), 3.27 (br, 0.90 H), 2.90 (br, 0.60 H), 2.78 (br, 0.22 H), 2.56 (br, 0.44 H), 2.44 (br, 0.28 H), 2.23 (br, 0.32 H), 2.04 (br, 2.04 H), 0.95- 0.88 (br, 0.45 H) **Figure 2.35**: nPFNG12- Batch 2 ^{13}C NMR (800 MHz, $CDCl_3$): δ 150.1, 140.2, 127.0, 126.10, 121.6, 120.3, 72.1, 70.7, 70.2, 67.3, 60.1, 59.2, 45.5, 38.1, 29.9.

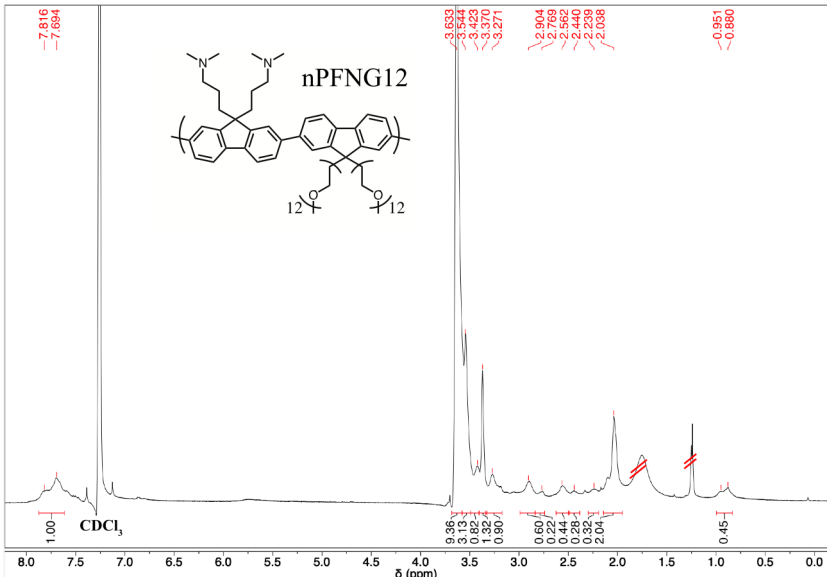

Figure 2.34 nPFNG12- Batch 2 ^{1}H NMR with trace amount of water and pinacol.

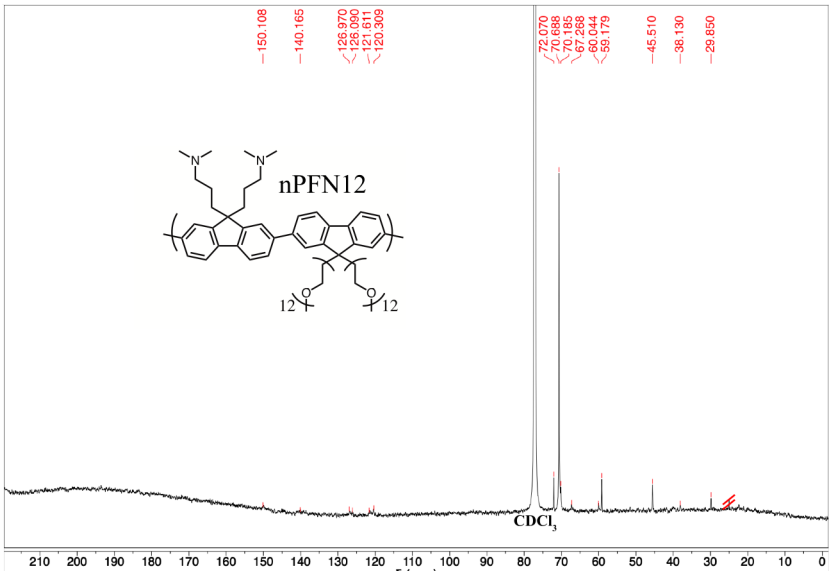

Figure 2.35 nPFNG12- Batch 2 ^{13}C NMR

2.5 Synthesis of Conjugated Polyelectrolytes

2.5.1 Conjugated Polyelectrolyte PFNG3- Batch 1

Conjugated Polyelectrolyte poly([9,9-bis(3'-(N,N,N-trimethyl-ammonium)-propyl)-fluorene]-alt-co-[9,9-bis-(2-(2-(2-methoxy-ethoxy) ethoxy) ethyl)- fluorene] In-situ quaternization of nPFNG3 occurred via the addition of methyl iodide (MeI, 4.0 mL, 64.3 mmol) directly to the remaining dioxane layer containing nPFNG3. After reacting for 2 hours, a small aliquot of DI H_2O was added to help dissolve the precipitated polymer. The reaction was heated to 50 °C for 5 days and DI H_2O was added until there was no more headspace in the pressure vial. After 5 days, the remaining MeI was quenched with a solution of NaOH. Upon addition of NaOH, some of the newly formed PFNG3 precipitated out of the solution. The solution along with some precipitate was dialyzed via Snakeskin dialysis tubing (10,000 MWCO) submerged in a vat of DI H_2O. The DI H_2O was replaced with fresh DI H_2O every day for 5 days. After 5 days, the dialyzed solution of PFNG3 was concentrated under reduced pressure, filtered, transferred into a 50 mL Falcon tube, and lyophilized to yield PFNG3 as a yellow solid (60 mg, 9.4% yield).[1,6] **Figure 2.36**: PFNG3- Batch 1 ^{1}H NMR (800 MHz, D_2O): δ 8.05- 7.91 (br, 1.00 H), 3.41 (br, 1.59 H), 3.27 (br, 2.55 H), 3.12 (br, 0.85 H), 3.00 (br, 0.39 H), 2.81 (br, 3.47 H), 2.65 (br, 0.13 H), 2.41 (br, 0.09 H), 1.21- 1.14 (br, 0.12 H) **Figure 2.37**: PFNG3- Batch 1 ^{13}C NMR (800 MHz, $CDCl_3$):

δ 215.6, 161.1, 150.4, 140.6, 140.0, 127.4, 121.6, 120.9, 70.9, 69.3, 68.9, 67.0, 66.5, 58.0, 54.6, 52.5, 51.9, 38.7, 38.3, 35.3, 30.2, 30.1, 29.96, 29.87, 29.7, 29.6, 29.5, 17.6.

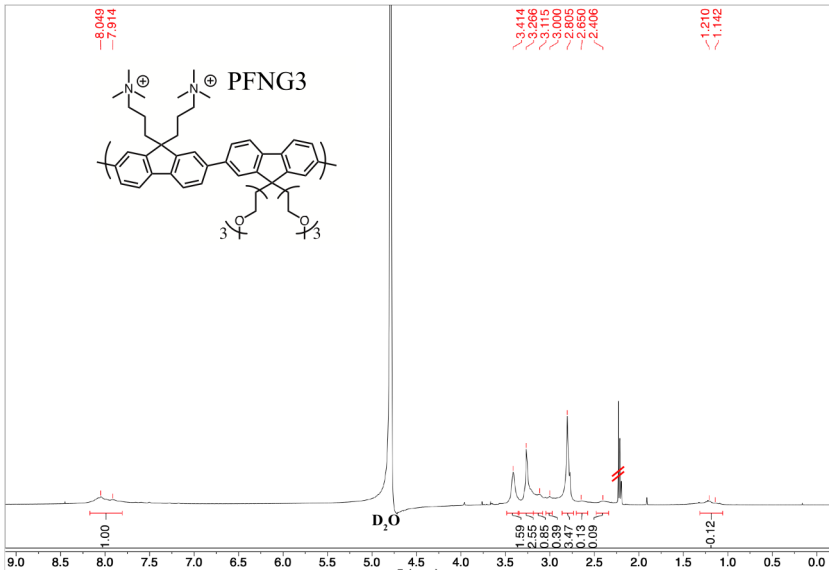

Figure 2.36 PFNG3- Batch 1 ^{1}H NMR with trace amount of acetone.

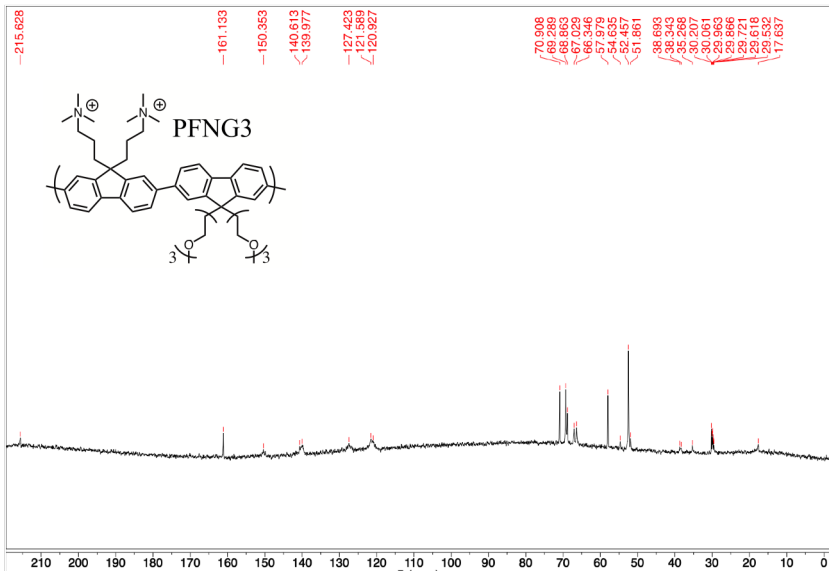

Figure 2.37 PFNG3- Batch 1 ^{13}C NMR

2.5.2 Conjugated Polyelectrolyte PFNG6- Batch 1

Conjugated polyelectrolyte poly([9,9-bis(3'-(N,N,N-trimethyl-ammonium)-propyl)-fluorene]-alt-co-[9,9-bis-(2-(2-(2-(2-(2-(2-methoxy-ethoxy) ethoxy) ethoxy) ethoxy) ethoxy) ethyl)- fluorene] In-situ quaternization of nPFNG6 occurred via the addition of methyl iodide (MeI, 2.5 mL, 40.2 mmol) directly to the remaining dioxane layer containing nPFNG6. After reacting for 2 hours, a small aliquot of DI H_2O was added to help dissolve the precipitated polymer. The reaction was heated to 50 °C for 5 days and DI H_2O was added until there was no more headspace in the pressure vial. After 5 days, the remaining MeI was quenched with a solution of NaOH. Upon addition of NaOH, some of the newly formed PFNG6 precipitated out of the solution. The solution along with some precipitate was dialyzed via Snakeskin dialysis tubing (10,000 MWCO) submerged in a vat of DI H_2O. The DI H_2O was replaced with fresh DI H_2O every day for 5 days. After 5 days, the dialyzed solution of PFNG6 was concentrated under reduced pressure, filtered, transferred into a 50 mL Falcon tube, and lyophilized to yield PFNG6 as a dark yellow solid (240 mg, 40.1% yield).[1,6]

Figure 2.38: PFNG6- Batch 1 ^{1}H NMR (800 MHz, D_2O): δ 8.06- 7.93 (br, 1.00 H), 3.59 (br, 4.79 H), 3.43 (br, 0.84 H), 3.31 (br, 1.55 H), 3.24 (br, 0.74 H), 3.01 (br, 0.64 H), 2.84 (br, 3.25 H), 2.65 (br, 0.43 H), 2.41 (br, 0.20 H), 1.25- 1.16 (br, 0.16 H) **Figure 2.39**: PFNG6- Batch 1 ^{13}C NMR (800 MHz, $CDCl_3$): δ 215.7, 161.3, 150.4, 149.8, 140.6, 140.2, 127.4, 126.8, 121.7, 121.1, 120.9, 71.0, 69.5, 69.0, 67.1, 66.3, 58.0, 54.6, 52.5, 51.9, 38.7, 35.4, 30.2, 30.1, 30.0, 29.9, 29.7, 29.6, 17.8, 17.6.

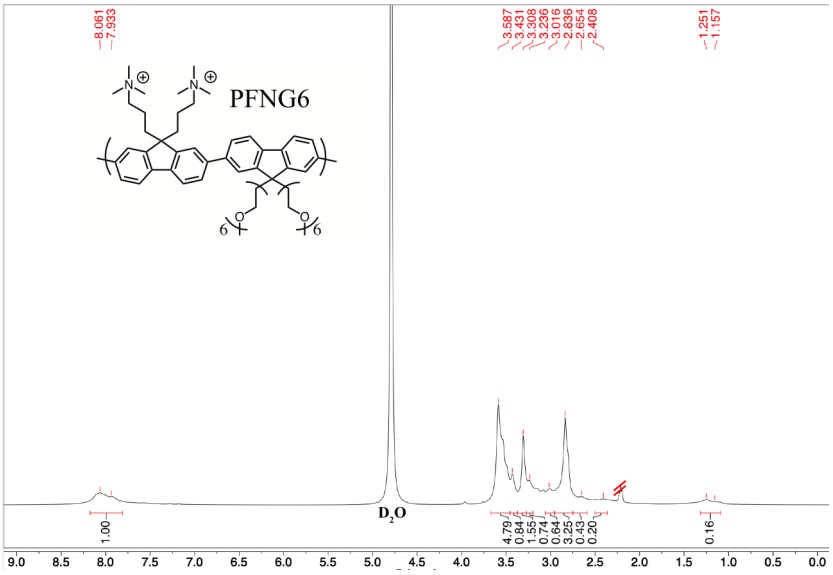

Figure 2.38 PFNG6- Batch 1 ^{1}H NMR with trace amount of acetone.

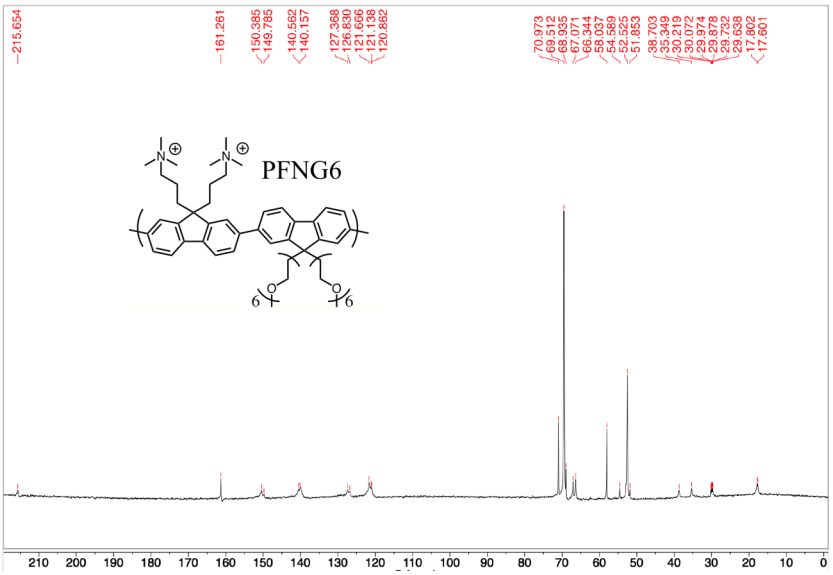

Figure 2.39 PFNG6- Batch 1 ^{13}C NMR

2.5.3 Conjugated Polyelectrolyte PFNG9- Batch 1

Conjugated polyelectrolyte poly([9,9-bis(3'-(N,N,N-trimethyl-ammonium)-propyl)-fluorene]-alt-co-[9,9-bis-(2-(2-(2-(2-(2-(2-(2-(2-methoxy-ethoxy) ethoxy) ethoxy) ethoxy) ethoxy) ethoxy) ethoxy) ethyl)- fluorene] In-situ quaternization of nPFNG9 occurred via the addition of methyl iodide (MeI, 1.5 mL, 24.1 mmol) directly to the remaining dioxane layer containing nPFNG9. After reacting for 2 hours, a small aliquot of DI H_2O was added to help dissolve the precipitated polymer. The reaction was heated to 50 °C for 5 days and DI H_2O was added until there was no more headspace in the pressure vial. After 5 days, the remaining MeI was quenched with a solution of NaOH. Upon addition of NaOH, some of the newly formed PFNG6 precipitated out of the solution. The solution along with some precipitate was dialyzed via Snakeskin dialysis tubing (10,000 MWCO) submerged in a vat of DI H_2O. The DI H_2O was replaced with fresh DI H_2O every day for 5 days. After 5 days, the dialyzed solution of PFNG9 was concentrated under reduced pressure, filtered, transferred into a 50 mL Falcon tube, and lyophilized to yield PFNG9 as a brown solid (60 mg, 10.4% yield).[1,6] **Figure 2.40**: PFNG9- Batch 1 ^{1}H NMR (800 MHz, D_2O): δ 8.07- 7.95 (br, 1.00 H), 3.63 (br, 5.21 H), 3.57 (br, 2.61 H), 3.50 (br, 0.63 H), 3.44 (br, 0.71 H), 3.34 (br, 1.49 H), 3.25 (br, 0.48 H), 3.16 (br, 0.48 H), 3.10 (br, 0.19 H), 3.02, (br, 0.37 H), 2.93 (br, 0.34 H), 2.85 (br, 2.72 H), 1.26 (br, 0.13 H) **Figure 2.41**: PFNG9-Batch 1 ^{13}C NMR (800 MHz, $CDCl_3$): δ 215.7, 161.6, 150.4, 149.8, 140.5, 139.8,

127.3, 126.8, 121.6, 120.9, 70.1, 71.0, 69.6, 69.0, 67.1, 66.37, 62.48, 58.1, 54.6, 52.6, 51.8, 38.6, 35.4, 29.8, 17.9.

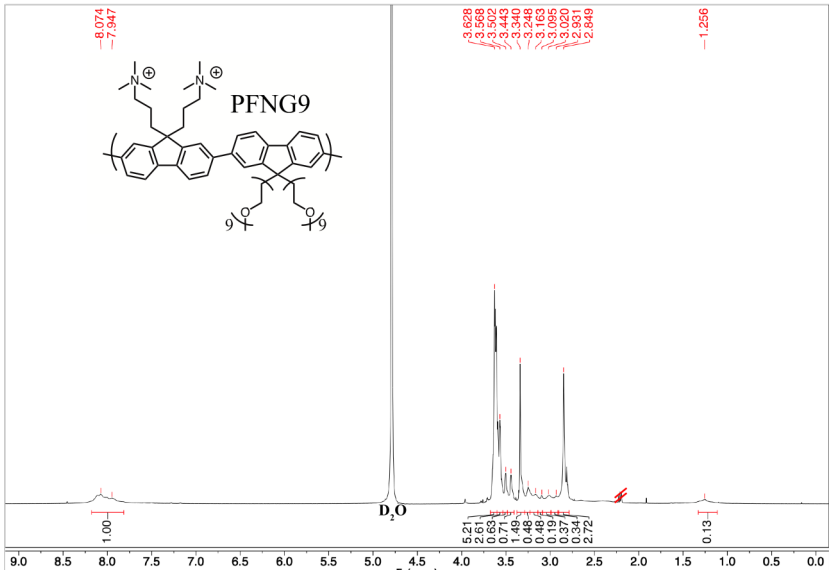

Figure 2.40 PFNG9- Batch 1 ^{1}H NMR with trace amount of acetone.

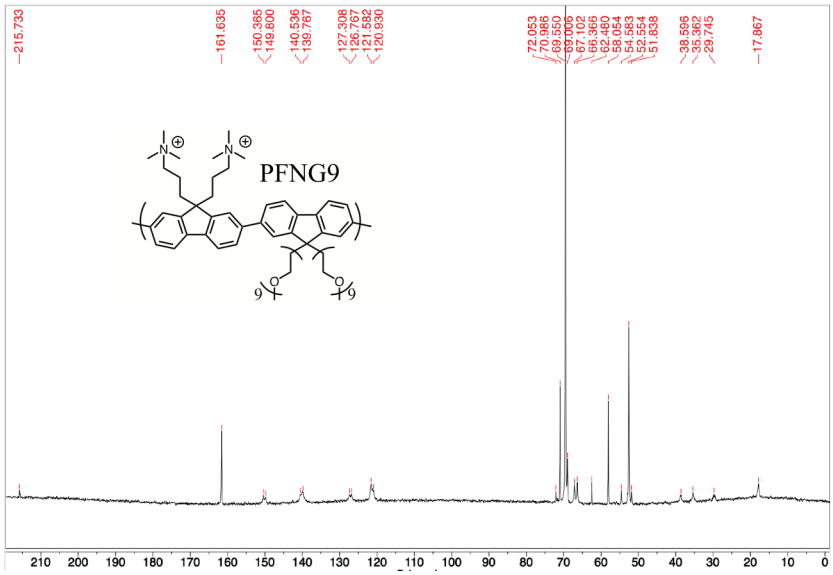

Figure 2.41 PFNG9- Batch 1 ^{13}C NMR

2.5.4 Conjugated Polyelectrolyte PFNG3- Batch 2

Conjugated polyelectrolyte poly([9,9-bis(3'-(N,N,N-trimethyl-ammonium)-propyl)-fluorene]-alt-co-[9,9-bis-(2-(2-(2-methoxy-ethoxy) ethoxy) ethyl)- fluorene] The Dioxane containing nPFNG3 was transferred into a 350 mL pressure vessel. Then quaternization occurred via the addition of methyl iodide (MeI, 1.0 mL, 16.1 mmol) directly to the remaining dioxane layer containing nPFNG3. The cap was threaded onto the pressure vessel, heated to 80 °C for 24 hours, and allowed to cool back down to room temperature before the cap was unscrewed. An aliquot of DI H_2O (200 mL) was added to help dissolve the precipitated polymer. The cap was threaded back onto the pressure vessel and was reheated to 80 °C for an additional 3 days. After which, the pressure vessel was cooled down to room temperature and uncapped. Once the cap was removed, the reaction contents were reheated to 80 °C to remove unreacted MeI from the reaction and reduced the volume of the reaction to 250 mL. The polymer solution was then dialyzed via a dialysis flask (10,000 MWCO) submerged in a vat of DI H_2O. The DI H_2O was replaced with fresh DI H_2O every day for 5 days. After 5 days, the dialyzed solution of PFNG3 was concentrated under reduced pressure, filtered, transferred into a 50 mL Falcon tube, and lyophilized to yield a minimal amount of PFNG3 (< 10 mg, 0.0% yield).[1,6]

2.5.5 Conjugated Polyelectrolyte PFNG6- Batch 2

Conjugated polyelectrolyte poly([9,9-bis(3'-(N,N,N-trimethyl-ammonium)-propyl)-fluorene]-alt-co-[9,9-bis-(2-(2-(2-(2-(2-(2-methoxy-ethoxy) ethoxy) ethoxy) ethoxy) ethoxy) ethyl)- fluorene] The Dioxane containing nPFNG6 was transferred into a 350 mL pressure vessel. Then quaternization occurred via the addition of methyl iodide (MeI, 1.0 mL, 16.1 mmol) directly to the remaining dioxane layer containing nPFNG6. The cap was threaded onto the pressure vessel, heated to 80 °C for 24 hours, and allowed to cool back down to room temperature before the cap was unscrewed. An aliquot of DI H_2O (200 mL) was added to help dissolve the precipitated polymer. The cap was threaded back onto the pressure vessel and was reheated to 80 °C for an additional 3 days. After which, the pressure vessel was cooled down to room temperature and uncapped. Once the cap was removed, the reaction contents were reheated to 80 °C to remove unreacted MeI from the reaction and reduced the volume of the reaction to 250 mL. The polymer solution was then dialyzed via a dialysis flask (10,000 MWCO) submerged in a vat of DI H_2O. The DI H_2O was replaced with fresh DI H_2O every day for 5 days. After 5 days, the dialyzed solution of PFNG6 was concentrated under reduced pressure, filtered, transferred into a 50 mL Falcon tube, and lyophilized to yield PFNG6 as a dark yellow solid (270 mg, 26.0% yield).[1,6] **Figure 2.42**: PFNG6- Batch 2 ^1H NMR (800 MHz, D_2O): δ 8.05- 7.91 (br, 1.00 H), 3.57 (br, 8.18 H), 3.52 (br, 6.09 H), 3.46 (br, 2.13 H), 3.30 (br, 4.98 H), 3.22 (br, 2.16 H), 3.00 (br, 2.01 H), 2.81 (br, 11.01 H), 2.66 (br, 1.57 H), 2.34 (br, 1.23 H), 1.17 (br, 0.26 H) **Figure 2.43**: PFNG6- Batch 2 ^{13}C NMR (800 MHz, $CDCl_3$): δ 215.4, 150.9,

140.6, 140.0, 127.3, 121.8, 120.9, 71.0, 69.6, 69.0, 67.1, 66.3, 58.1, 52.6, 38.7, 35.3, 30.2, 17.6.

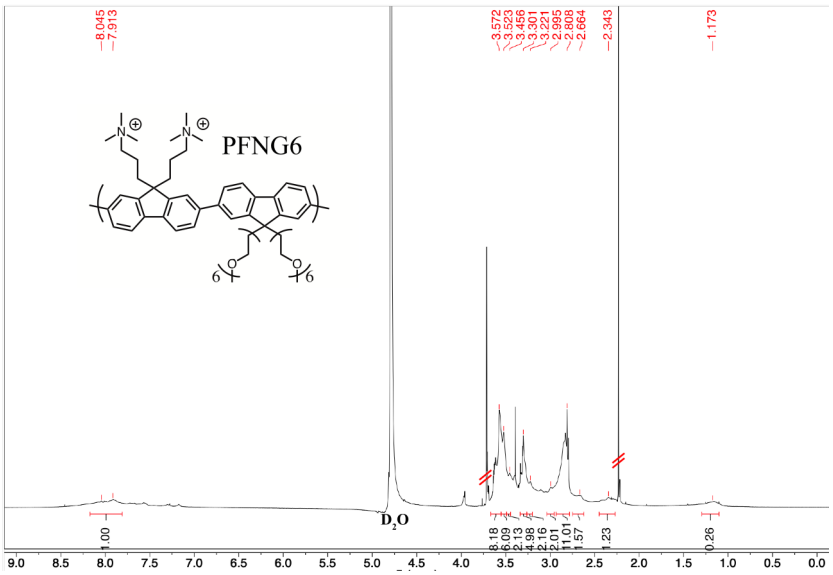

Figure 2.42 PFNG6- Batch 2 ^{1}H NMR with trace amount of dioxane and acetone.

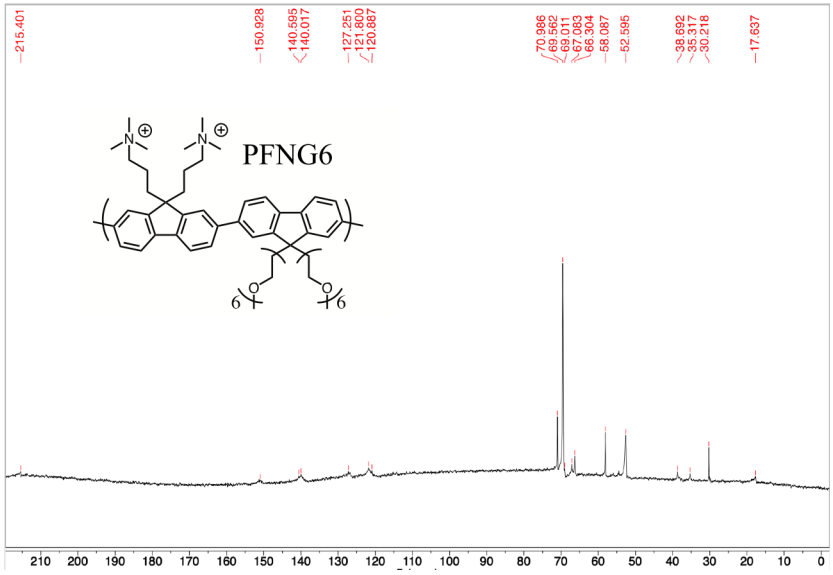

Figure 2.43 PFNG6- Batch 2 ^{13}C NMR

2.5.6 Conjugated Polyelectrolyte PFNG9- Batch 2

Conjugated polyelectrolyte poly([9,9-bis(3'-(N,N,N-trimethyl-ammonium)-propyl)-fluorene]-alt-co-[9,9-bis-(2-(2-(2-(2-(2-(2-(2-(2-methoxy-ethoxy) ethoxy) ethoxy) ethoxy) ethoxy) ethoxy) ethoxy) ethoxy) ethyl)- fluorene] The Dioxane containing nPFNG9 was transferred into a 350 mL pressure vessel. Then quaternization occurred via the addition of methyl iodide (MeI, 1.0 mL, 16.1 mmol) directly to the remaining dioxane layer containing nPFNG9. The cap was threaded onto the pressure vessel, heated to 80 °C for 24 hours, and allowed to cool back down to room temperature before the cap was unscrewed. An aliquot of DI H_2O (200 mL) was added to help dissolve the precipitated polymer. The cap was threaded back onto the pressure vessel and was reheated to 80 °C for an additional 3 days. After which, the pressure vessel was cooled down to room temperature and uncapped. Once the cap was removed, the reaction contents were reheated to 80 °C to remove unreacted MeI from the reaction and reduced the volume of the reaction to 250 mL. The polymer solution was then dialyzed via a dialysis flask (10,000 MWCO) submerged in a vat of DI H_2O. The DI H_2O was replaced with fresh DI H_2O every day for 5 days. After 5 days, the dialyzed solution of PFNG9 was concentrated under reduced pressure, filtered, transferred into a 50 mL Falcon tube, and lyophilized to yield PFNG6 as a brown solid (320 mg, 24.6% yield).[1,6] **Figure 2.44**: PFNG9- Batch 2 ^{1}H NMR (800 MHz, D_2O): δ 8.06- 7.93 (br, 1.00 H), 3.63 (br, 2.66 H), 3.58 (br, 2.27 H), 3.34 (br, 0.67 H), 3.28 (br, 0.17 H), 3.22 (br, 0.17 H), 2.98 (br, 0.17 H), 2.80 (br, 1.65 H), 2.68 (br, 0.06 H), 2.36 (br, 0.28 H), 1.17 (br, 0.38 H) **Figure 2.45**: PFNG9- Batch 2 ^{13}C NMR (800 MHz,

$CDCl_3$): δ 151.2, 140.6, 139.8, 128.4, 127.1, 121.7, 120.8, 71.8, 71.0, 69.6, 67.1, 66.6, 66.3, 60.4, 58.1, 54.3, 52.6, 38.7, 35.2, 30.2, 17.7.

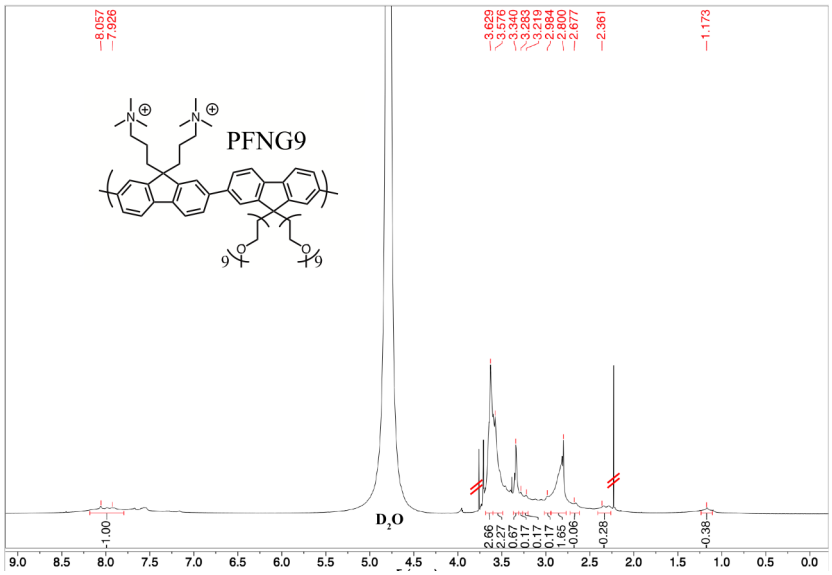

Figure 2.44 PFNG9- Batch 2 ^{1}H NMR with trace dioxane and acetone.

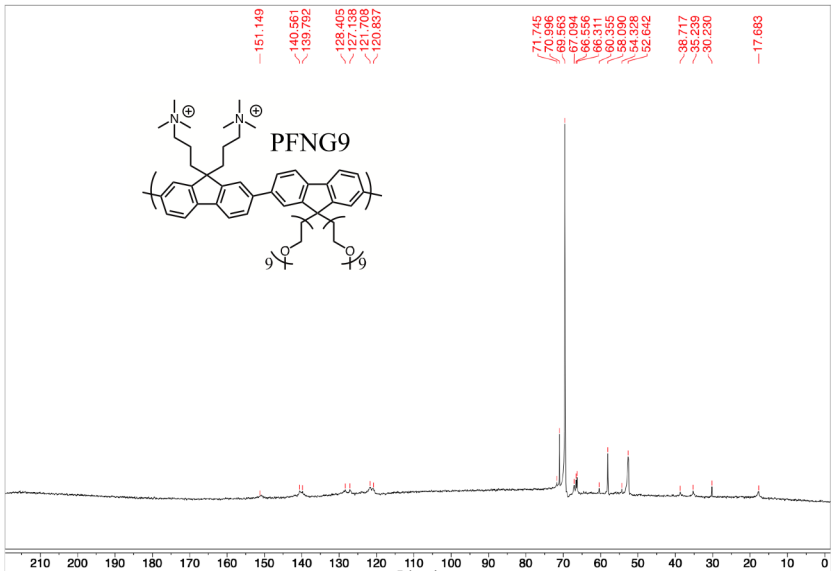

Figure 2.45 PFNG9- Batch 2 ^{13}C NMR

2.5.7 Conjugated Polyelectrolyte PFNG12- Batch 2

Conjugated polyelectrolyte poly([9,9-bis(3'-(N,N,N-trimethyl-ammonium)-propyl)-fluorene]-alt-co-[9,9-bis-(2-(2-(2-(2-(2-(2-(2-(2-(2-(2-(2-methoxy-ethoxy) ethoxy) ethoxy) ethoxy) ethoxy) ethoxy) ethoxy) ethoxy) ethoxy) ethoxy) ethyl)- fluorene] The Dioxane containing nPFNG12 was transferred into a 350 mL pressure vessel. Then quaternization occurred via the addition of methyl iodide (MeI, 1.0 mL, 16.1 mmol) directly to the remaining dioxane layer containing nPFNG12. The cap was threaded onto the pressure vessel, heated to 80 °C for 24 hours, and allowed to cool back down to room temperature before the cap was unscrewed. An aliquot of DI H_2O (200 mL) was added to help dissolve the precipitated polymer. The cap was threaded back onto the pressure vessel and was reheated to 80 °C for an additional 3 days. After which, the pressure vessel was cooled down to room temperature and uncapped. Once the cap was removed, the reaction contents were reheated to 80 °C to remove unreacted MeI from the reaction and reduced the volume of the reaction to 250 mL. The polymer solution was then dialyzed via a dialysis flask (10,000 MWCO) submerged in a vat of DI H_2O. The DI H_2O was replaced with fresh DI H_2O every day for 5 days. After 5 days, the dialyzed solution of PFNG12 was concentrated under reduced pressure, filtered, transferred into a 50 mL Falcon tube, and lyophilized to yield PFNG12 as a brown solid (880 mg, 56.4% yield).[1,6] **Figure 2.46**: PFNG12- Batch 2 ^{1}H NMR (800 MHz, D_2O): δ 8.06- 7.92 (br, 1.00 H), 3.66 (br, 136.84 H), 3.60 (br, 80.32 H), 3.36 (br, 24.95 H), 3.10 (br, 11.13 H), 2.82 (br, 48.60 H), 2.67 (br, 3.95 H), 2.35 (br, 2.27 H), 1.17 (br, 2.83 H) **Figure 2.47**: PFNG12- Batch 2 ^{13}C NMR (800

MHz, $CDCl_3$): δ 215.4, 150.7, 140.0, 127.1, 121.8, 120.8, 71.7, 71.0, 69.6, 67.1, 66.3, 58.1, 55.9, 54.4, 52.6, 51.9, 38.7, 35.3, 30.2, 17.7.

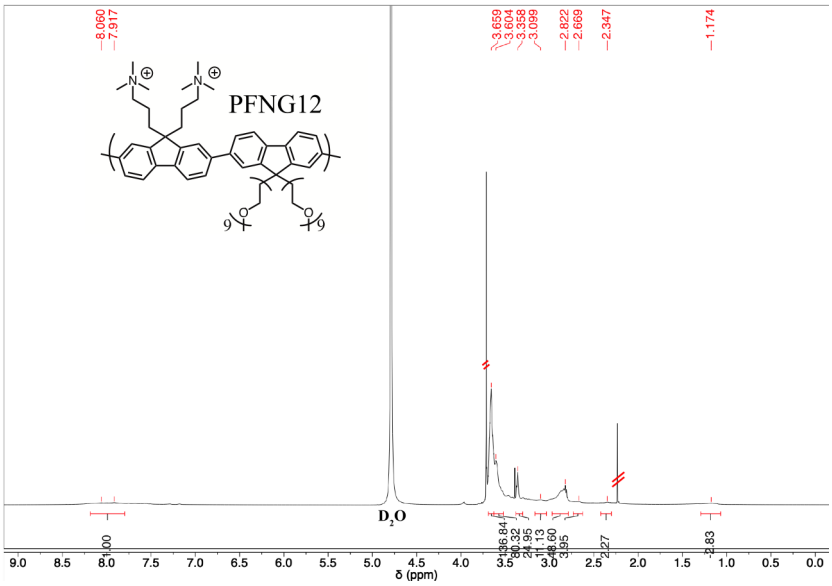

Figure 2.46 PFNG12- Batch 2 ^{1}H NMR with trace amount of dioxane and acetone.

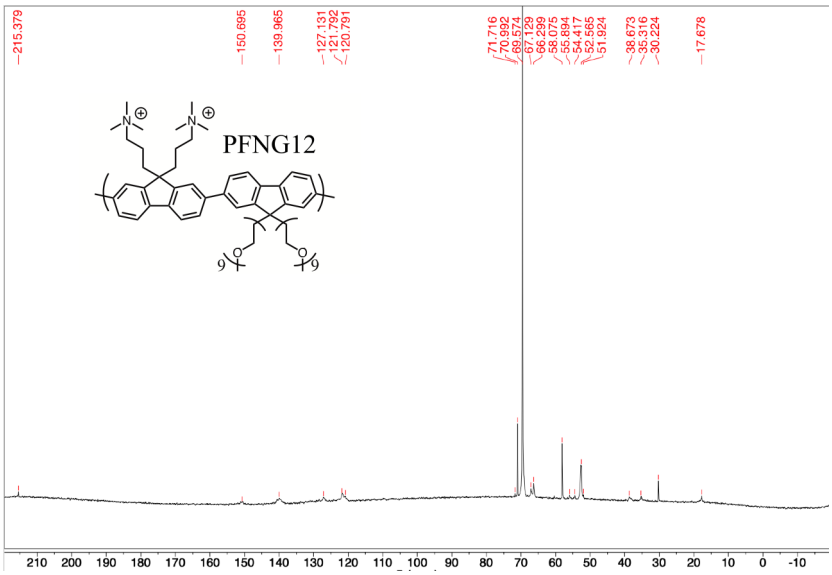

Figure 2.47 PFNG12- Batch 2 ^{13}C NMR

2.6 Conclusion

This chapter describes the synthesis of a CPE series with enhanced aqueous solubility. Two batches of PFNGX have been synthesized via a sequence of tosylation, SN_2, Miyaura borylation, Suzuki cross-coupling, and quaternization reactions.[1–6] The first batch consisted of a PFNGX series where X was equal to 3, 6, or 9. The second batch consisted of the same series but also included X equals 12.

The first observable is that when working with oEG chain lengths beyond 6 ethylene glycol units, crystallization was inhibited. Recrystallization of FG3 was possible, albeit difficult, however FG6, FG9, and FG12 could not be crystallized. Monomers FG6 through FG12 oiled out of the solvent even when allowed to cool very slowly from hot DCM: hexanes (solvent: antisolvent) mixtures.

For reactions where sodium hydride was used as the base, an unquenched crude reaction mixture could not be used directly as the TLC sample. This was attributed to a product that was likely charged and interacted strongly with the silica on the TLC plate. The way to solve this issue was to remove a small portion of the reaction mixture, quench it with water, and dry it over sodium sulfate. The quenched reaction mixture was decanted from the sodium sulfate and was then used to spot onto the TLC plate. This allowed for the neutral product to travel from the baseline, allowing the reaction progress to be monitored.

The next point is that even with the extremely polar elution solvents (such as methanol and water), monomer FN could not be eluted from a silica gel column. Use of triethylamine to deprotonate acidic sites on the silica gel allowed for elution of the

amine-containing molecule. This can be used as an advantage since other impurities without an amine functionality would elute easily with polar solvent in the absence of triethylamine while the amine-containing product would stay bound. This effect was exacerbated by the product having two pendant amine moieties and therefore potentially acting as bidentate with the acidic sites on the silica gel. FN would stay bound to the column even if one amine became unbound and the product would only elute if both amine groups did not participate in binding to the silica gel.

Rather than borylating FN with 2-isopropoxy-4,4,5,5-tetramethyl-1,3,2-dioxaborolane and *n*-butyl lithium, borylation of the amine-containing product occurred through nonconventional means with B_2Pin_2, $Pd(dppf)Cl_2$, and KOAc in DMF. The reason the latter was chosen was to minimize the hazards in the laboratory, since *n*-butyl lithium is a liquid pyrophoric reagent. However, this nonconventional route was originally thought of as not viable for borylation of a tertiary amine-containing aryl-bromide, due to having quite similar reaction conditions to the Buchwald-Hartwig coupling. However, use of B_2Pin_2 turns out to ₙe a highly robust method for borylation, as these conditions were first applied to the other dibrominated fluorene monomers, and successful on a multi-gram scale.

Silica gel chromatographic purification was not successful for the borylated amine-containing product. When attempting to elute the product from the column, only degraded materials were obtained. This suggests that the competing triethylamine added to the elution solvent was non-innocent, either forming a Lewis acid-base adduct with the boron of the boronic ester or acting as a nucleophile and attacking the boron

with concomitant displacement of the pinacol ester. Instead, the borylated amine-containing product was purified by recrystallization in acetone with very satisfying yields of > 60%.

As mentioned in the previous chapter, the electronic properties and the conformation of conjugated polymers are intimately tied. Polymerization conditions were explored with the aim to create very high molecular weight polymers. Three different solvents were tested: toluene, anisole, and dioxane. Various polymerization durations spanning from 1 to 7 days were explored at 100 ℃. The palladium catalyst, base, and molar equivalents were not varied. Two notable outcomes lead to the choice of dioxane as the solvent with a reaction time of 1-2 days. The first outcome was that according to UV-vis absorption spectroscopy, the chromophore length was invariant with regard to the polymerization conditions. The neutral polymer intermediate was desired, in order to interrogate its properties before being quaternized. Precipitation to isolate the neutral polymer requires a polymerization solvent that is miscible with water; the anti-solvent. However, after precipitating the polymer, it was extremely difficult to completely redissolve it in hot dioxane, the same solvent from which it had just been polymerized. This is attributed to making very long polymer chains, with a high propensity to become entangled. Therefore, since the polymerization time didn't seem to affect the chromophore length, two polymerization durations were chosen to maximize the yield of soluble polymers, as there was not any use in making a polymer that cannot be studied in solution or solution-processed into solid-state materials.

Upon in-situ quaternization of the nPFNGX series to form the PFNGX series, quenching of the excess methyl iodide reagent was required for a safe work-up. Therefore, an aqueous solution of sodium hydroxide was used to quench the methyl iodide, forming methanol and sodium iodide. While this looks reasonable on paper, it resulted in precipitation of the polymers. It was desirable to keep the polymers dissolved, since dialysis was to be used for the purification of the final PFNGX series. The precipitation of the polymers greatly hindered the amount of polymer that was able to be dialyzed and therefore the overall yields suffered. During the second batch of polymerizations, heat was used to quench the reactions since methyl iodide is extremely volatile, with a boiling point of 42 ℃. This allowed for much higher yields to be obtained of the polymers, since the polymers stayed dissolved.

The yields of the various PFNGX derivatives provided insight into the polymerization conditions. Although batch dependent polymerization conditions were held constant in the synthesis of each PFNGX derivatives, yields varied. The conditions that favored the formation of PFNG12 were not the conditions suitable to form PFNG3 in high yields. This was particularly accute when quaternizing the neutral polymers. The original procedure for quaternization stated that after methyl iodide was added to the reaction vessel, water should be added to help dissolve the precipitates. To keep everything the same across the chemical series, the same volume of water was added to each vessel. Precipitation of the increasingly insoluble polymer occurred. However, each polymer required a slightly different solvent environment to redissolve. This was

seen in the very low yield for PFNG3: less than 10 mg were obtained compared to PFNG12, where 880 mg of material was obtained.

Lastly, when characterizing the chemical series by NMR, the use of the 800 MHz NMR spectrometer under very high concentrations and many scans were needed to obtain a carbon-13 NMR that included the aromatic resonances. However, this led to aggregation of the NMR sample and therefore the resulting proton NMR spectra showed only weak aromatic signals, making the peaks difficult to integrate. This was challenging as the aromatic protons were used as a reference to determine the number of sidechains successfully appended to the fluorene core.

The target exciton-donor CPE series was successfully synthesized and purified. This allowed for interrogation of the effect of oEG chain length on complexation of PFNGX to PTAK, and on EET between PFNGX and PTAK. The next chapter will describe the results from complexation and EET experiments.

2.7 References

(1) Pu, K.-Y.; Wang, G.; Liu, B. *Design and Synthesis of Conjugated Polyelectrolytes*; John Wiley & Sons Inc., 2013, pp 16-17.

(2) Heathcote, R.; Howell, J. A. S.; Jennings, N.; Cartlidge, D.; Cobden, L.; Coles, S.; Hursthouse, M. Gold(i)–Isocyanide and Gold(i)–Carbene Complexes as Substrates for the Laser Decoration of Gold onto Ceramic Surfaces. *Dalton T* 2007, *0* (13), 1309–1315. https://doi.org/10.1039/b617347k.

(3) Meng, B.; Song, H.; Chen, X.; Xie, Z.; Liu, J.; Wang, L. Replacing Alkyl with Oligo(Ethylene Glycol) as Side Chains of Conjugated Polymers for Close π–π Stacking. *Macromolecules* 2015, *48* (13), 4357–4363. https://doi.org/10.1021/acs.macromol.5b00702.

(4) Wang, H.; Lu, P.; Wang, B.; Qiu, S.; Liu, M.; Hanif, M.; Cheng, G.; Liu, S.; Ma, Y. A Water-Soluble Π-Conjugated Polymer with up to 100 Mg · mL−1 Solubility. *Macromol Rapid Comm* 2007, *28* (16), 1645–1650. https://doi.org/10.1002/marc.200700221.

(5) Huang, F.; Wu, H.; Wang, D.; Yang, W.; Cao, Y. Novel Electroluminescent Conjugated Polyelectrolytes Based on Polyfluorene. *Chem Mater* 2004, *16* (4), 708–716. https://doi.org/10.1021/cm034650o.

(6) Pu, K.; Liu, B. Conjugated Polyelectrolytes as Light-Up Macromolecular Probes for Heparin Sensing. *Adv Funct Mater* 2009, *19* (2), 277–284. https://doi.org/10.1002/adfm.200800960.

Chapter 3

Aqueous Light Harvesting Antennae based on Brush-Like Conjugated Polyelectrolyte Complexes: Self-Assembly and Electronic Energy Transfer

Acknowledgments

Gregory M. Pitch performed the bulk of the work discussed in this chapter, however there were some measurements that were performed by Levi Matsushima, and analyzed by Alexander L. Ayzner. The experiments for which LM and ALA contributed a great deal were discussed in sections 3.2.5- Time-resolved photoluminescence, 3.2.6- Small-angle X-ray scattering, and 3.2.7- Dynamic light scattering. For section 3.2.6; GMP prepared solution samples of PFNGX (3, 6, 9), LM performed the measurements, and ALA performed analysis. For sections 3.2.5 and 3.2.7; GMP prepared solution samples of PFNGX (3, 6, 9), LM performed the measurements, and LM (with guidance from ALA) performed analysis.

3.1 Introduction

Constructing a complex artificial light-harvesting systems that can mimic core aspects of natural light-harvesting organelles is a chemical grand challenge. Such a system should exhibit panchromatic light absorption and the ability to rapidly move electronic excited states (excitons) through space. Exciton migration increases the probability that photon energy will eventually be converted to chemical potential energy of spatially separated electron/hole pairs.

It is highly desirable to be able to construct such an artificial light-harvesting system in water – the most environmentally benign medium. However, this desideratum imposes significant additional constraints. This includes the need to impart aqueous solubility to molecular semiconductors that possess the propensity for hydrophobic and π-stacking interactions, as well as the need to ensure that their hierarchical assemblies are stable. Among examples that satisfy these requirements, a particularly elegant one is an aqueous light-harvesting antenna developed by the Tovar group. They used small-molecule organic semiconductors decorated with peptidic side chains to build in specific aggregation motifs while retaining sufficient aqueous solubility. π-Stacking interactions between adjacent organic semiconductors within the assembly gave rise to an electronic coupling and resultant exciton motion down the stacking axis.

The Ayzner lab has shown that electrostatic assemblies of conjugated polyelectrolytes (*CPEs*), water-soluble semiconducting polymers, hold substantial promise as primary building blocks of complex aqueous light-harvesting systems.[1,2]

First, CPEs support highly delocalized electronic states, which leads to rapid intrachain exciton motion down the CPE chain over distances that are large compared to the monomer length. Second, oppositely charged CPEs that function as an exciton donor/acceptor pair may be readily electrostatically assembled to form artificial light-harvesting antennae that exhibit ultrafast (sub-250 fs) exciton transfer. Finally, and crucially, we argue that associative phase separation of aqueous polyelectrolyte assemblies provides a tractable and relatively simple pathway to complex, multi-component and multi-functional light-harvesting systems.[1–3] Our lab has recently showed that associative phase separation of one conjugated and one non-conjugated polyelectrolyte allowed us to form colloidal gels with tunable photophysical properties that were sensitive to specific cation-π interactions.[4]

However, of particular interest is the formation of a liquid complex-coacervate phase, which is a dense, highly polyelectrolyte-enriched liquid. Forming such a coacervate via phase separation from oppositely charged CPEs that function as an exciton donor/acceptor pair would constitute a major step towards light-harvesting soft-matter complexity. Such coacervates could function as photophysically active compartments in a larger overarching system or as fluid exciton-transferring scaffolds for an artificial electron transport chain and molecular catalysts.

Such a CPE-based liquid coacervate has not yet been observed. We hypothesize that this is because associative phase separation is most often induced at ionic stoichiometry of oppositely charged polyelectrolytes. With CPEs, this leads to a net-

neutral complex with many hydrophobic and potentially π-stacking interactions. The result is a solid- or gel-like assembly. Our central hypothesis is that fluidity and stability must come from polar-but-nonionic side chains that do not directly participate in ionic inter-CPE complexation. To increase the aqueous solubility of a net-neutral inter-CPE complex, we synthesized a chemical series of polyfluorene-based CPEs with one ionic monomer and one co-monomer bearing oligoethylene glycol (*oEG*) side chains with 3, 6 and 9 ethylene glycol (*EG*) units. These brush-like CPEs are highly water-soluble and remarkable stable at high ionic strength. We interrogated their self-assembly in isolated solution using a combination of solution scattering methods. Oppositely charged artificial light-harvesting antennae using the synthesized exciton-donor CPE series and a poly(butyl-carboxylate)-thiophene (*PTAK*) exciton-acceptor that was common to all the exciton donors were then formed. Remarkably, the efficiency of electronic energy transfer from the donor to the acceptor CPE does not effectively decrease, even for the longest 9-EG derivative. This illustrates that the CPE microstructure in the complex is such that the long brush-like side chains do not present any appreciable steric hindrance to alignment of CPE transition dipole moments. However, we show that the onset of associative phase separation does in fact depend on oEG length. Our observations have intriguing implications for the construction of light-harvesting complex fluids based on CPEs.

3.2 Experimental Methods

3.2.1 Monomer Synthesis, Suzuki Coupling, and Quaternization

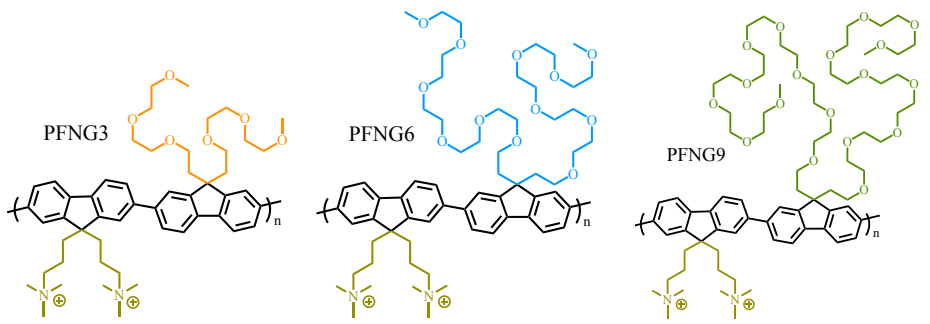

Figure 3.1 Polymer repeat units for PFNGX series (X = 3, 6, 9).

A polyfluorene-based exciton-donor CPE series varying in the length of oEG side chains (PFNGX), where X represents the number of ethylene glycol units in the oEG side chain, was synthesized and is shown in **Figure 3.1**. PFNGX is formed via Suzuki coupling reactions between a dibrominated fluorene monomer functionalized with oEG side chains (*FGX*) (X = 3, 6, 9), and a diborylated (3,3'-dimethylamino-1-propyl) fluorene derivative (*FNB*). This was followed with *in situ* quaternization of pendant alkyl amines on the dibrominated (3,3'-dimethylamino-1-propyl) fluorene co-monomer (*FN*). Purity of synthesized products were evaluated with proton (^{1}H) and carbon (^{13}C) nuclear magnetic resonance (NMR) spectroscopy.

3.2.2 Sample Preparation

Stock solutions of 3 mg/mL PFNGX, and 1 mg/mL PTAK were prepared with HPLC grade water (Sigma-Aldrich) degassed with Ar (g). These solutions were wrapped in aluminum foil, stirred with a Teflon stir bar at 650 r.p.m., and heated at 70

℃ for 6 hours. Upon cooling to room temperature the stock solutions were filtered through 450 nm polyvinylidene difluoride (*PVDF)* filters. Dilute solutions of exciton-donor CPE controls and exciton-donor-acceptor conjugated polyelectrolyte complexes (*CPECs*) were prepared in 1.5 mL natural microcentrifuge tubes (Seal Rite), wrapped in aluminum foil, stirred with a Teflon stir bar at 650 r.p.m., and heated at 70 ℃ in a sand bath for 6 hours. The concentration of PFNGX was held constant at 1.33×10^{-5} M. With respect to PFNGX, the concentration of PTAK in the CPECs required to form molar charge percentages of 25%, 50%, 75% were 6.65×10^{-6} M, 1.33×10^{-5} M, and 2.00×10^{-5} M respectively.

3.2.3 UV-vis Spectroscopy

Optical density (*OD*) measurements were collected of dilute PFNGX CPEs and CPECs on a UV-2700 Shimadzu spectrometer. Spectra were collected in transmission geometry scanning through wavelengths of 300 - 800 nm at 1.0 nm increments. Samples were measured in a 1 mm quartz cuvette.

3.2.4 Steady-State Photoluminescence Spectroscopy

Photoluminescence (*PL*) measurements were collected of dilute PFNGX CPEs and CPECs in a 1 mm quartz cuvette on a Horiba Fluoromax-4 spectrometer in a right angle geometry. The excitation wavelength was set to 375 nm and emission wavelengths were collected from 350 - 800 nm in 1 nm increments, with excitation and emission slit widths of 1nm.

3.2.5 Time-Resolved Photoluminescence Spectroscopy

Time-resolved photoluminescence (*TRPL*) measurements were collected of dilute PFNGX CPEs, carried out on a custom built laser table setup to elucidate the excited state kinetics of each polymer. Based on absorption spectroscopy, the excitation wavelength was chosen to be 375 nm. In order to reduce the chance of scattering, a cut-on filter was used on the detection arm at 400 nm, while the detector was set to collect intensity at 475 nm. The measurements were collected in right-angle geometry with samples loaded into a 1 mm quartz cuvette. Excitation and detection polarizers were offset from each other by 54.7˚ to nullify the effects polarization. FluoroTools DecayFit ™ software was used to calculate the decay times and a double exponential model was used to fit the data.

3.2.6 Small-Angle X-ray Scattering

Small-angle X-ray Scattering (*SAXS*) was conducted at Stanford Linear Accelerator Center (*SLAC*) at Stanford Synchrotron Radiation Laboratory (*SSRL*). SAXS data was used to investigate the contributions of increasing oEG chain length to bulk solution ordering. Samples were irradiated with high energy X-rays (11 keV) and scattering was collected with a Dectris Pilatus3 X 1M detector, with a distance of 1.7 meters. Each sample was irradiated for 16 x 1 second exposures. The intensity of these images were plotted against scattering vector q. Data was background subtracted and averaged with the use of the SAXSPipe SASTools.

3.2.7 Dynamic Light Scattering

Dynamic light scattering (*DLS*) was used to investigate the radius of gyration and diffusion coefficients of the charged polymer series. DLS measurements were carried out using a 637 nm light source and scattered intensity was collected at angles: 45˚, 67˚, 90˚, 112˚, and 135˚. For DLS measurements, all samples were made with high-performance liquid chromatography (*HPLC*) grade water, thus a refractive index of 1.33 was used. The time window layouts were chosen to fully capture the decay in intensity with a first delay of 0.500 μs and a last delay of 1 x 10^5 μs. All measurements were averaged over 5 minutes to produce robust statistical results.

3.2.8 Photoluminescence Excitation Spectroscopy

Photoluminescence excitation (*PLE*) measurements were collected of dilute PFNGX CPEs and CPECs in a 1 mm quartz cuvette on a Horiba Fluoromax-4 spectrometer in a right angle geometry. Excitation wavelengths were scanned from 300 - 800 nm in 1 nm increments, with excitation and emission slit widths of 2 nm.

3.3 Results

3.3.1 Photophysics of Aqueous CPE Solutions

Figure 2.1 shows the synthetic scheme and the chemical structures of our CPE chemical series. After synthesizing and characterizing our CPE series via ^{1}H and ^{13}C NMR, we then examined their photophysics and chain microstructures. Absorption

spectroscopy and PL spectroscopy measurements are discussed first. Then the solution chain structure was interrogated using a combination of small-angle X-ray scattering (*SAXS*) and angle-dependent dynamic light scattering (*DLS*) experiments. Finally, the electronic energy transfer (*EET*) efficiency of our PFNX polymers was investigated by complexing them with an oppositely charged polythiophene-based CPE, which serves as the common exciton-acceptor.

Panel A of **Figure 3.2** shows the OD of each monomer and its corresponding CPE. FNX labels oligoethyleneglycol-containing dibromofluorene monomers, while FNB represents the pinacol boryl ester of the dimethylaminopropyl fluorene monomer. All monomers absorb in the UV and have very similar absorption spectra. As expected, PFNG3, PFNG6, and PFNG9 display strongly redshifted spectra compared to the monomers, with λ_{max} values of 388 nm, 391 nm, and 393 nm , respectively. There is a

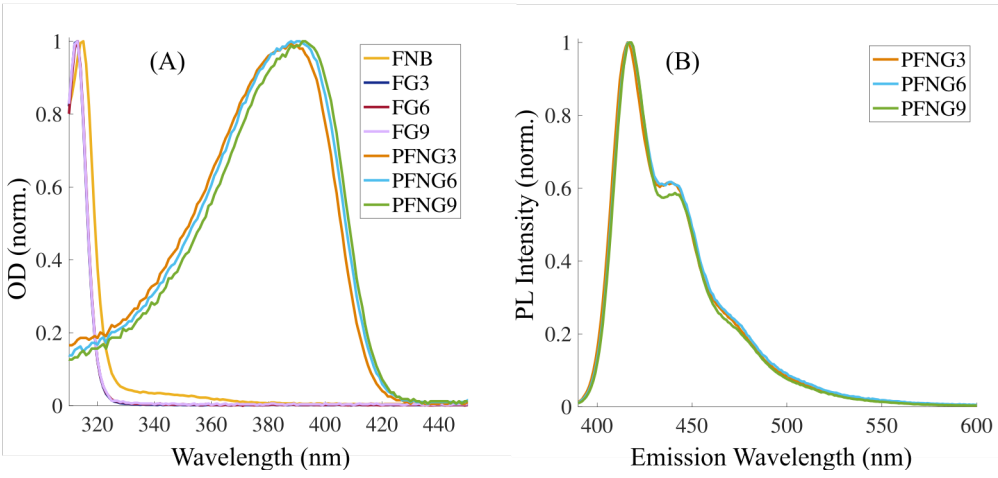

Figure 3.2 (A) Normalized OD of monomers required for synthesis of fluorene-based CPEs, as well as normalized OD of PFNGX CPEs. (B) Normalized PL intensities for PFNGX CPEs

subtle monotonic redshift of λ_{max} from PFNG3 to PFNG6 to PFNG9, which suggests that the mean chromophore length is slightly longer for each successive polymer.

Panel B of **Figure 3.2** shows peak-normalized PL spectra for the three polymers following excitation at 375 nm. The position of the emission maximum is nearly unchanged across the CPE series. However, there is small a difference in the PL intensity ratio corresponding to the 0-0 and 0-1 vibronic peaks, I_{00}/I_{01}. Specifically, I_{00}/I_{01} for PFNG9 is ~5% larger than the other two CPEs. The larger I_{00}/I_{01} emission ratio is indicative of PFNG9 chromophores being slightly more extended in solution, whereas evidently PFNG3 and PFNG6 have similar polymer conformations on average.

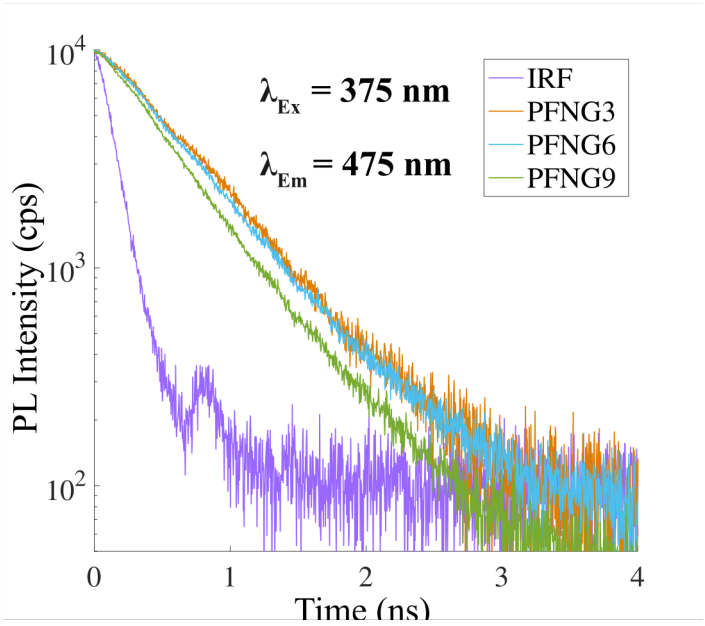

Figure 3.3 Time-resolved decays for PFNGX chemical series. The concentration of each polymer was 1.33 x 10^{-5} M. The excitation wavelength was 375 nm, and the emission wavelength was 475 nm.

Figure 3.3 shows time-resolved PL decays for the polymer series following excitation near the peak of the OD spectrum, along with the instrument response function (*IRF*). The deconvolved decays are biexponential with one dominant PL lifetime component. The average PL lifetimes are similar for the three polymers, but PFNG9 appears to have a long-lifetime component with a slightly larger amplitude.

3.3.2 CPE Coil Microstructure in Salt-Free Aqueous Solutions

Having characterized the photophysical properties of the CPE solutions, we interrogated the structural characteristics of the polyelectrolyte coils in salt-free aqueous solutions. We began by measuring diffusion dynamics using angle-dependent DLS. This technique uses a monochromatic wavelength of 637 nm to illuminate a sample. The particles in the sample interact and scatter the light in all directions, and a detector that sweeps over a set of angles collects the scattered signal.[5]

Diffusing particles are characterized by a diffusion coefficient (D_τ), and is related to the hydrodynamic size of the particles in solution. Diffusion of macromolecular particles through a solution is transitory and leads to fluctuations of scattered light. More specifically, larger particles diffuse more slowly than smaller particles; because of this difference in diffusion, a sample's D_τ can be determined.[5] Scattered light will interact with scattered light from other particles in a sample and results in a time dependent interaction that can be monitored. In DLS experiments, the rate of fluctuations of scattered light can be related to the motion of the particle and therefore can be leveraged to determine a D_τ. The measurable quantity in a DLS experiment is

an intensity correlation function $G_2(\tau)$, which can be expressed as an average of the product of intensities at t and a later time $(t + \tau)$. This relationship is shown in Equation 3.1, where τ is the lag time between two time points.[5]

$$G_2(\tau) = \langle I(t)I(t+\tau)\rangle \tag{3.1}$$

Measurements as a function of scattering angle allow us to interrogate the dependence of the effective diffusion coefficient D_{eff} on the scattering vector length q at low wavenumbers of order 10^{-3} Å^{-1}. **Figure 3.4** shows that $D_{eff} = D_{eff}(q)$ for all three CPEs.

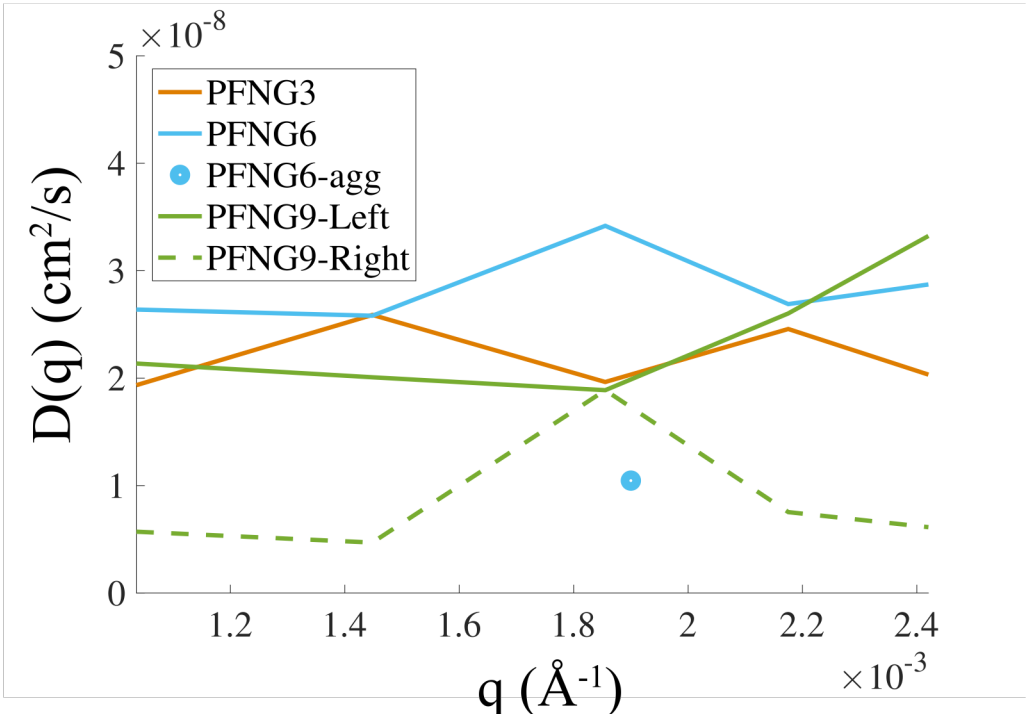

Figure 3.4 Angle-dependent DLS of PFNGX (3, 6 , 9) at 45°, 67°, 90°, 112°, and 135°.

At an angle of 67°, which provides representative D(q) values for PFNGX (3, 6, 9) series, D(q) values are determined as 2.59 x 10^{-8} cm^2/s, 2.58 x 10^{-8} cm^2/s, and 2.01 x 10^{-8} cm^2/s, respectively. The effective diffusion coefficient for polyelectrolyte solutions may be written as Equation 3.2.

$$D_{eff}(q) = \frac{D_0}{S(q)} \tag{3.2}$$

where D_0 is the free particle diffusion coefficient, and $S(q)$ is the static structure factor of the solution. Thus, differences in $D_{eff}(q)$ for the three CPEs likely reflect differences in their respective solution structure, which may reflect both intrachain structure and interactions between different CPE chains.

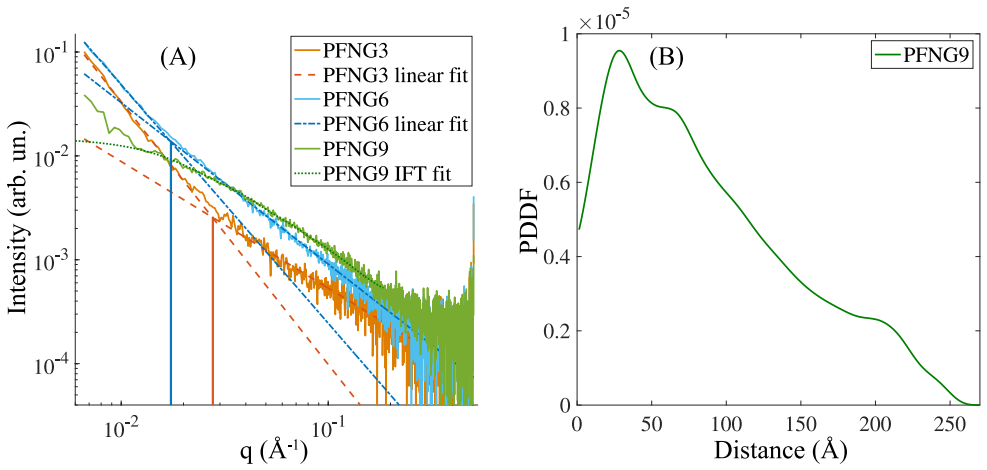

Figure 3.5 Small-angle X-ray scattering (SAXS) of CPE solutions. (A) Reduced SAXS intensities as a function of scattering vector length q. Sloped lines indicate fits to the linear regions, and vertical lines correspond to the intersection point of low-q and high-q linear fits. The green dotted line shows the fit obtained using the indirect Fourier transform (IFT) (B) Pair-distance distribution function (PDDF) obtained in a model-independent manner the IFT.

The fact that DLS measurements on PFNG9 appear to differ significantly from the other two CPEs suggests that a deeper exploration of solution scattering is in order. To this end, we performed small-angle X-ray scattering measurements on our CPE solutions, the results of which are shown in **Figure 3.5**.

Figure 3.5A shows the reduced scattering intensities as a function of q on a double-logarithmic scale for aqueous solutions of the PFNGX polymers at the same molar monomer concentration. PFNG3 and PFNG6 solutions have qualitatively similar curves. The monotonically decreasing intensity shows two linear regions, each with a different slope corresponding to a different power-law exponent. For PFNG3, the low-q and high-q regions have slopes of –2.53 and –1.22, respectively, with the intersection point q^* = 0.0275 Å^{-1}. For PFNG6, the low-q and high-q regions have slopes of –2.30 and –1.55, respectively, with the intersection point q^* = 0.0171 Å^{-1}. A high-q slope of ~ –1 is indicative of rod-like scaling. The q^* that corresponds to a transition from ~ –2 to ~ –1 scaling can be used to crudely estimate the polymer persistence length (l_p) via $q^* l_p \sim 3.5$. This estimate gives a value of l_p for PFGN3 and PFNG6 as ~13 nm and ~21 nm, respectively. These values correspond to approximately 8 repeat units for PFGN3 and 12 repeat units for PFNG6. Although these crude absolute values are likely overestimates, the change in relative magnitude is likely trustworthy.

The SAXS curve for PFNG9 does not qualitatively resemble that of PFNG3 and PFNG6. At q ~ 0.01 Å^{-1} the scattering intensity displays a Guinier-like plateau before increasing further at lower q. Thus, although we performed linear fits to both the low-

q and high-q regions (slopes of –1.95 and –1.37, respectively), we did not attempt to extract a l_p estimate. Instead, the appearance of a Guinier-like plateau allows us to use the indirect Fourier transform to fit the curve over the entire q-range above the low-q linear region. This assumes that the scattering intensity is due to a single scattering "particle" and not an interacting assembly. Although our polymer concentrations are relatively dilute, the assumption of no inter-polyelectrolyte interactions in salt-free aqueous solutions may be questionable. Nevertheless, under this simplifying assumption, we extract the pair-distance distribution function (PDDF) for PFNG9 in a model-independent manner, which is shown in **Figure 3.5B**. We do not attempt to interpret the fine structure of the PDDF. Instead, we note that the general shape is consistent with a quasi-cylindrical particle, and the distance at which the PDDF goes to zero can be approximately associated with the size of the scattering inhomogeneity. This gives a value of ~25 nm for PFNG9.

3.3.3 Energy Transfer in PFNGX Inter-CPE Complexes

With structural and photophysical information about isolated PFNGX solutions in hand, we went on to elucidate the influence of the increasing oEG side chain length on EET. To do so, we formed aqueous CPECs composed of the cationic PFNGX and an anionic polythiophene-based CPE, PTAK. Given the spectral overlap between the OD spectrum of PTAK and the PL spectrum of PFNGX, the PFNGX's serve as exciton donors while PTAK serves as the exciton acceptor.[1,2,6] To evaluate whether PFNGX excitons were undergoing EET to PTAK, we first fixed the donor polymer

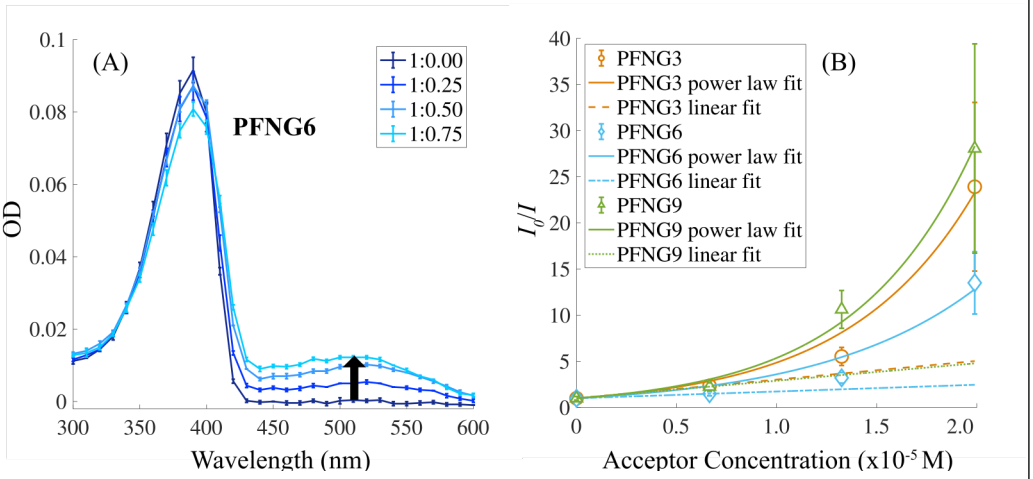

Figure 3.6 (A) Optical densities of PFNG6, and PFNG6 CPECs formed with PTAK at molar charge percentages of 25%, 50%, 75%. (B) Stern-Volmer analysis with error bars for PFNGX CPEs. Specifically, PFNG3 (orange circles), PFNG3 power law fit (orange-solid line), PFNG3 linear fit (orange-dashed line), PFNG6 (blue diamonds), PFNG6 power law fit (blue-solid line), PFNG6 linear fit (blue- dotted dashed line), PFNG9 (green triangles), PFNG9 power law fit (green-solid line), PFNG9 linear fit (green- dotted line).

concentration at 1.33 x10^{-5} M and varied the relative ionic charge ratio between PFNGX and PTAK from 1:0.00 (donor control) to 1:0.75. **Figure 3.6A** shows OD spectra of PFNG6 in isolation as well as with increasing PTAK concentration. CPEC absorption spectra show a characteristic and well-separated peak for each component of the complex. The relatively narrow band near 390 nm corresponds to PFNG6, while the broader peak centered about 520 nm corresponds to PTAK. As expected, the PTAK OD increased monotonically with increasing PTAK concentration, which is indicated by the upward-facing arrow. Corresponding OD spectra for PFNG3 and PFNG9 CPECs are shown in the Appendix in **Figure A1.1**. The molar concentration of each

donor polymer was dilute enough such that its OD was kept < 0.1 to ensure reliability of PL quenching measurements. We find that the PL intensity of donor CPEs decreases monotonically as the acceptor CPE concentration increases. This observation is consistent with EET from PFNGX to PTAK.[1,2,6,7] To quantify the extent of donor PL quenching, we performed Stern-Volmer analysis of the quenching data.[6,8] This consists of plotting the ratio of the PL intensity of the unquenched donor CPE control, I_0, to the intensity of the donor in the presence of the quencher, I, as a function of acceptor concentration. The PL intensity value was chosen to be at the emission wavelength corresponding to the maximum of the PL spectrum (419 nm). **Figure 3.6B** shows the Stern-Volmer plots for the three exciton donor CPEs as a function of molar PTAK concentration. It is clear that over the full range of PTAK concentrations, corresponding to the 1:0.00 through 1:0.75 ionic charge ratio range, I_0/I departs from linearity for all three PFNGX derivatives. Nevertheless, at low acceptor concentrations, I_0/I is locally linear. We were able to fit the intensity ratio over the entire concentration range using a simple power-law functional form according to Equation 3.2,

$$I_0/I = (c/c_0 + 1)^{\beta} \tag{3.2}$$

where c is the acceptor concentration, c_0 is the unit concentration, and β is the sole fitting parameter. We find that β is 1.58 x 10^5, 1.28 x 10^5, and 1.68 x 10^5 for PFNG3, PFNG6, and PFNG9, respectively. For completeness, we also fit the low-c region to a

linear form to extract the Stern-Volmer constant, K_{SV}. Given the nonlinear behavior over the entire c range, we chose to be particularly conservative and to consider only the first two data points in the linear analysis. The slope of the linear fit to the I_0/I vs. [PTAK] plot gives K_{SV}, which is a quantitative measure of quenching efficiency. The K_{SV} values determined from the analysis for PFNG3, PFNG6, and PFNG9 are 2.03 x 10^5 M^{-1}, 7.34 x 10^4 M^{-1}, and 1.90 x 10^5 M^{-1}, respectively. The corresponding donor PL quenching spectra for PFNG3, PFNG6, and PFNG9 CPECs are shown in the Appendix in **Figure A1.2**.

Although the quenching of donor PL by the acceptor CPE is consistent with EET,[1–3] there are other mechanisms, such as excited-state electron transfer, that could also give rise to donor PL quenching. To establish whether we indeed observed EET between PFNGX and PTAK, we measured steady-state photoluminescence excitation (PLE) spectra for each CPEC.[6,9] In this experiment, the PL intensity was measured at a fixed emission wavelength corresponding to emission by the acceptor CPE alone. We then varied the excitation wavelength across the full absorption spectrum of the CPEC while detecting only acceptor PL at the fixed PTAK emission wavelength.

PLE spectra of PFNG3, PFNG6, and PFNG9 each complexed with PTAK at a PFNGX/PTAK ionic molar charge ratio of 25% are shown in **Figure 3.7A**, with the emission wavelength fixed at 680 nm. In **Figure 3.2B**, the PFNGX chemical series emits extremely weakly at 680 nm. In the CPEC where PFNGX emission is strongly quenched, emission from exciton donor CPEs at 680 nm is negligible. **Figure 3.7A**

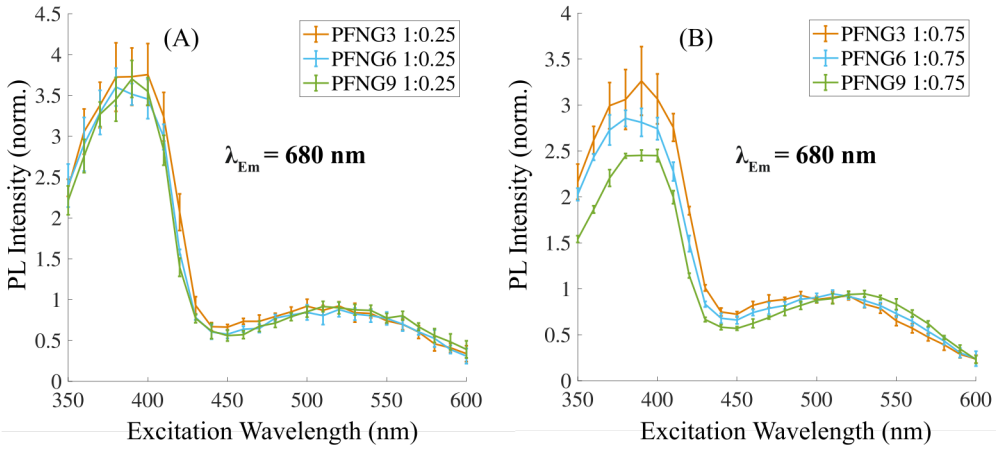

Figure 3.7 (A) Normalized photoluminescence excitation spectra of PFNGX CPECs formed with PTAK at molar charge percentages of 25%. (B) Normalized photoluminescence excitation spectra of PFNGX CPECs formed with PTAK at molar charge percentages of 75%.

shows that photoexcitation of all three PFNGX/PTAK CPECs at photon wavelengths where strong donor absorption occurs, namely between 350 nm and 440 nm, ultimately gives rise to radiative relaxation at 680 nm. Spectra were normalized to the signal corresponding to the peak of the PTAK absorption region ~ 520 nm. The PLE spectrum is seen to effectively trace out the CPEC absorption spectrum (**Figure 3.7A**).[6,9] Taken together with the observation of strong donor PL quenching, the PLE spectrum is unambiguous evidence that excitons initially created on the donor undergo EET to the PTAK acceptor during their excited-state lifetimes.

Since the Stern-Volmer plots showed significant departure from linearity at the high end of the PTAK concentration range, corresponding to a 75% molar charge ratio, it is intriguing to evaluate whether the PLE spectrum also undergoes changes between 25%

and 75% PTAK. PLE spectra of PFNG3, PFNG6, and PFNG9 CPECs at a 75% molar charge ratio are shown in **Figure 3.7B**. It is notable that in the linear Stern-Volmer regime, all three donor CPEs exhibit very similar EET efficiencies, as judged by the height of the peak at low excitation wavelengths, corresponding to absorption by the donor CPEs. However, for the conditions that fall outside of the linear regime, there is a clear difference in EET among the three PFNGX derivatives. The relative contribution from the low-wavelength peak decreases monotonically as a function of oligoethyleneglycol side chain length. Concomitantly, the region corresponding to direct PTAK excitation undergoes a subtle redshift. PLE spectra of PFNG3, PFNG6, and PFNG9 CPECs at a 50% molar charge ratio are shown in **Figure A1.3**.

3.4 Discussion

We found that the steady-state PL spectra and time-resolved PL decays for the three CPEs were quite similar. The vibronic ratios of the PL spectra are consistent with a highly extended backbone. The crude l_p estimates from SAXS data are similarly consistent with this interpretation. Interestingly, we found that l_p increased from PFNG3 to PFGN6, which suggests that the oEG length influences the polymer backbone extension in salt-free aqueous solution, consistent with the small redshift in OD. We also found that both q-dependence of D_{eff} and the SAXS intensity was qualitatively different from PFNG9 compared to the other two derivatives. We believe these observations point towards self-assembly of PFNG9, which challenges our assumption of no inter-chain interactions in SAXS analysis. The fact that the vibronic

ratio for PFNG9 is slightly larger than that of PFNG3 and PFNG6 suggests that the structure of the assembly is not that of a simple H-aggregate. The latter would be expected to show a substantially diminished I_{00}/I_{01} value.

Our original hypothesis was that the EET efficiency between an exciton-donor and an exciton-acceptor CPE would decrease with increasing oEG length. We reasoned that longer oEG chains would eventually hinder complexation between oppositely charged CPEs. It is intriguing that these oEG length differences did not in fact influence the EET efficiency at low acceptor CPE mole ratios, as the PLE spectra for all three CPEs were effectively identical, and the K_{SV} estimates were relatively similar. This has

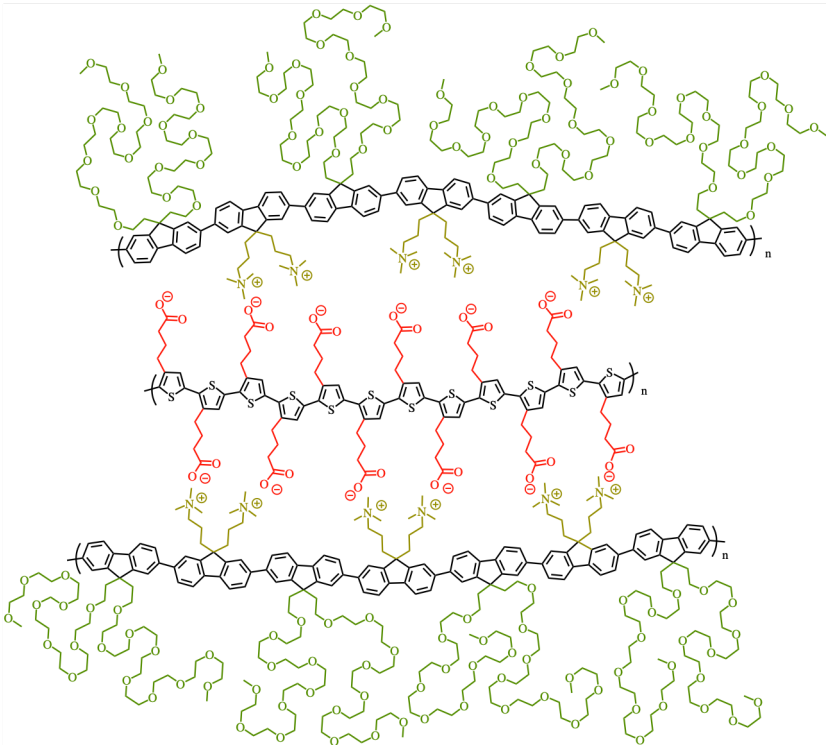

Figure 3.8 Cartoon of hypothesized inter-CPE complex structure with PFGN9 as the exciton donor and PTAK as the acceptor.

implications for the inter-chain structure that the donor/acceptor complex must assume, which is summarized in the postulated cartoon in **Figure 3.8**. It must be the case that PFNGX polymers arrange in the complex so as to point the oEG side chains away from the exciton acceptor for all three oEG lengths. This implies that the PFNGX backbone remains relatively straight in the inter-CPE complex despite the quite large, brush-like nonionic side chain size in PFNG9. Our initial expectation that this would induce substantial coiling of the exciton donor was proven incorrect.

Although the EET efficiency was independent of oEG length at low acceptor/donor charge mole ratios, at a charge mole ratio of 0.75, intriguing differences in both the Stern-Volmer plots and PLE spectra emerged. First, the β exponent from power-law fits to Stern-Volmer curves was largest for PFNG9. Second, the PTAK PLE spectrum for PFNG9 differed from that of PFNG6 in both the decrease in the low-wavelength peak amplitude corresponding to EET from PFNG9 to PTAK, along with a redshift in the long-wavelength (PTAK absorption) region.

Why did the Stern-Volmer plot diverge as [PTAK] was increased? What this corresponds to is the onset of phase separation, which we expect as the charge mole ratio between the cationic and anionic CPEs approaches unity. It is interesting that although all three donor CPEs behaved identically within CPECs at low acceptor mole fractions, differences emerged near the onset of phase separation. The fact that PFNG9 clearly distinguished itself implies that the oEG chains are non-innocent when the inter-CPE correlation length begins to diverge near the phase transition. At this point the

few-chain complex grows into a large and eventually macroscopic inter-chain network of proximal exciton donors and acceptors, thus forming a highly excitonically interconnected state. Based on the PLE and Stern-Volmer results, this in turn implies that we should expect significant differences in the behavior of the concentrated dense phases of these complexes as the polymer and salt concentration are increased.

3.5 Conclusion

In this work we synthesized a chemical series of exciton-donor CPEs with variable lengths of oEG side chains. The motivation behind this alternating co-polymer series was to make CPEs with functionalized fluorene monomers: one with pendant ionic side chains and one with polar nonionic side chains, for increased stability in high-ionic-strength solutions. For the 9EG side chain, we do in fact find remarkable stability in solutions with salt (LiBr, tetraethylammonium bromide) concentrations in the 1-5 M range. In the absence of oEG side chains, a similar fluorene-*alt*-phenylene polymer is highly unstable against phase separation in *isolated* solution. In salt-free solutions, we find that oEG length influences the polymer persistence length, with the longest oEG derivative evidently inducing self-assembly. However, when electrostatically coupled with an exciton-acceptor CPE, the EET efficiency was independent of oEG length on the exciton donor, which implies that even very large oEG side chains do not interfere with efficient exciton transfer.

A very intriguing finding is that the oEG length does influence both the apparent onset of phase separation and the structure of the inter-CPE complex near this phase

transition. The reason we are interested in increasing the stability of these synthesized exciton-donor CPEs in high-salt solution is our desire to form light-harvesting inter-CPE complex *fluids*. Such fluids can serve as precursors for hierarchical light-harvesting systems via a relatively simple thermodynamic pathway of associative phase separation. The fact that the oEG side chain influences this associative phase separation has intriguing implications for the tunability of the structure of and dynamics within these systems. Our current work is focusing on the phase behavior and exciton transfer within such CPE macrostates in the high ionic strength and high polymer concentration limits.

3.6 References

(1) Hollingsworth, W. R.; Segura, C.; Balderrama, J.; Lopez, N.; Schleissner, P.; Ayzner, A. L. Exciton Transfer and Emergent Excitonic States in Oppositely-Charged Conjugated Polyelectrolyte Complexes. *J Phys Chem B* 2016, *120* (31), 7767–7774. https://doi.org/10.1021/acs.jpcb.6b06533.

(2) Hollingsworth, W. R.; Magnanelli, T. J.; Segura, C.; Young, J. D.; Bragg, A. E.; Ayzner, A. L. Polyion Charge Ratio Determines Transition between Bright and Dark Excitons in Donor/Acceptor-Conjugated Polyelectrolyte Complexes. *J Phys Chem C* 2018, *122* (39), 22280–22293. https://doi.org/10.1021/acs.jpcc.8b06195.

(3) Hollingsworth, W. R.; Williams, V.; Ayzner, A. L. Semiconducting Eggs and Ladders: Understanding Exciton Landscape Formation in Aqueous Π-Conjugated Inter-Polyelectrolyte Complexes. *Macromolecules* 2020, *53* (7), 2724–2734. https://doi.org/10.1021/acs.macromol.0c00029.

(4) Johnston, A. R.; Perry, S. L.; Ayzner, A. L. Associative Phase Separation of Aqueous Π-Conjugated Polyelectrolytes Couples Photophysical and Mechanical Properties. *Chem Mater* 2021, *33* (4), 1116–1129. https://doi.org/10.1021/acs.chemmater.0c02424.

(5) Stetefeld, J.; McKenna, S. A.; Patel, T. R. Dynamic Light Scattering: A Practical Guide and Applications in Biomedical Sciences. *Biophysical Rev* 2016, *8* (4), 409–427. https://doi.org/10.1007/s12551-016-0218-6.

(6) Lakowicz, J. R. *Principles of Fluorescence Spectroscopy*; Springer, 2006, pp 18.

(7) Braslavsky, S. E.; Fron, E.; Rodríguez, H. B.; Román, E. S.; Scholes, G. D.; Schweitzer, G.; Valeur, B.; Wirz, J. Pitfalls and Limitations in the Practical Use of Förster's Theory of Resonance Energy Transfer. *Photochem Photobio S* 2008, *7* (12), 1444–1448. https://doi.org/10.1039/b810620g.

(8) Valandro, S. R.; Jagadesan, P.; Feng, F.; Schanze, K. Aggregation-Enhanced Two-Photon Absorption of Anionic Conjugated Polyelectrolytes. *J Phys Chem Lett* 2020, *11* (19), 8292–8296. https://doi.org/10.1021/acs.jpclett.0c02152.

(9) Wang, X.; Zardo, I.; Spirkoska, D.; Yazji, S.; Ng, K. W.; Ko, W. S.; Chang-Hasnain, C. J.; Finley, J. J.; Abstreiter, G. Valence Band Splitting in Wurtzite InGaAs Nanoneedles Studied by Photoluminescence Excitation Spectroscopy. *Acs Nano* 2014, *8* (11), 11440–11446. https://doi.org/10.1021/nn504512u.

Chapter 4

MORPHOLOGY CHARACTERIZATION

VIA X-RAY SCATTERING EXPERIMENTS

Acknowledgments

Sections 4.2.1- 4.2.4 were made possible with the use of samples that were prepared by other researchers, namely: Dr. Michael Roders, Dr. Aristide Gumyusenge, and Kartik Choudhary. Gregory M. Pitch collected GIXD measurements and performed the analysis of samples discussed in sections 4.2.1, 4.2.2, and 4.2.3. In sections 4.2.2 and 4.2.4, GMP performed analysis on GIXD images collected by Tim J. Dunn; a beamline scientist at Stanford Synchrotron Radiation Lightsource (*SSRL*). The principal investigators who supervised each project approved including these results in this dissertation.

4.1 Organic Photovoltaics

Traditionally, the most common organic photovoltaics (*OPVs*) have utilized conjugated polymer/fullerene blends which have been solution-processed to form bulk-heterojunction (*BHJ*) thin films.[1,2] The conjugated polymer has the role of an exciton-donor in thin film OPVs. Upon photo-excitation, the polymer generates an exciton, due to the high binding energies of ~ 0.5 eV.[3–5] The exciton participates in intra-chain and inter-chain migration until either the excited electron recombines with its bound hole in the ground-state, or the excited electron dissociates from its bound hole. This competitive process between geminate recombination and charge separation is influenced by the excited-state lifetime of the exciton.[1,2,6] Separation of the excited electron from its bound hole is initiated through interaction with an acceptor molecule; the energy of the acceptor molecule's LUMO must be lower than that of the donor.[6] Fullerene derivatives are the quintessential acceptor molecules due to having the appropriate energy levels to induce separation of charges in excitons, as well as having isotropic charge transport via their 3-dimensional geometry of frontier orbitals.[7]

BHJ architectures have highly-interpenetrating networks of donor-acceptor (*D-A*) phases with the necessary nanometer length scales to increase the efficiency of an organic solar cell.[1,2,6,8] This type of D-A architecture increases the probability that a generated exciton in the donor phase will migrate to a D-A interface during the exciton's lifetime and therefore increases the probability of generating separated charge

carriers. The interpenetrating network of D-A phases also provides a continuous pathway for free charge carriers to reach the electrodes.[1,2,6,8]

These soft-matter systems, which are spin-cast from D-A blend solutions, span a wide range of morphologies. The morphology of polymer/small-molecule BHJ thin films depends on many variables such as chemical structures of D-A, the concentration of D-A, solvent volatility, spin-coating conditions, additives, and post-processing conditions.[1,2,6,8] Since the morphology of the BHJ architecture influences the efficiency of the OPV, interrogating the morphology of polymer thin films in terms of the length scales of D-A phase separation, is of utmost importance.

4.2 Synchrotron Based Grazing Incidence X-ray Diffraction

Grazing incidence X-ray diffraction (*GIXD*) is a technique that probes the length scales of molecular packing and crystallite orientations of organic molecules in the solid-state, specifically thin films formed on a substrate. A large flux of energy is needed to generate enough scattering in samples with low-Z atoms like C, N, and O. Therefore, synchrotron radiation light sources are often used to generate X-ray scattering data for thin film organics.[9] A highly collimated beam of X-rays is used to strike the sample at an extremely shallow angle. To investigate the surface of the sample and limit scattering contributions from the substrate, an angle above the critical angle (α_c) of the organic material and below the α_C of the silicon or glass substrate is required. This technical aspect of GIXD arises because X-rays cannot enter a sample if

the incident angle is below the α_C of the material. Moreover, this requirement arises because the complex refractive index (n) is slightly below the value of 1. The equation for the complex index of refraction is shown in Equation 4.1,

$$n = 1 - \delta + i\beta \tag{4.1}$$

where δ is the real part of the complex index of refraction, and β is the complex part of the complex index of refraction, accounting for absorption.[9]

Scattering of light from particles can occur either as Thompson scattering (elastic) or Compton scattering (inelastic).[10] Inelastic scattering occurs when an incoming photon collides with an electron and transfers some of its energy to the electron. This type of scattering does not provide structural information because the scattered waves are incoherent. In contrast, elastic scattering does provide structural information since the scattered photons produce coherent waves that can interact constructively and destructively.[10] These interactions encode structural details via bright and dark spots on a detector.

GIXD provides information on the angstrom length scale and helps determine the orientation of crystallite populations present in thin films. Amorphous samples do not have defined repeating distances and will scatter X-rays over a wide range of reciprocal space. Crystalline or semi-crystalline samples that have some long range order on the angstrom length scale will provide bright spots on the 2D detector in reciprocal space. These bright spots are known as Bragg reflections and arise from the constructive

interference of scattered X-rays off of crystalline planes. Equation 4.2 makes explicit the relationship between reciprocal space and real space,[9]

$$Q = \frac{2\pi}{d} \tag{4.2}$$

where, d represents the real-space distance in units of Å, and Q is the scattering vector length. The scattering vector can be described further as the difference between the incoming and outgoing wavevectors of X-rays. It is typical to express the scattering data as a function of scattering vector Q, which has a magnitude shown in Equation 4.3.[9]

$$Q = \left[\frac{4\pi}{\lambda}\right] \sin\theta \tag{4.3}$$

The incident X-ray wavelength is λ, and θ is half of the value of the scattering angle.[9]

GIXD images taken of semi-crystalline polymers produce diffraction images with peaks that correspond to lamellar distances between side chains, and π-stacking distances between conjugated backbones. A cartoon of semi-crystalline polymer chains is shown in **Figure 4.1**. Scattering from a sample is detected on a 2-dimensional *area* detector; the vertical axis is labeled Q_z and the horizontal axis is labeled Q_{xy}. The outgoing scattering vectors with a component perpendicular to the substrate will be detected along the Q_Z axis, and outgoing scattering vectors with a component parallel to the substrate will be detected along the Q_{xy} axis. The in-plane scattering vector, will be that of a true crystalline powder if the sample is randomly oriented in the XY-plane.

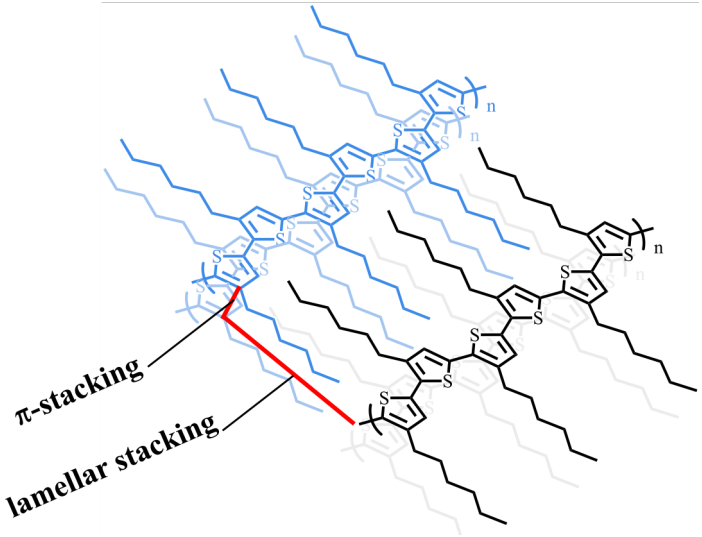

Figure 4.1 Cartoon of P3HT polymer chains: π-stacking between conjugated backbones and lamellar stacking of hexyl side chains.

However, when the preferential alignment of polymer crystallites exist, then a difference in the in-plane scattering vector is seen for a sample that has been rotated in-plane by 90°.[9] The direction of the scattering vector is related to the orientation of the molecule in the sample, GIXD measurements are also sensitive to the distance between crystallographic planes in a sample, and therefore, this technique is also used to elucidate the angstrom length scales in a sample.

4.2.1 Influence of Molecular Excluded Volume and Connectivity on the Nanoscale Morphology of Conjugated Polymer/Small Molecule Blends

Besides the choice of donor and acceptor, there is a limited number of parameters that can be varied to influence the morphology of the resulting BHJ. Previous

investigations of the parameter space for polymer/fullerene BHJ OPVs produced devices with similarly disappointing power conversion efficiencies (*PCE*).[6,11] To substantially increase the PCE, either the donor or acceptor should be changed. A major consideration when trying to find an acceptor molecule to replace the fullerene would be how the molecular geometry affects the resulting charge transfer and morphology of the blend.[8]

This work investigates the influence of relatively small differences within a series of small molecule acceptors on the morphology of the resulting polymer/small molecule blends via X-ray scattering experiments. A series of nonplanar conjugated small molecule acceptors have been systematically altered to determine how the subtle molecular changes affect the resulting morphology on the angstrom scale.[8] GIXD measurements probe the influence of the chemical structure of nonplanar conjugated small molecule acceptors has on the texture and orientation distribution of the polymer crystallites in the thin film.[9] These experiments were carried out at SSRL at Beamline 11.3.

In this work, a small-molecule chemical series was used where each spirobifluorene (*Sp*) core was modified by the number and placement of peripheral side groups. Spiro-bifluorene provides the small molecule with a pseudo spherical 3-dimensional molecular geometry, to attain an acceptor with a space-filling arrangement similar to that of fluorene, the quintessential acceptor molecule.[8] The chemical series is comprised of 2,2',7,7'-tetrakis[*N*,*N*-di(4-methoxy-phenyl)amino]-9,9'-spirobifluorene

(*Sp-M*), 2,7-bis[*N*,*N*-bis(4-methoxy-phenyl)-amino]-9,9'-spirobifluorene (*Sp-Z*), and 2,2'-bis[*N*,*N*-bis(4-methoxyphenyl) amino]-9,9-spirobifluorene (*Sp-E*). These small molecule acceptors have similar types of molecular interactions and are weakly ordered in thin films.[12] The conjugated polymer hosts used for this study were poly(3-hexylthiophene) (P3HT) and poly[4,8-bis(5-(2-ethylhexyl)thiophen-2-yl)benzo[1,2-b;4,5-b']dithiophene-2,6-diyl-alt-(4-(2-ethylhexyl)-3-fluorothieno[3,4-b]thiophene-)-2-carboxylate-2,6-diyl)] (PTB7). Each of these conjugated polymers is semi-crystalline albeit having different chemical structures.[6] The small-molecule series and their host conjugated polymers are shown in **Figure 4.2**.

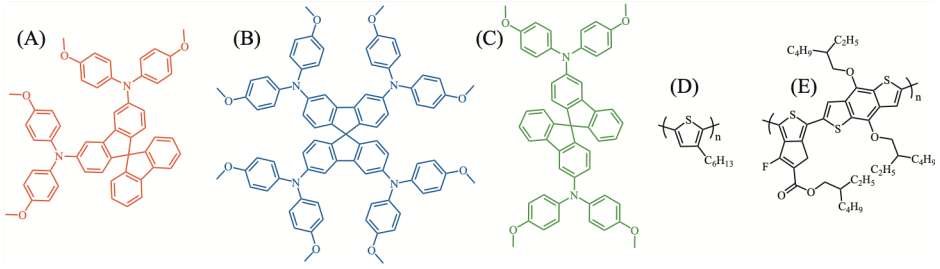

Figure 4.2 Structures of (A) Sp-Z, (B) Sp-M, (C) Sp-E, (D) P3HT, (E) PTB7.

GIXD images were collected and analyzed to determine the influence that each small molecule has on the texture of the thin film. Briefly, the X-ray beam skims the surface of the thin film and is scattered by the electrons in the sample. The observable in this measurement is the scattering vector Q, which is quantified by a detector at a distance away from the sample.[9,10] The diffraction image is then analyzed for the spatial arrangement of the scattering vector so that the real space distances attributed to

morphological features can be determined.[9] Additionally, the placement of the scattering vector provides information on the orientation distribution of the polymer crystallites, with inherent implications on an OPVs PCE.

GIXD images of neat P3HT and PTB7 have Bragg reflections associated with lattice planes for lamellar distances and π-stacking distances between polymer chains, shown in **Figure 4.3**. In the images, these distances are detected in reciprocal space and were converted to real space distances via Equation 4.2.[9,10] For P3HT, the (100) Bragg

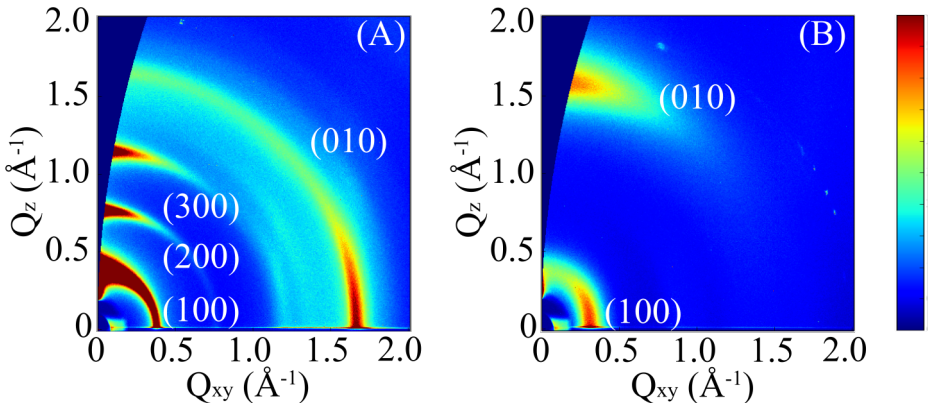

Figure 4.3 (A) GIXD image for neat P3HT film. (B) GIXD image for neat PTB7 film.

reflection was located at a Q value of 0.38 $Å^{-1}$, which is attributed to a real space lamellar distance between side chains of 16.5 Å. The (010) Bragg reflection was located at a Q value of approximately 1.67 $Å^{-1}$, which is attributed to a real space π-stacking distance of 3.76 Å. Additionally, higher-order Bragg reflections associated with

lamellar stacking were also seen, indicating P3HT is a highly semi-crystalline polymer.[10] The π-stacking peak for neat P3HT is located close to the Q_{xy} axis, indicating that the polymer crystallites preferentially aligned edge-on to the substrate. For PTB7, the (100) Bragg reflection was found to have a Q value of 0.315 $Å^{-1}$, which is attributed to a real space lamellar distance between side chains of 19.9 Å. The (010) Bragg reflection has a Q value of approximately 1.58 $Å^{-1}$, attributed to a real space π-stacking distance of 3.98 Å. The opposite orientation was found to be true for the neat PTB7 samples, where the crystallites aligned face-on to the substrate, as indicated by the (010) Bragg reflection near the Q_z axis.[10]

Depending on which small-molecule acceptor was incorporated into the blend, the π-stacking distance and the lamellar distances were not found to change dramatically. A more detailed understanding of the polymer/small molecule thin film texture was investigated by the orientation distribution function (*ODF*) of the blends.[10] P3HT blends have a slightly more narrow edge-on component compared to that of the neat P3HT film, while the face-on fraction of crystallite population for P3HT blend samples are slightly larger than for the neat film. This means that of the amount of total crystalline material in each sample, blend films have a higher propensity to be found with a face-on orientation. The ODF plots for neat polymer and polymer/small molecule blends are shown in **Figure 4.4**.

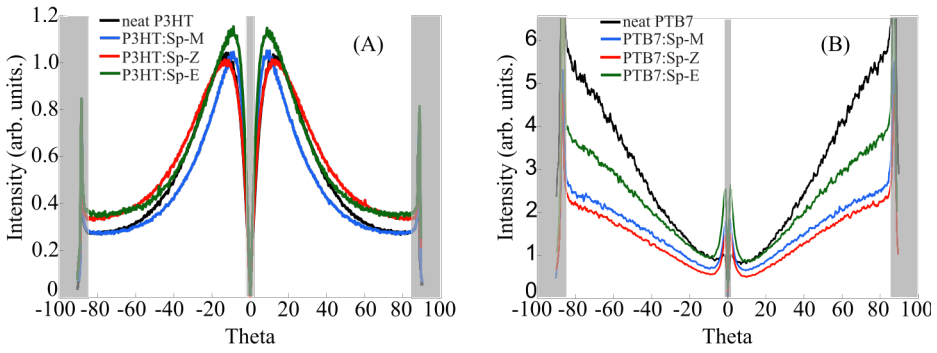

Figure 4.4 (A) ODF of neat P3HT and P3HT blend films (B) ODF of neat

In contrast, the neat film of PTB7 has a higher propensity to exist with a face-on orientation than their respective blend films. These qualitative results were quantitatively analyzed for the determination of face-on to edge-on ratios. For each sample, the area under the curve of the ODF was integrated from 45-85° (face-on) and 5-45° (edge-on). The ODF also includes a sin (θ) correction factor to account for the crystalline density contributing to a given solid angle as a function of polar angle.[10] The ODF was calculated from the ratio of these two integrals and is shown in Equation 4.4.

$$R = \int_{45}^{85} \text{ODF}\, d\theta \Big/ \int_{5}^{45} \text{ODF}\, d\theta \qquad (4.4)$$

The results from these calculations are tabulated in **Figure 4.5**.

	P3HT Face-on : Edge-on Ratio	PTB7 Face-on : Edge-on Ratio
Neat Film	0.13	1.22
Blend with Sp-M	0.13	0.84
Blend with Sp-Z	0.16	0.92
Blend with Sp-E	0.15	0.92

Figure 4.5 Face-on : Edge-on ratios for neat polymers and polymer/small molecule blends.

4.2.2 Isoindigo-Based Binary Polymer Blends for Solution-Processing of Semiconducting Nanofiber Networks

In this study, nanofibrous thin films were formed by blending an isoindigo-based semiconducting polymer with conjugation break spacers and a crystalline tie-polymer. These conditions provide thin films with low elastic moduli, low glass transition, excellent charge transport, and high crack-on-set strain. The crystalline tie-polymer is present to aid in the nucleation of nanofibers and ensure that the electronic properties of the material are maintained, while the matrix polymer aids in increasing the processability and flexibility of the thin film.[13–15] Traditionally, insulating matrix polymers serve as a blending medium for guest species. In electronics, the guest species could be a conjugated polymer or crystalline small molecule. One way to possibly

increase the efficiency of an electronic device would be to increase the fraction of the active component in the device.[13–15]

By using a conjugated polymer with deliberate conjugation break spacers as the matrix blended with a structurally similar crystalline tie-polymer, flexible thin films with electronic properties are formed. The chemical structures of the isoindigo-based crystalline tie-polymer (*P1*) and the matrix polymer (*C3*) are shown in **Figure 4.6**.

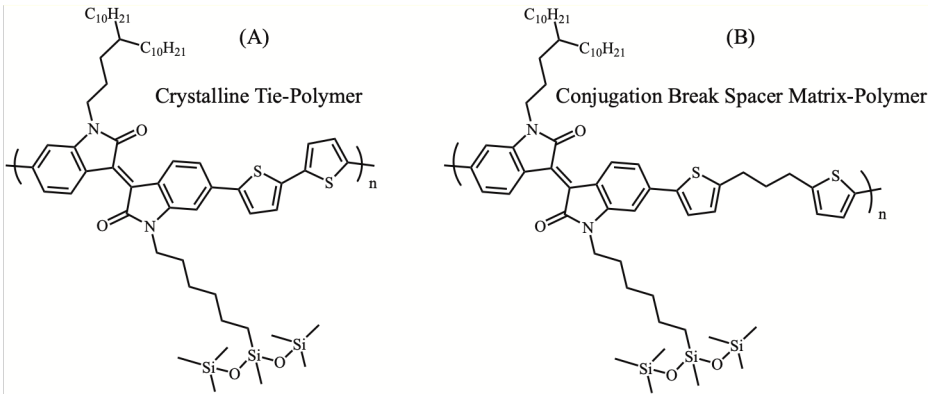

Figure 4.6 Structures of (A) Isoindigo crystalline tie-polymer (B) Isoindigo conjugation break spacer matrix-polymer.

The isoindigo matrix-polymer and the isoindigo crystalline tie-polymer were blended in ratios of 100:0, 90:10, 50:50, 10:90, and 0:100, and the texture of the resulting thin films were investigated by GIXD experiments at SSRL (Beamline 11.3). **Figure 4.7** shows the resulting GIXD images.

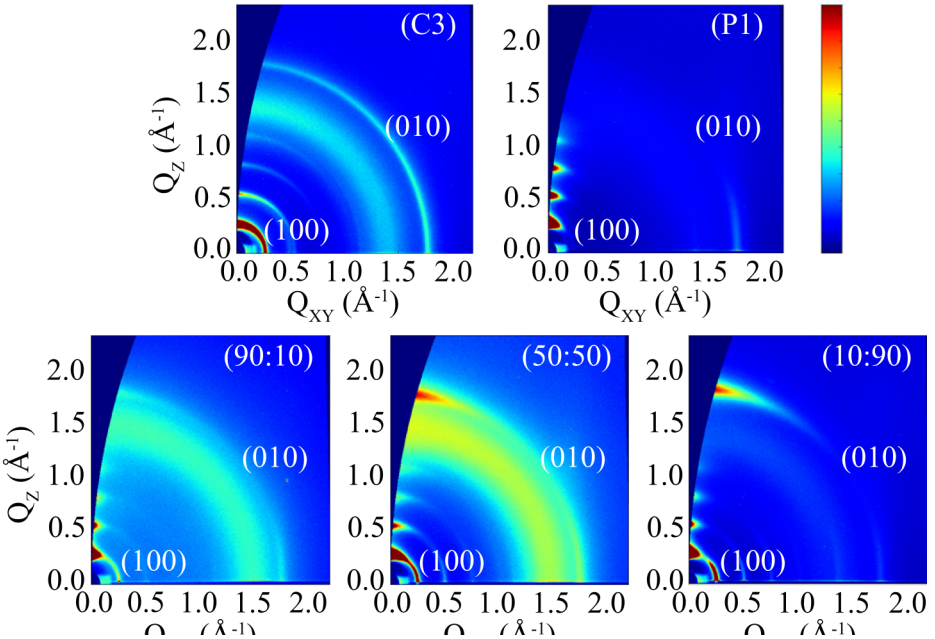

Figure 4.7 GIXD images of (P1)Isoindigo crystalline tie-polymer, (C3) Isoindigo conjugation break spacer matrix-polymer, (90:10) Matrix-Tie Blend, (50:50) Matrix-Tie Blend, (10:90) Matrix-Tie Blend.

The (100) Bragg reflections for each neat polymer thin film have slightly different peak positions but differ widely in their ODFs. The (100) Bragg reflection for the matrix polymer shows a bimodal crystallite orientation distribution, and since the reflections corresponding to lamellar and π-stacking are anti-correlated, the (010) Bragg reflection also shows a bimodal crystallite orientation distribution.[10] The texture of the matrix-polymer is in stark contrast to that of the crystalline tie polymer, where the texture of the crystalline tie-polymer is heavily edge-on. This is seen with the (100) Bragg reflection being located near the Q_z axis.[10]

The progression of the thin films texture upon blending the matrix-polymer with the crystalline tie-polymer initially brings about a change from the bimodal crystallite orientation distribution in the pure matrix-polymer thin film to a more edge-on orientation in the 90:10 blend. This is then followed by a more isotropic crystallite orientation distribution for the 50:50 blend. Compared with that of the pure films, an increase in the crystallinity of the thin film was also observed in the 50:50 blend. This is true only if the sample volume probed by the X-ray beam was the same across all thin films.[10] Furthermore, since the beam footprint and the incidence angle did not change between measurements of each sample, and because the processing conditions remained constant among the samples, the thickness of each thin film should also be very similar. This strongly suggests that the crystallinity of the 50:50 blend is higher than for the other films.

The texture of the 10:90 film becomes even more bimodal than that of the 50:50 blend with the addition of more crystalline tie-polymer, albeit the crystallinity seemingly diminishes, which was gleaned from the lower intensity of the broad (010) Bragg reflection. This broad halo seen most notably in the 50:50 blend implies that the nanofibrous structures are isotropic; since a broad halo indicates that the orientation of crystallites exist at all angles with respect to the substrate.[9,10]

4.2.3 Semiconducting Polymer Blends that Exhibit Stable Charge Transport at High Temperatures

Organic semi-conductors usually display charge-transport mechanisms that are thermally activated due to the inherent nature of the distribution of trap states. Charge carriers will thermally hop between electronic states until they interact strongly with a defect site.[16,17] Up until a point, excess thermal energy often helps overcome the trapping of charge carriers.[18] However, extreme increases in temperature disrupt the integrity of the material by forming unstable morphologies. Attempts to create thermally robust morphologies via thermal annealing have not solved the problem of temperature-dependent charge-carrier mobilities.[19]

The way to overcome the temperature-dependent mobility of charge carriers is to form a system where morphological features such as π-stacking distances are retained at high temperatures. This allows the thin film to retain ambient charge-carrier mobilities at elevated temperatures. Logistically, this occurs through the processing of a semicrystalline conjugated polymer with an insulating polymer with high glass-transition temperatures (T_g).[20] Conceptually, the insulating polymer locks in the morphology of the semicrystalline conjugated polymer, with concomitant retention of the electronic properties.

In this work, poly(*N*-vinyl carbazole) (*PVK*) was used as a high T_g insulating polymer and diketopyrrolopyrrole-thiophene (*DPP-T; P1*) was used as the semicrystalline conjugated polymer to provide high charge-carrier mobilities. The chemical structures of DPP-T and PVK are shown in **Figure 4.8**. The 55- 65 wt. % PVK blends were solution-processed via spin-coating, producing interpenetrating

channels between the conjugated polymer and DPP-T. These conditions formed materials that retained device performance at temperatures up to 220℃, where hole mobilities as high as 2.5 $cm^2/V{\cdot}s$ were measured.[20] To investigate the molecular packing of the blended films, temperature-dependent GIXD experiments were carried out at SSRL (Beamline 11.3).

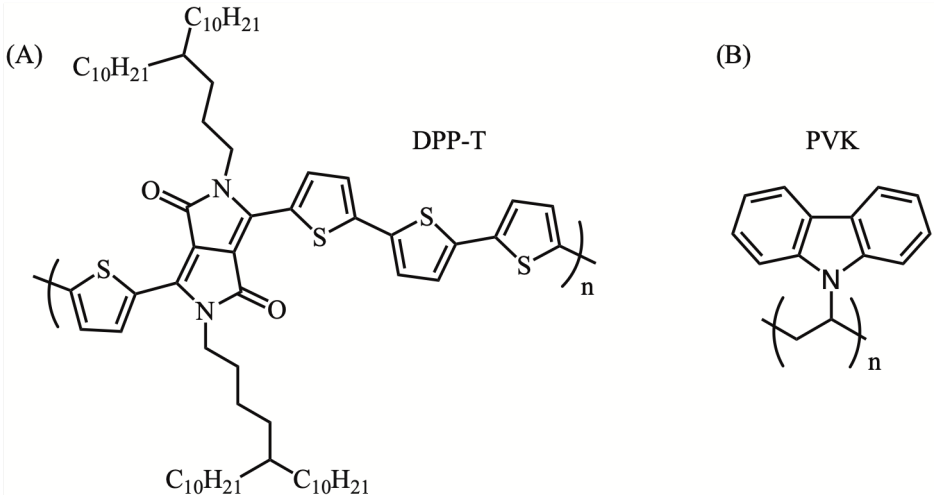

Figure 4.8 Structures of (A) Semicrystalline conjugated polymer (DPP-T), (B) Insulating polymer (PVK).

Temperature-dependent GIXD experiments were carried out on a neat DPP-T film, a neat PVK film, and a 60 wt. % PVK blended film. Relative to neat DPP-T at ambient temperature, the π-stacking distance of the 60 wt. % PVK blended film contracted from 3.70 Å to 3.64 Å. However, the π-stacking distance in both the pure DPP-T film and the 60 wt. % PVK film expanded with added thermal energy to distances of 3.79 Å and

3.73 Å, respectively. The relative similarity in the π-stacking distances in the neat DPP-T film at ambient conditions and the 60 wt. % PVK film at elevated temperatures explains the high hole mobilities detected in the blended PVK film over a range of temperatures. In contrast, upon blending DPP-T with 60 wt. % PVK, expansion of the lamellar packing distance is seen at room temperature and stays expanded at higher temperature. This has little bearing on the charge-carrier mobility, since the lamellar distance describes the distance between insulating side chains. Representative GIXD images of DPP-T, PVK, and the 60 wt. % PVK blended films at room temperature and 200℃ are shown in **Figure 4.9**.

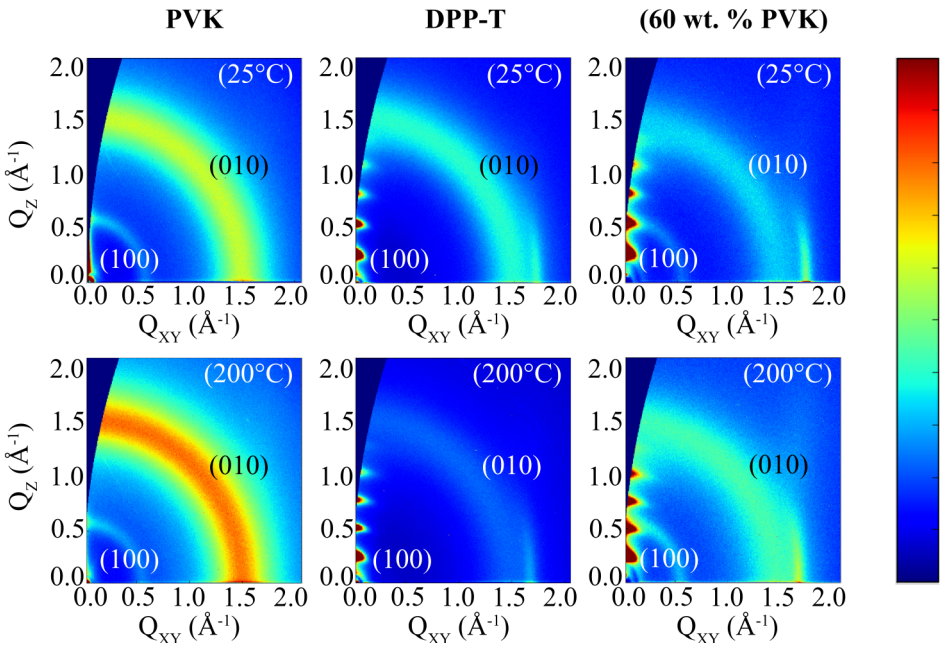

Figure 4.9 GIXD images of (PVK) at 25℃, (PVK) 200℃, (DPP-T) at 25℃, (DPP-T) 200℃, (60 wt. % PVK) at 25℃, (60 wt. % PVK) 200℃.

The neat PVK film shows an isotropic π-stacking arrangement of the carbazole side chains. Additionally, the (010) Bragg reflection is very broad, indicative of the wide variety of π-stacking distances in the thin film. The orientation distribution of crystallites for the thin films of DPP-T show an edge-on orientation which is invariant with increasing thermal energy. This was observed in the GIXD image as a (100) Bragg reflection located near the Q_z axis.[10] Moreover, the 60 wt. % PVK blend thin film also shows invariant edge-on orientation with increasing temperature, with the (100) Bragg reflection located near the Q_z axis.[10] The main takeaway is that even though the π-stacking distance becomes smaller for the 60 wt. % PVK blend compared with neat DPP-T, at elevated temperatures, there seems to be a negligible change in a film's ODF.

4.2.4 Comparison of the Mechanical Properties of a Conjugated Polymer Deposited Using Spin Coating, Interfacial Spreading, Solution Shearing, and Spray Coating

Applications that utilize semiconducting polymers as their active component are often thin films prepared by spin-casting from solution. However advantageous an organic material may be for an application, widespread adoption of a functional form needs to be amenable to large scale mass production. Spin-coating works well with small substrates; it is no surprise that spin-coating has been a widely adopted research technique. Spin-coating electronic devices is an easy way to investigate the fundamental chemistry of organic materials, since many small-scale devices that encompass the parameter space can be made and studied. The issue is the potential

relevance of these fundamental studies have for real-world applications. It is imperative to take a step back, and approach the organic electronic space with a new frame of reference. The mechanical properties of thin films of poly(2-heptylthiophene) (*P3HpT*) formed from scalable deposition processes were thus investigated. The chemical structure of P3HpT is shown in **Figure 4.10**.

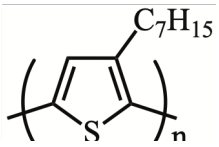

Figure 4.10 Structures of P3HpT

The mechanical properties and thin film morphologies of the following deposition techniques were compared in this study. Interfacial spreading is a technique where a polymer solution is drop-cast onto a surface of a liquid. The formed film can be transferred to a substrate via a stamping process, and layer-by-layer assemblies can be formed from sequential stamping.[21,22] Solution shearing, also known as doctor-blading, is a process where a blade is used to coat a solute onto a substrate. This process creates a thin film with an aligned orientation along the direction of coating.[23–25] Spray coating is a process in which a solution is atomized into droplets to coat a substrate.[26] This creates thin films with similar hole mobilities to that of thin films deposited by spin-coating, although the films formed from spray-coating are rougher.[27,28] Spin-coated films are formed by drop-casting solutions onto a substrate and then spinning the

substrate to remove excess organic material. This facilitates the evaporation of the solvent, solidifying the organic material into a thin film.[6,29]

Since the mechanical properties of a polymer thin film depend on the molecular structure and the solid-state morphology, the morphologies of three scalable deposition processes were herein investigated. GIXD experiments were carried out to provide insight into the morphology of thin films deposited from solutions via spreading, solution shearing, and spray coating methods. GIXD images for each of the four deposition techniques are shown in **Figure 4.11**.

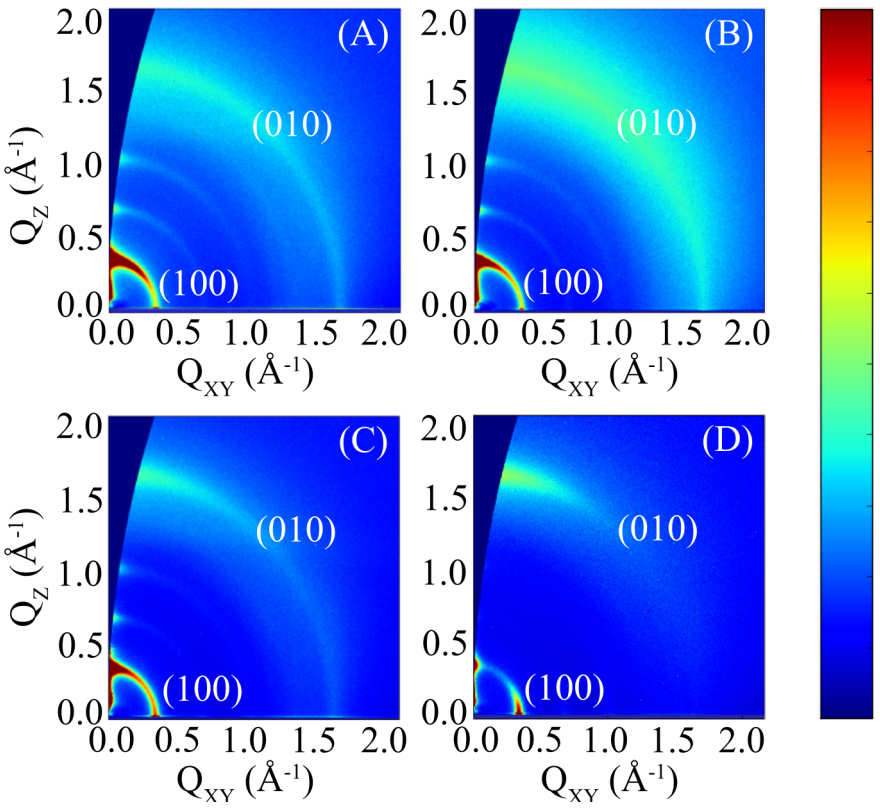

Figure 4.11 GIXD images of P3HpT (A) spin coated, (B) spread, (C) shear, (D) spray coated.

The GIXD images for all of the deposition techniques show very similar π-stacking distances of ~ 3.93 Å, which were determined from a broad (010) Bragg reflection located at a Q_z value of ~1.6 $Å^{-1}$.[9,10] The (010) Bragg reflections for spin-coated, interfacial spread, solution shear, and spray-coated were found to have Q values of 0.352 $Å^{-1}$, 0.349 $Å^{-1}$, 0.349 $Å^{-1}$, and 0.343 $Å^{-1}$, respectively. These values correlate with real space distances of 17.85 Å, 18.00 Å, 18.00 Å, and 18.32 Å, respectively. The most impactful information gleaned from these GIXD images came from the investigation of the film's texture via an ODF, which is shown in **Figure 4.12**.

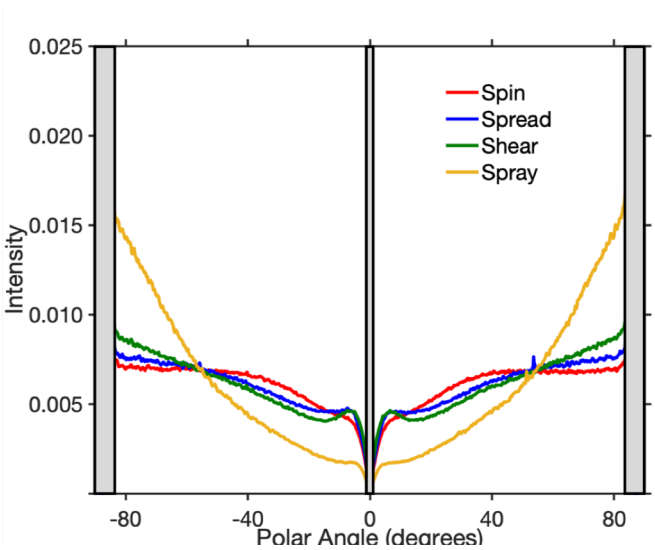

Figure 4.12 P3HpT ODF for spin coated, spread, shear, and spray coated deposition techniques.

As seen in the ODF of the thin films formed from the four deposition techniques, the outlier was the spray coated film. The ODF of the spray-coated film describes a

thin film texture that is highly face-on to the substrate.[9,10] Whereas, thin films deposited from interfacial spreading and solution shearing adopt a mostly face-orientation, although have edge-on character as well. The texture of the spin-coated films is the most isotropic of the four deposition methods, with a crystallite orientation distribution spanning a wide range of θ.[9,10]

4.3 Synchrotron Based Resonant Elastic X-ray Scattering Experiments

In resonant elastic X-ray scattering (*REXS*), the absorption edge of an element in the sample is leveraged to create additional scattering contrast. GIXD is different from REXS in multiple ways; the starkest difference is that the X-rays in REXS are much less energetic, resulting in interactions with core electrons. Each element requires X-rays of different energies to become resonant with its respective K-edge. This condition provides an increase in absorption of X-rays and leads to an increase in anomalous scattering. This technique is not only sensitive to the identity of the element but is also sensitive to the bonding environment around the element. These energies associated with an element's K-edge are determined by carrying out near edge X-ray absorption fine structure (*NEXAFS*) measurements.

The complex index of refraction has been mathematically described earlier with Equation 4.1. However, the dispersive and absorptive terms are also dependent on the energy of the incoming photon. Both δ and β are related to the complex scattering factor which is shown in Equations 4.5 and 4.6.[30,31]

$$f = f_1 - if_2 \quad (4.5)$$

$$f = f_0 - \Delta f' + i\Delta f'' \quad (4.6)$$

In the small-angle or long-wavelength limit, Equation 4.7 holds,

$$\delta - i\beta = \alpha\lambda^2(f_1 - if_2) \quad (4.7)$$

where $\alpha = n_a r_e/2\pi$, n_a equals the number density of atoms in the sample, and r_e equals the classical radius of an electron.[32] The practical result is that near the absorption edge, the values of δ and β as a function of photon energy change rapidly, and the contrast and scattering strength are determined by $\Delta\delta^2 + \Delta\beta^2$.[30,31]

Logistically, this experiment is conducted at a specialized beamline at a synchrotron facility. The sample is arranged with a transmission geometry, and the sample-detector distance is set to achieve values of the scattering vector, such that the real space distances are of order 10-100 nm.[30,31]

4.3.1 Evolution of Percolation Network in Polymer/ Small-Molecule Bulk-Heterojunction Organic Solar Cells via Resonant Elastic X-ray Scattering

The pertinent length scale for efficient exciton diffusion and dissociation is on the order of tens of nanometers. REXS is an X-ray scattering technique that has access to this length scale and leverages high powered, tunable soft energy X-rays from the advanced light source (*ALS*) at the Lawrence-Berkley national lab (*LBNL*), Beamline

11.01.2.[30] The high powered X-ray source is needed to provide enough scattering contrast from low Z materials, while the soft energy of the synchrotron X-rays allows for resonant scattering to occur when tuned over an elemental absorption edge.[30,31]

REXS was utilized to investigate the scattering contrast from a small molecule within a conjugated polymer host and therefore provides insight into the microstructure of the small molecule only. The sensitivity of this technique arises from choosing an energy resonant with the K-edge of an element only present in one component of the thin film. Three small molecules were each blended with two different semicrystalline conjugated polymers in order to investigate the nanometer length scales of small molecule phase separation present in the thin film.[30,31] To observe the evolution of the small-molecules phase separation, each small molecule was blended with the host polymer at two molar concentrations.

Three small molecules with distinct chemical structures were utilized in this study, a perylene diimide dimer (*dPDI*), [6,6]-phenyl-*C*71-butyric acid methyl ester (*$PC_{70}BM$*), and 3,9-bis(2-methylene-(3-(1,1-dicyanomethylene)-indanone))-5,5,11,11-tetrakis(4-hexylphenyl)-dithieno[2,3-d:2',3'-d']-s-indaceno[1,2-b:5,6-b']dithiophene (*ITIC*). Each of these small molecule acceptors has different molecular geometries and should pack differently into the same conjugated polymer host.[8] The chemical structures of these small molecules and the two semicrystalline conjugated polymers are shown in **Figure 4.13**.

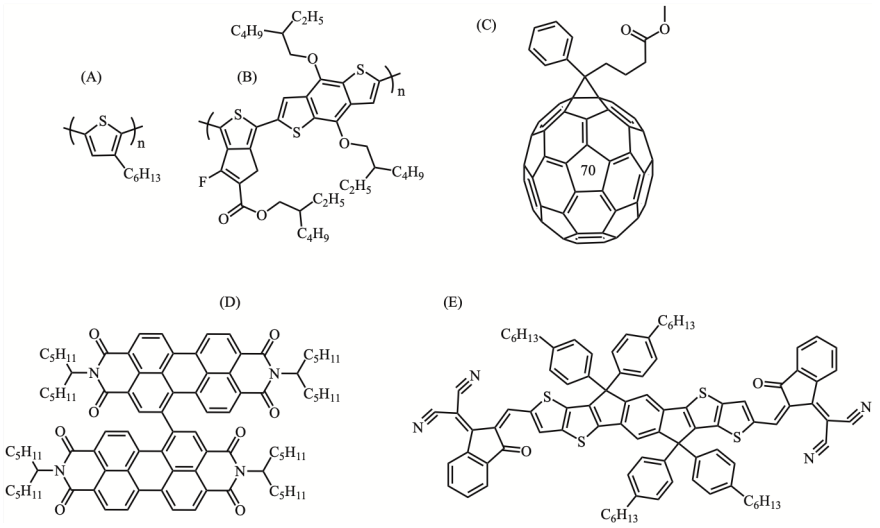

Figure 4.13 Chemical Structures of (A) P3HT, (B) PTB7, (C) $PC_{70}BM$, (D) dPDI, and (E) ITIC.

NEXAFS spectroscopic measurements were carried out on neat films of each component to identify the appropriate energies to utilize.[30,31] NEXAFS spectra were collected for each component at energies associated with exciting a carbon 1s electron into an unoccupied orbital (K-edge) and a NEXAFS spectrum was also collected for ITIC at energies associated with exciting a nitrogen 1s electron into an unoccupied orbital (K-edge).[30,31] These NEXAFS spectra are shown in **Figure 4.14**. The main determining factor for choosing a resonant energy to scatter at is to find a transition in one component of the thin film that is absent or very weak in another component present in the thin film blend. This became extremely straightforward when choosing an energy resonant with a nitrogen K-edge transition since the host polymer did not contain any nitrogen atoms. However, choosing the correct carbon energy that is

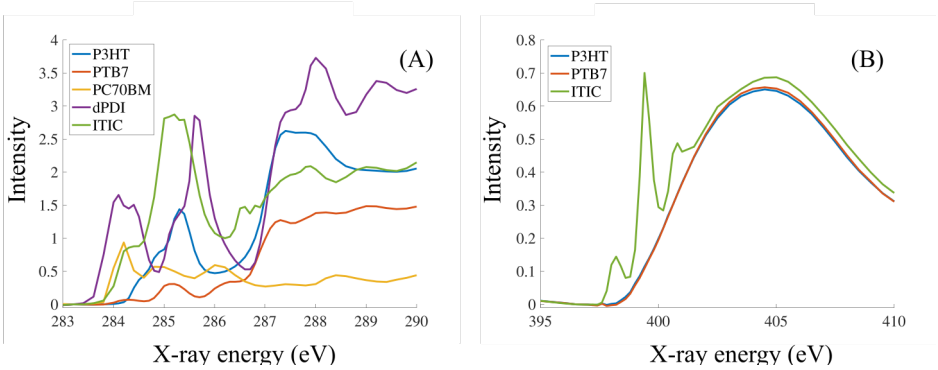

Figure 4.14 NEXAFS spectra of (A) P3HT, PTB7, $PC_{70}BM$, dPDI, and ITIC at the carbon K-edge, along with (B) P3HT, PTB7, and ITIC at the nitrogen K-edge.

particularly intense in a small molecule acceptor and not in the host polymer was more difficult.

REXS data was collected at four positions on the thin film to acquire representative data of the morphology of the material. This was done for each sample at close (50 mm) and far detector (150 mm) distances to access a wider range of scattering vector Q, and therefore a wider range of real space length scales. The acquired REXS data for P3HT:$PC_{70}BM$ at mole ratios of 1:0.5 and 1:1, along with REXS data for PTB7:$PC_{70}BM$ at mole ratios of 1:0.75 and 1:1.5 are shown in **Figure 4.15**.

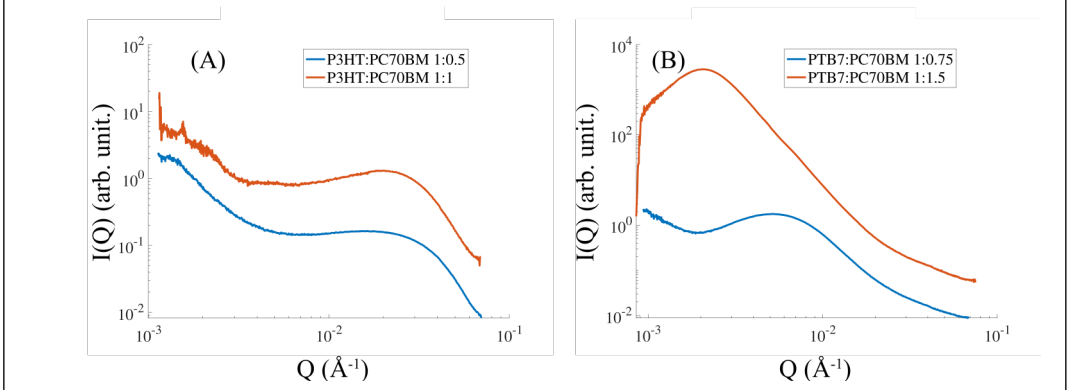

Figure 4.15 REXS at 284.2 eV (Carbon K-edge) stitched from close and far detector distances for (A) P3HT:$PC_{70}BM$ blends, and (B) PTB7:$PC_{70}BM$ blends.

The resonantly enhanced scattering data for each polymer: small molecule thin film blend shows the evolution of the small molecule percolation network with increasing small molecule mole fraction. Panel A of **Figure 4.15** shows that with increasing mole fraction of $PC_{70}BM$ in P3HT from 0.5 to 1, a feature located at a Q value of 0.0188 $Å^{-1}$ grows in intensity, and can be roughly quantified as a length scale of phase separation of 33.4 nm. A more interesting resonantly enhanced scattering signature can be seen in panel B, whereupon increasing the mole fraction of $PC_{70}BM$ in PTB7 from 0.75 to 1.5, a feature located at a Q value of 0.0052 $Å^{-1}$, which is representative of phase separation with a length scale of 120.8 nm, shifts to a smaller Q value of 0.0021 $Å^{-1}$. This new feature has a representative length scale that is more than two times larger and is quantified as 299.2 nm. Upon increasing the mole fraction of the small molecule

acceptor in both blends, P3HT is resistant to large-scale phase separation of $PC_{70}BM$, whereas PTB7 allows for more self-association of $PC_{70}BM$.

The reduced REXS data for P3HT:dPDI at mole ratios of 1:0.5 and 1:1, along with REXS data for PTB7:dPDI at mole ratios of 1:0.75 and 1:1.5 are shown in **Figure 4.16**.

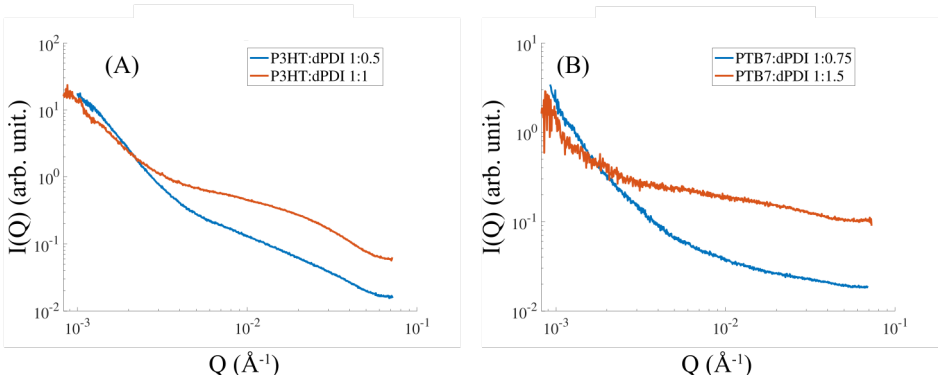

Figure 4.16 REXS at 285.7 eV (Carbon K-edge) stitched from close and far detector distances for (A) P3HT:dPDI blends, and (B) PTB7:dPDI blends.

Both panels A and B show weak scattering with features that are not as pronounced as the ones observed in **Figure 4.15**. Regardless, upon increasing the mole fraction of dPDI in the P3HT thin film, a more prominent plateau takes form. The Q value for the increase in negative slope is approximately 0.0207 $Å^{-1}$ and correlates with a length scale of phase separation of approximately 30.4 nm. Panel B shows that upon increasing the mole fraction of dPDI in PTB7 from 0.75 to 1.5, another plateau is discernible, however the length scale for phase separation is not readily determined. In comparison to the evolution of the percolation network found in panel B of **Figure**

4.15, the features in panel B of **Figure 4.16** appear at a larger Q value. Indicating that dPDI was not able to form as extended phase-separated regions as $PC_{70}BM$ was able to form, in the same host matrix.

REXS data for P3HT: ITIC at mole ratios of 1:0.5 and 1:1, and REXS data for PTB7: ITIC at mole ratios of 1:0.75 and 1:1.5 are shown in **Figure 4.17**.

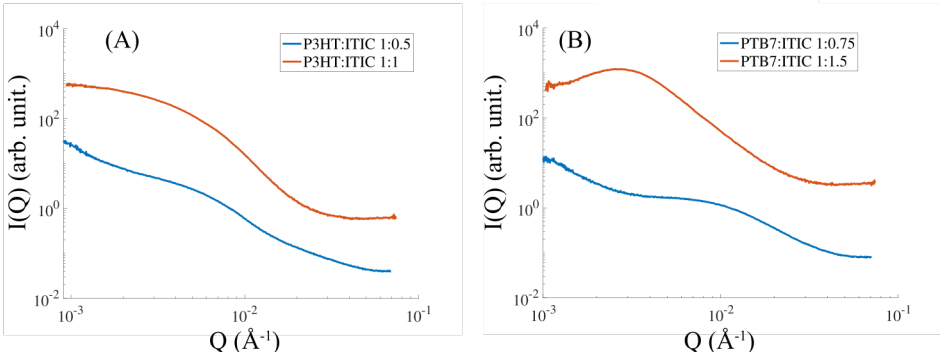

Figure 4.17 REXS at 285.2 eV (Carbon K-edge) stitched from close and far detector distances for (A) P3HT:ITIC blends, and (B) PTB7:ITIC blends.

The lower mole fraction sample for P3HT: ITIC shows a broad and low-intensity peak at a Q value of approximately 0.0060 $Å^{-1}$, whereas the higher mole fraction sample of ITIC in P3HT has a much stronger scattering signature at a Q value of approximately 0.0030 $Å^{-1}$. This is indicative of an expansion of phase separation of the small molecule upon increasing the mole fraction of ITIC in P3HT. The two aforementioned Q values can be represented in real space as 104.7 nm and 209.4 nm, respectively. Panel B of **Figure 4.17** shows a very similar evolution of phase separation

as seen in panel B of **Figure 4.15**. In this sample, the phase separation of ITIC in a PTB7 matrix becomes larger upon increasing the mole fraction of the small molecule. The approximate reciprocal space Q values for the lower and higher mole fraction of ITIC are 0.0086 $Å^{-1}$ and 0.0027 $Å^{-1}$, respectively. Since the Q value decreased upon increasing the mole fraction of ITIC in PTB7, this indicated that the length scale of phase separation of ITIC in the PTB7 matrix became larger. Specifically, these lengths of phase separation were determined for the lower and higher mole fractions of ITIC as 73.1 nm and 232.7 nm, respectively.

To leverage the elemental composition of ITIC in REXS experiments, energies associated with the nitrogen K-edge were used to induce resonant enhancement from only the small molecule.[30,31] Both of the films used to obtain carbon K-edge REXS data were also used to obtain the nitrogen K-edge REXS data, albeit at different locations of the sample as to not probe previously exposed material. This data is shown in **Figure 4.18**.

An energy of 399.4 eV which corresponds to the nitrogen K-edge absorption was used to enhance the scattering data obtained from the sample due to the chemical composition of ITIC.[30,31] The appearance of a very slight slope change in the scattering data in panel A makes it hard to accurately determine the size of the phase separation.

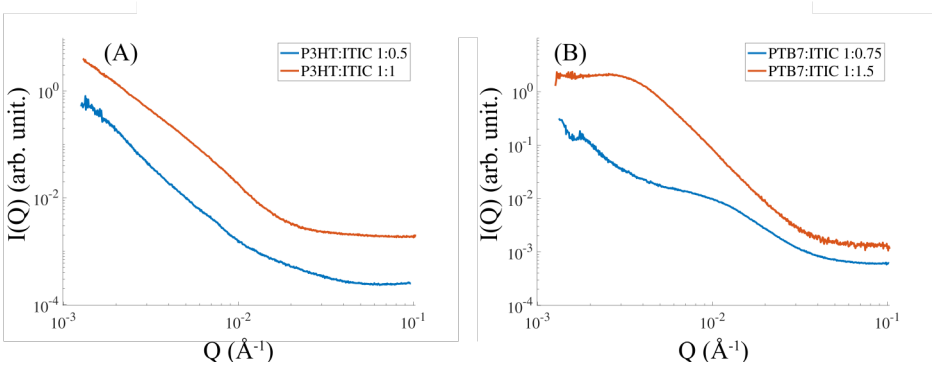

Figure 4.18 REXS at 399.4 eV (Nitrogen K-edge) stitched from close and far detector distances for (A) P3HT:ITIC blends, and (B) PTB7:ITIC blends.

However, panel B shows a noticeable change in feature shape and position. The positions in reciprocal space for the lower and higher mole fraction of ITIC blended with PTB7 appears at Q values of 0.0091 $Å^{-1}$ and 0.0028 $Å^{-1}$, respectively. The change in phase separation correlates well with the data obtained for the carbon K-edge resonant enhancement shown in panel B of **Figure 4.17**. Therefore, two things can be determined with high certainty. The first is that the energy of 285.2 eV which correlates with the carbon K- absorption edge was truly probing the length scale of the small molecule acceptor, due to having a significant contribution from ITIC at that energy. Secondly, the length scale of phase separation for ITIC in PTB7 can be confidently determined as increasing with increasing mole fraction of ITIC. The actual real-space values of phase separation determined are 69.5 nm and 224.3 nm, respectively. Compared with the values obtained for this sample in **Figure 4.17** of 73.1 nm and 232.7

nm, the values obtained from resonantly enhanced scattering from the nitrogen K-edge of ITIC are very similar.

4.4 Conclusion

When organic materials are incorporated into a solid-state device, their morphology matters for a slew of reasons. In organic OPVs, the π-stacking distance, crystallite orientation, and phase-separated length scales between donor and acceptor all have an impact on the device performance.[6,9,10] Organic materials should be able to withstand thermal abuse and retain their electronic, structural, and mechanical properties.[15,19,21–28,33,34] Since organics are often solution-processed, the resultant properties are also influenced by their deposition method. The morphology that the organic materials adopt in the solid-state needs to be robust and also facilitate the desired properties.

It is imperative that an understanding of how the morphology of organics change in the solid-state with exposure to different environmental conditions, such as chemical composition, blending ratio, deposition conditions, increased temperature, and mechanical strain. The ultimate technique to investigate morphological changes brought about from exposure to different conditions is X-ray scattering because the wavelength of radiation can successfully interact and report on the state of molecular packing.[9,10] X-ray scattering allows for investigations to occur over many length scales and is, therefore, a very important technique when needing to glean insight into the molecular orientations, packing, and arrangements.

GIXD experiments were utilized to determine packing distances at ambient and elevated temperatures.[20] This technique was also used to investigate the influence of four different deposition methods, and for use on determining the crystallite orientation distributions of nanofibrous organic materials.[35] The orientation and molecular packing of semi-conductive conjugated polymers are limiting aspects to device performance in organic electronics due to the need for close π-π interactions and isotropic or preferential anisotropic charge transport.[35]

Compared to GIXD, REXS experiments probe longer length scales and have other advantages such as being element-specific. This technique leverages the enhancement of scattered electrons in the vicinity of an element's absorption edge.[30,31] These scattering techniques are complementary to each other, and should always be considered in unison if resources allow. However, a drawback to X-ray scattering experiments is that this methodology averages the morphological features over the entirety of the probed sample volume. That is why microscopy is often used alongside X-ray scattering techniques to parse out real space inhomogeneities or real space morphological variations in a sample.[10]

4.5 References

(1) Rivnay, J.; Mannsfeld, S. C. B.; Miller, C. E.; Salleo, A.; Toney, M. F. Quantitative Determination of Organic Semiconductor Microstructure from the Molecular to Device Scale. *Chem Rev* 2012, *112* (10), 5488–5519. https://doi.org/10.1021/cr3001109.

(2) Huang, Y.-C.; Tsao, C.-S.; Huang, T.-Y.; Cha, H.-C.; Patra, D.; Su, C.-J.; Jeng, U.-S.; Ho, K.-C.; Wei, K.-H.; Chu, C.-W. Quantitative Characterization and Mechanism of Formation of Multilength-Scale Bulk Heterojunction Structures in Highly Efficient Solution-Processed Small-Molecule Organic Solar Cells. *J Phys Chem C* 2015, *119* (29), 16507–16517. https://doi.org/10.1021/acs.jpcc.5b05239.

(3) Alvarado, S. F.; Seidler, P. F.; Lidzey, D. G.; Bradley, D. D. C. Direct Determination of the Exciton Binding Energy of Conjugated Polymers Using a Scanning Tunneling Microscope. *Phys Rev Lett* 1998, *81* (5), 1082–1085. https://doi.org/10.1103/physrevlett.81.1082.

(4) Knupfer, M. Exciton Binding Energies in Organic Semiconductors. *Appl Phys* 2003, *77* (5), 623–626. https://doi.org/10.1007/s00339-003-2182-9.

(5) Takeda, N.; Asaoka, S.; Miller, J. R. Nature and Energies of Electrons and Holes in a Conjugated Polymer, Polyfluorene. *J Am Chem Soc* 2006, *128* (50), 16073–16082. https://doi.org/10.1021/ja062596h.

(6) Hedley, G. J.; Ruseckas, A.; Samuel, I. D. W. Light Harvesting for Organic Photovoltaics. *Chem Rev* 2017, *117* (2), 796–837. https://doi.org/10.1021/acs.chemrev.6b00215.

(7) Zhou, Y.; Li, M.; Shen, S.; Wang, J.; Zheng, R.; Lu, H.; Liu, Y.; Ma, Z.; Song, J.; Bo, Z. Hybrid Nonfused-Ring Electron Acceptors with Fullerene Pendant for High-Efficiency Organic Solar Cells. *Acs Appl Mater Inter* 2021, *13* (1), 1603–1611. https://doi.org/10.1021/acsami.0c19632.

(8) Nielsen, C. B.; Holliday, S.; Chen, H.-Y.; Cryer, S. J.; McCulloch, I. Non-Fullerene Electron Acceptors for Use in Organic Solar Cells. *Accounts Chem Res* 2015, *48* (11), 2803–2812. https://doi.org/10.1021/acs.accounts.5b00199.

(9) Chabinyc, M. L. X-ray Scattering from Films of Semiconducting Polymers. *Polym Rev* 2008, *48* (3), 463–492. https://doi.org/10.1080/15583720802231734.

(10) Birkholz, M. *Thin Film Analysis by X-Ray Scattering*; Wiley-VCH, 2006., pp 2, 175-203.

(11) Brabec, C. J.; Zerza, G.; Cerullo, G.; Silvestri, S. D.; Luzzati, S.; Hummelen, J. C.; Sariciftci, S. Tracing Photoinduced Electron Transfer Process in Conjugated Polymer/Fullerene Bulk Heterojunctions in Real Time. *Chem Phys Lett* 2001, *340* (3–4), 232–236. https://doi.org/10.1016/s0009-2614(01)00431-6.

(12) Shi, D.; Qin, X.; Li, Y.; He, Y.; Zhong, C.; Pan, J.; Dong, H.; Xu, W.; Li, T.; Hu, W.; Brédas, J.-L.; Bakr, O. M. Spiro-OMeTAD Single Crystals: Remarkably Enhanced Charge-Carrier Transport via Mesoscale Ordering. *Sci Adv* 2016, *2* (4), e1501491. https://doi.org/10.1126/sciadv.1501491.

(13) Zhao, Y.; Zhao, X.; Roders, M.; Qu, G.; Diao, Y.; Ayzner, A. L.; Mei, J. Complementary Semiconducting Polymer Blends for Efficient Charge Transport. *Chem Mater* 2015, *27* (20), 7164–7170. https://doi.org/10.1021/acs.chemmater.5b03349.

(14) Zhao, X.; Zhao, Y.; Ge, Q.; Butrouna, K.; Diao, Y.; Graham, K. R.; Mei, J. Complementary Semiconducting Polymer Blends: The Influence of Conjugation-Break Spacer Length in Matrix Polymers. *Macromolecules* 2016, *49* (7), 2601–2608. https://doi.org/10.1021/acs.macromol.6b00050.

(15) Zhao, Y.; Zhao, X.; Zang, Y.; Di, C.; Diao, Y.; Mei, J. Conjugation-Break Spacers in Semiconducting Polymers: Impact on Polymer Processability and Charge Transport Properties. *Macromolecules* 2015, *48* (7), 2048–2053. https://doi.org/10.1021/acs.macromol.5b00194.

(16) Lampert, M. A. Simplified Theory of Space-Charge-Limited Currents in an Insulator with Traps. *Physical Review* 2015, *103* (6), 1648–1656.

(17) Mark, P. Space-Charge-Limited Currents in Organic Crystals*. *Journal of Applied Physics* 1962, *33* (1), 205–215.

(18) Hertel, D.; Bässler, H. Photoconduction in Amorphous Organic Solids. *Chemphyschem* 2008, *9* (5), 666–688. https://doi.org/10.1002/cphc.200700575.

(19) Kintigh, J. T.; Hodgson, J. L.; Singh, A.; Pramanik, C.; Larson, A. M.; Zhou, L.; Briggs, J. B.; Noll, B. C.; Kheirkhahi, E.; Pohl, K.; McGruer, N. E.; Miller, G. P. A Robust, High-Temperature Organic Semiconductor. *J Phys Chem C* 2014, *118* (46), 26955–26963. https://doi.org/10.1021/jp505011x.

(20) Gumyusenge, A.; Tran, D. T.; Luo, X.; Pitch, G. M.; Zhao, Y.; Jenkins, K. A.; Dunn, T. J.; Ayzner, A. L.; Savoie, B. M.; Mei, J. Semiconducting Polymer Blends That Exhibit Stable Charge Transport at High Temperatures. *Science* 2018, *362* (6419), 1131–1134. https://doi.org/10.1126/science.aau0759.

(21) Morita, T.; Singh, V.; Nagamatsu, S.; Oku, S.; Takashima, W.; Kaneto, K. Enhancement of Transport Characteristics in Poly(3-Hexylthiophene) Films Deposited with Floating Film Transfer Method. *Appl Phys Express* 2009, *2* (11), 111502. https://doi.org/10.1143/apex.2.111502.

(22) Nawaz, A.; Tavares, A. C. B.; Do, T. T.; Patil, B. B.; Sonar, P.; Hümmelgen, I. A. Experimental and Modeling Study of Low-Voltage Field-Effect Transistors Fabricated with Molecularly Aligned Copolymer Floating Films. *Flexible Print Electron* 2018, *3* (1), 015006. https://doi.org/10.1088/2058-8585/aaa97b.

(23) Giri, G.; DeLongchamp, D. M.; Reinspach, J.; Fischer, D. A.; Richter, L. J.; Xu, J.; Benight, S.; Ayzner, A.; He, M.; Fang, L.; Xue, G.; Toney, M. F.; Bao, Z. Effect of Solution Shearing Method on Packing and Disorder of Organic Semiconductor Polymers. *Chem Mater* 2015, *27* (7), 2350–2359. https://doi.org/10.1021/cm503780u.

(24) Shaw, L.; Hayoz, P.; Diao, Y.; Reinspach, J. A.; To, J. W. F.; Toney, M. F.; Weitz, R. T.; Bao, Z. Direct Uniaxial Alignment of a Donor-Acceptor Semiconducting Polymer Using Single-Step Solution Shearing. *Acs Appl Mater Inter* 2016, *8* (14), 9285–9296. https://doi.org/10.1021/acsami.6b01607.

(25) Giri, G.; Verploegen, E.; Mannsfeld, S. C. B.; Atahan-Evrenk, S.; Kim, D. H.; Lee, S. Y.; Becerril, H. A.; Aspuru-Guzik, A.; Toney, M. F.; Bao, Z. Tuning Charge Transport in Solution-Sheared Organic Semiconductors Using Lattice Strain. *Nature* 2011, *480* (7378), 504–508. https://doi.org/10.1038/nature10683.

(26) Noebels, M.; Cross, R. E.; Evans, D. A.; Finlayson, C. E. Characterization of Spray-Coating Methods for Conjugated Polymer Blend Thin Films. *J Mater Sci* 2014, *49* (12), 4279–4287. https://doi.org/10.1007/s10853-014-8123-5.

(27) Bielecka, U.; Lutsyk, P.; Janus, K.; Sworakowski, J.; Bartkowiak, W. Effect of Solution Aging on Morphology and Electrical Characteristics of Regioregular P3HT FETs Fabricated by Spin Coating and Spray Coating. *Org Electron* 2011, *12* (11), 1768–1776. https://doi.org/10.1016/j.orgel.2011.06.027.

(28) Scarratt, N. W.; Griffin, J.; Wang, T.; Zhang, Y.; Yi, H.; Iraqi, A.; Lidzey, D. G. Polymer-Based Solar Cells Having an Active Area of 1.6 Cm2 Fabricated via Spray Coating. *Apl Mater* 2015, *3* (12), 126108. https://doi.org/10.1063/1.4937553.

(29) Balar, N.; Xiong, Y.; Ye, L.; Li, S.; Nevola, D.; Dougherty, D. B.; Hou, J.; Ade, H.; O'Connor, B. T. Role of Polymer Segregation on the Mechanical Behavior of All-Polymer Solar Cell Active Layers. *Acs Appl Mater Inter* 2017, *9* (50), 43886–43892. https://doi.org/10.1021/acsami.7b13719.

(30) Su, G. M.; Cordova, I. A.; Brady, M. A.; Prendergast, D.; Wang, C. Combining Theory and Experiment for X-Ray Absorption Spectroscopy and Resonant X-Ray Scattering Characterization of Polymers. *Polymer* 2016, *99*, 782–796. https://doi.org/10.1016/j.polymer.2016.06.068.

(31) Liu, F.; Brady, M. A.; Wang, C. Resonant Soft X-Ray Scattering for Polymer Materials. *Eur Polym J* 2016, *81*, 555–568. https://doi.org/10.1016/j.eurpolymj.2016.04.014.

(32) Belloni, L. Historical Remarks on the «classical» Electron Radius. *Lett Al Nuovo Cimento 1971-1985* 1981, *31* (4), 131–134. https://doi.org/10.1007/bf02822412.

(33) Patel, S. N.; Chabinyc, M. L. Anisotropies and the Thermoelectric Properties of Semiconducting Polymers. *J Appl Polym Sci* 2016, *134* (3). https://doi.org/10.1002/app.44403.

(34) Peng, J.; Chen, Y.; Wu, X.; Zhang, Q.; Kan, B.; Chen, X.; Chen, Y.; Huang, J.; Liang, Z. Correlating Molecular Structures with Transport Dynamics in High-Efficiency Small-Molecule Organic Photovoltaics. *Acs Appl Mater Inter* 2015, *7* (24), 13137–13141. https://doi.org/10.1021/acsami.5b03073.

(35) Gumyusenge, A.; Luo, X.; Zhang, H.; Pitch, G. M.; Ayzner, A. L.; Mei, J. Isoindigo-Based Binary Polymer Blends for Solution-Processing of Semiconducting Nanofiber Networks. *Acs Appl Polym Mater* 2019, *1* (7), 1778–1786. https://doi.org/10.1021/acsapm.9b00321.

Appendix

Supporting Information for

Aqueous Light Harvesting Antennae based on Brush-Like Conjugated Polyelectrolyte Complexes: Self-Assembly and Electronic Energy Transfer

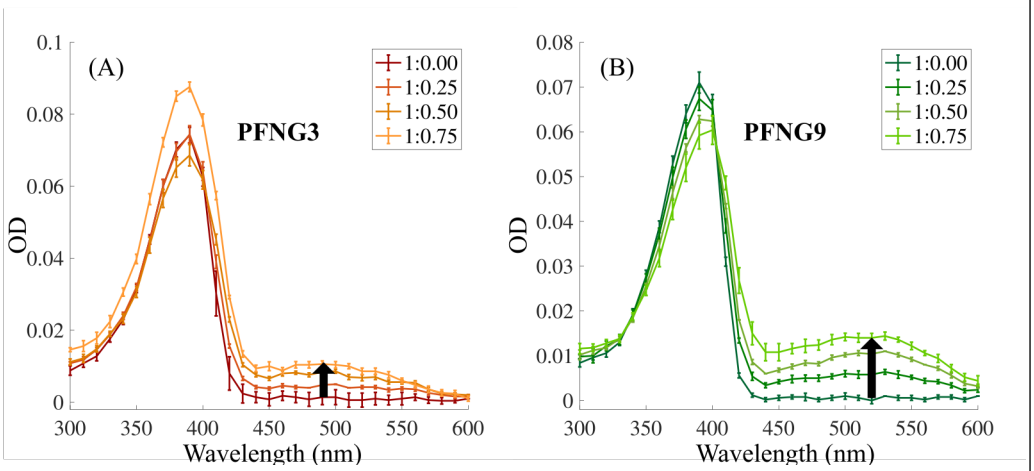

Figure A1.1 (A) Optical densities of PFNG3, and PFNG3 CPECs formed with PTAK at molar charge percentages of 25%, 50%, 75%. (B) Optical densities of PFNG9, and PFNG9 CPECs formed with PTAK at molar charge percentages of 25%, 50%, 75%.

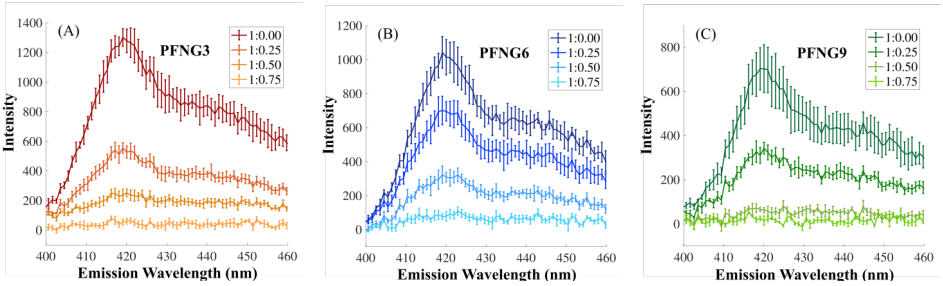

Figure A1.2 PL intensity quenching data for PFNGX excited at 375 nm in the presence of PTAK (A) PFNG3, (B) PFNG6, (C) PFNG9.

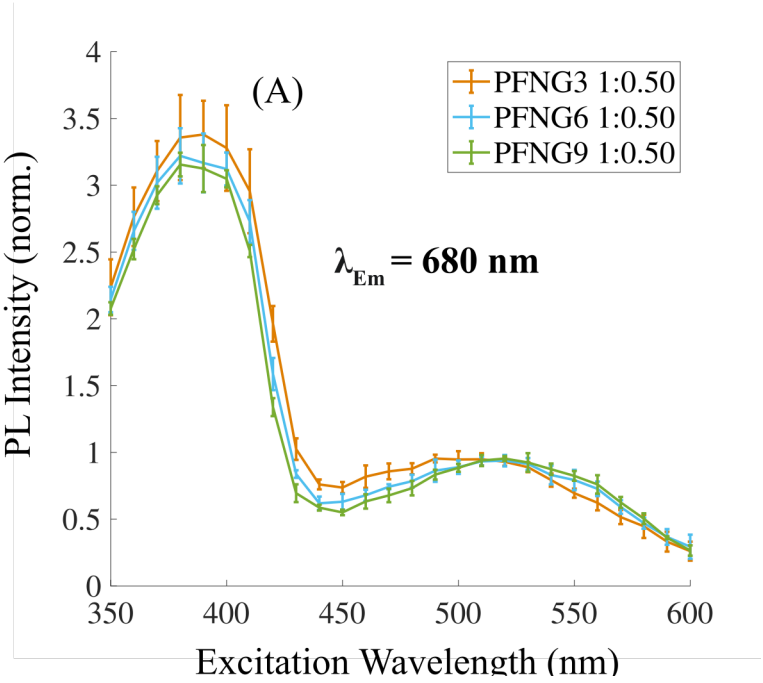

Figure A1.3 (A) Normalized photoluminescence excitation spectra of PFNGX CPECs formed with PTAK at molar charge percentages of 50%.